

PRECISE POINT POSITIONING WITH GPS

A NEW APPROACH FOR POSITIONING, ATMOSPHERIC STUDIES, AND SIGNAL ANALYSIS

RODRIGO FIGUEIREDO LEANDRO

April 2009



**TECHNICAL REPORT
NO. 267**

**PRECISE POINT POSITIONING WITH GPS
A NEW APPROACH FOR POSITIONING,
ATMOSPHERIC STUDIES, AND SIGNAL
ANALYSIS**

Rodrigo Figueiredo Leandro

Department of Geodesy and Geomatics Engineering
University of New Brunswick
P.O. Box 4400
Fredericton, N.B.
Canada
E3B 5A3

April 2009

© Rodrigo F. Leandro 2009

PREFACE

This technical report is a reproduction of a dissertation submitted in partial fulfillment of the requirements for the degree of Doctor of Philosophy in the Department of Geodesy and Geomatics Engineering, April 2009. The research was supervised by Dr. Marcelo Santos, and funding was provided by the Canadian International Development Agency and the Natural Sciences and Engineering Research Council of Canada.

As with any copyrighted material, permission to reprint or quote extensively from this report must be received from the author. The citation to this work should appear as follows:

Leandro, R. F. (2009). *Precise Point Positioning with GPS: A New Approach for Positioning, Atmospheric Studies, and Signal Analysis*. Ph.D. dissertation, Department of Geodesy and Geomatics Engineering, Technical Report No. 267, University of New Brunswick, Fredericton, New Brunswick, Canada, 232 pp.

DEDICATION

To Ivi, Camila, and Isabel.

ABSTRACT

Precise Point Positioning (PPP) is one of the existing techniques to determine point coordinates using a GPS (Global Positioning System) receiver. In this technique observations collected by a single receiver are used in order to determine the three components of the coordinates, as well as other parameters, such as the receiver clock error and total neutral atmosphere delay.

The PPP technique is the subject of this thesis. The idea is that PPP could be used not only for positioning, but for a number of different tasks, as GPS data analysis. The observation model used in this technique has to take into consideration a number of effects present on GPS signals, and observations are un-differenced (there are no differences between receivers or between satellites). This makes PPP a powerful data analysis tool which is sensible to a variety of parameters. When the observation model is designed for positioning, most of these parameters (e.g., satellite clocks) are used as known quantities, but in this research the observation model was modified and enhanced to develop a PPP package that can be used as a tool for determining other parameters rather than position, receiver clock error and neutral atmosphere delay. These estimated parameters include ionospheric delay, code biases, satellite clock errors, and code multipath plus noise.

Existing neutral atmosphere delay models have also been studied in this thesis, and an enhanced model has been developed and has had its performance assessed. The development of the model is based on measured meteorological parameters, and the

rationale of the model is established in order to make its use as practical as possible for users of positioning techniques, such as PPP.

ACKNOWLEDGEMENTS

During five years of work I have received different kinds of support from several people and institutions that helped me to achieve the completion of the doctoral degree.

Therefore I would like to acknowledge:

My wife, Ivi, and daughters Camila and Isabel, for their unconditional love and care, always being at my side offering all kind of support I would need for accomplishing my studies. This thesis has been written with you, and for you, my beloved family.

My parents, José Paulo and Maria Cristina, for the education, love, and support they have given to me throughout my entire life, especially in difficult times.

My supervisor Dr. Marcelo Santos, for giving the opportunity of coming to University of New Brunswick for the Ph.D. program. Also, for all his efforts in helping me to perform this work in the best way I could, with his technical advices, financial support, and for providing a good work environment. It has been a pleasure being Dr. Santos' student over the last years. He has proven to be much more than a supervisor, as he became a real friend of me and my family. I would like to extend my thanks to Dr. Santos to his family, Ms. Denise Ferreira and Thales, who made our stay in Fredericton much more pleasant than it would be without them.

Dr. Richard B. Langley, for his enormous contributions for the development of the present work. Dr. Langley has been extremely active in giving his helpful advices whenever they were needed, and has been always available for discussions that were certainly critical for the quality of this research.

Felipe G. Nievinski, for all helpful discussions carried out throughout the years we worked together. I also would like to thank Felipe and his wife, Giovana, for their great support during times when I was without my family in Fredericton.

Sylvia Whitaker, for her great support in getting around with all paperwork issues as a graduate student at UNB.

The Canadian International Development Agency (CIDA), for financial support provided for this research.

Natural Sciences and Engineering Research Council of Canada, for financial support provided for this research.

The International GNSS Service (IGS), for providing GNSS observation data from sites all over the world that was used in several parts of this research.

Natural Resources Canada (NRCan), for providing a license of their precise point positioning software.

Pierre Héroux and François Lahaye, for several helpful discussions and advices based on their experience that helped me to better understand and develop a precise point positioning software.

Seth Guttman and his colleagues at National Oceanic and Atmospheric Administration (NOAA), for making the Integrated Surface Hourly (ISH) database available. This database was crucial in the development of the UNBw.na model.

Paul Collins, for providing the radiosonde quality-control software that was used for pre-processing the radiosonde data before it could be used for ray-tracing. Paul also provided great feedback based on his experience with the development of UNB neutral atmosphere models.

James Davis, Thomas Herring, and Arthur Niell, for the ray-tracing software that was used along with the radiosonde data to compute the neutral atmosphere delays used as benchmark in the validation of the new neutral atmosphere model.

Carey Noll from the Crustal Dynamics Data Information System, for her great efforts in managing the IGS L2C Test network, as well as for her help in assuring the completeness of UNB3 stored data.

Alexandre Garcia, for his great work in assessing GAPS online that helped me to make it a better free online positioning service.

Dr. Herbert Landau, for his great effort in supporting and making sure I would not lose the focus on finishing my Ph.D..

Margit Dietrich, for her great efforts in making my family's adaptation to Germany as easy as possible, what facilitated the continued work on my Ph.D. thesis.

I would like to thank a number of people who have contributed to my academic formation at University of São Paulo, prior starting at UNB: Dr. Paulo Segantine, Dr. José Setti, Dr. Ricardo Schaal, Dr. Carlos Silva, Dr. Tule Maia, Dr. Genival Corrêa, and Dr. Maurício Veronez. I also thank all of them for their continued support during my years of work at UNB.

There are many other people I would like to thank for all the support I have received during the last years. Some of them are Tirso Barros, Antonieta Albaneze, Carlos Guimarães, Pablo Vilela, Humberto Gonçalves, Júlio Farret, Daniel Cid, Aluizio Oliveira, João Chaves, Leonel Manteigas, Ricardo Almeida, and their respective families.

Table of Contents

DEDICATION	ii
ABSTRACT	iii
ACKNOWLEDGEMENTS	v
Table of Contents	ix
List of Tables.....	xii
List of Figures	xiv
List of Symbols, Nomenclature or Abbreviations.....	xx
1. Introduction	1
1.1. Motivation	2
1.2. Objectives and contributions	3
1.3. Outline of the thesis	8
2. Precise Point Positioning and GPS Analysis and Positioning Software (GAPS)	10
2.1. A bit of history, and GAPS's role in PPP research and development	10
2.2. The positioning observation model.....	14
2.3. Observations adjustment	23
2.4. Corrections	35
2.4.1. Satellite antenna phase center offset and variation	35
2.4.2. Receiver antenna phase center offset and variation	41
2.4.3. Solid earth tide	45
2.4.4. Ocean tide loading.....	46

2.4.5. Differential code biases	47
2.4.6. Phase wind-up effect	48
3. Ionospheric delay estimation filter	49
3.1. Introduction	49
3.2. Ionospheric delay estimation filter	50
3.3. Results analysis.....	65
3.4. Chapter remarks	89
4. Estimation of code biases by means of PPP.....	91
4.1. Introduction	91
4.2. PPP-based P1-C1 code bias estimation.....	94
4.3. PPP-based P2-C2 code bias estimation.....	114
4.5. Chapter remarks	121
5. Code multipath and noise estimation with PPP.....	123
5.1. Iono-free code multipath plus noise estimates	123
5.2. L1 and L2 code multipath plus noise estimates.....	130
5.3. Comparison with TEQC.....	133
5.4. Analysis of L2C code quality	139
5.5. Chapter remarks	145
6. Single-receiver satellite pseudo-clock estimation	147
6.1. Derivation of the satellite pseudo-clocks	148
6.2. An example of generation and use of satellite pseudo-clocks.....	152
6.3. Chapter remarks	164

7. Neutral Atmosphere prediction models for GNSS positioning.....	166
7.1. Introduction	167
7.2. UNB wide area models	178
7.3. UNB wide area model for North America – UNBw.na.....	191
7.4. UNBw.na validation with ray-traced delays	201
7.5. Chapter remarks.....	210
8. Conclusions and recommendations	214
9. Bibliography.....	220
Appendix A: UNB3m_pack, a Neutral Atmosphere Delay Package for Radiometric	
Space Techniques	225
A.1. UNB3m_pack	225
A.2. Using UNB3m subroutines.....	227
A.2.1. UNB3m – Delays subroutine	227
A.2.2. UNB3mr – Delay rates subroutine	229
A.2.2. UNB3mm – Meteorological values subroutine	230
A.3. UNB3m_pack retrieval.....	232

Vita

List of Tables

Table 2.1. GPS satellite constellation history, as of July 2007.	38
Table 3.1. Receiver types of the stations used in this analysis (according to their respective site logs – accessed on September 2007).	83
Table 3.2. Statistics of GAPS and IGS maps comparison (in the sense GAPS-IGS)	88
Table 4.1. L2C Test Network stations (as of January 2007)	108
Table 4.3. P2-C2 satellite biases.	119
Table 4.4. P2-C2 satellite biases.	120
Table 5.1. Multipath plus noise values computed for each satellite observed by UNBJ station.	137
Table 6.1. Kinematic PPP run RMS values (cm).	164
Table 7.1. GAPS-PPP results from processing UNBJ data with variations on how the neutral atmosphere is handled.	170
Table 7.2. Look-up table of UNB3m model.	176
Table 7.3. General statistics for temperature estimation errors (all values in kelvins). ..	197
Table 7.4. General statistics for pressure estimation errors (all values in mbar).	199
Table 7.5. General statistics for WVP estimation errors (all values in mbar).	201
Table 7.6. General statistics of total zenith delay prediction performance (all values in mm).	204
Table 7.7. Statistics (bias, standard deviation and rms) for analysis regions (all values in cm).	205
Table 7.8. Average absolute biases (aab) and their standard deviations (aab-sd) - all values in cm.	205
Table 7.9. Numerical results for sample stations (represented by the first four characters of their names) – all values in cm.	210
Table A.1. UNB3m input and output.	228
Table A.2. UNB3mr input and output.	229

Table A.3. UNB3mm input and output.231

List of Figures

Figure 2.1. GPS satellite antenna offsets as of July of 2007 (Reference: International GNSS Service, file igs05_1421.atx). In this file there was no antenna information for SVN's 1, 2, 3, 4, 5, 6, 7, 8, 12, 42, 48, 49, 50, 55, and 57, for different reasons.....	39
Figure 2.2. GPS satellite antenna phase center variation, as of July of 2007 (Reference: International GNSS Service, file igs05_1421.atx). Recently launched SVN's 55 and 57 have the same variation as 52, 53 and 58.	41
Figure 2.3. Diagram of UNBJ station antenna (RegAnt choke-ring antenna). Similar diagram can be obtained from UNBJ station log file, available at http://igs.cb.jpl.nasa.gov/igs/cb/station/log/unbj_20060906.log .The antenna offsets used here were obtained from ANTEX file igs05_1421.atx.....	43
Figure 2.4. Antenna L1 phase center variation for station UNBJ's antenna, as of March 2008. Values obtained from file igs05_1421.atx.	44
Figure 2.5. Antenna L2 phase center variation for station UNBJ's antenna, as of March 2008. Values obtained from file igs05_1421.atx.	44
Figure 2.6. Antenna L1 and L2 phase center variation for station UNBJ's antenna, as of March 2008. Values obtained from file igs05_1421.atx.	45
Figure 2.7. Variation of UNBJ station site displacement due to solid earth tide over one day (5 March 2008).	46
Figure 3.1. Elements of the spherical ionospheric shell model.....	60
Figure 3.2. Relationship between positioning and ionospheric delay filters in GAPS.	65
Figure 3.3. Ionospheric delays computed with GAPS for station UNBJ, data observed at January 1 st 2007.....	66
Figure 3.4. Stations used in the ionospheric delay filter analysis.	68
Figure 3.5. Kp index values for days of year 312 to 316 of 2004.....	69
Figure 3.6. Kp index values for days of year 006 to 010 of 2007.....	69
Figure 3.7. Ionospheric delays and residuals for station UNBJ, 2007 DOY 6 to 10.	72
Figure 3.8. Ionospheric delays and residuals for station UNB1, 2004 DOY 312 to 316.	73
Figure 3.9. Ionospheric delays and residuals for station FRDN, 2007 DOY 6 to 10.....	74

Figure 3.10. Ionospheric delays and residuals for station FRDN, 2004 DOY 312 to 316.	74
Figure 3.11. Ionospheric delays and residuals for station BRAN, 2007 DOY 6 to 10.	75
Figure 3.12. Ionospheric delays and residuals for station BRAN, 2004 DOY 312 to 316.	75
Figure 3.13. Ionospheric delays and residuals for station LEEP, 2007 DOY 6 to 10.....	76
Figure 3.14. Ionospheric delays and residuals for station LEEP, 2004 DOY 312 to 316.	76
Figure 3.15. Ionospheric delays and residuals for station MANA, 2007 DOY 6 to 10. ...	77
Figure 3.16. Ionospheric delays and residuals for station MANA, 2004 DOY 312 to 316.	78
Figure 3.17. Ionospheric delays and residuals for station RIOG, 2007 DOY 6 to 10.....	79
Figure 3.18. Ionospheric delays and residuals for station RIOG, 2004 DOY 312 to 316.	79
Figure 3.19. Comparison of results for stations BRAN and LEEP, 2007 DOY 6 to 10. ..	80
Figure 3.20. Comparison of results for stations BRAN and LEEP, 2004 DOY 312 to 316.	81
Figure 3.21. Comparison of results for stations UNBJ and FRDN, 2007 DOY 6 to 10. ..	82
Figure 3.22. Comparison of results for stations UNB1 and FRED, 2004 DOY 312 to 316.	82
Figure 3.23. Comparison of results provided by GAPS (blue dots) and IGS (red line) for station BRAN.	85
Figure 3.24. Comparison of results provided by GAPS (blue dots) and IGS (red line) for station LEEP.....	86
Figure 3.25. Comparison of results provided by GAPS (blue dots) and IGS (red line) for station UNBJ/UNB1.	86
Figure 3.26. Comparison of results provided by GAPS (blue dots) and IGS (red line) for station FRDN.	86
Figure 3.27. Comparison of results provided by GAPS (blue dots) and IGS (red line) for station MANA.	87

Figure 3.28. Comparison of results provided by GAPS (blue dots) and IGS (red line) for station RIOG, quiet period.....	87
Figure 4.1. P1-C1 bias estimation, according to Equation 4.10, for station UNB3, PRN03, on DOY 280 of 2007.	98
Figure 4.2. Epoch per epoch estimates for PRN03 P1-C1 bias over 10 days, using UNB3 data (elevation cutoff 10 degrees).	100
Figure 4.3. Daily PRN03 P1-C1 estimations using UNB3 data.	101
Figure 4.4. Deviation of bias daily estimates from the 10-day estimate.	102
Figure 4.5. Daily P1-C1 bias results for all satellites, using UNB3 data.	102
Figure 4.6. Daily mean P1-C1 biases.	103
Figure 4.7. Satellite P1-C1 code biases determined using the 10-day UNB3 dataset.....	104
Figure 4.8. Comparison between P1-C1 satellite biases provided by CODE and computed with GAPS (using data from UNB3).....	105
Figure 4.9. Difference between P1-C1 satellite biases provided by CODE and computed with GAPS (using data from UNB3).....	106
Figure 4.10. Estimated uncertainties for the two solutions and their difference.....	107
Figure 4.11. P1-C1 bias determination results for each station/day.....	109
Figure 4.12. Estimated uncertainties for P1-C1 bias determined for each station/day. ...	109
Figure 4.13. GAPS-determined P1-C1 biases (white bars) and respective uncertainties (red error bars) for non-Block IIR-M satellites.....	111
Figure 4.14. Comparison between P1-C1 determined with GAPS and CODE's values.	112
Figure 4.15. Differences between P1-C1 determined with GAPS and CODE's values.	112
Figure 4.16. Estimates uncertainties for P1-C1 bias solutions and their differences.	113
Figure 4.19. Results of the P2-C2 satellite bias determination for several days and stations.	119
Figure 5.1. Iono-free code multipath plus noise estimates for PRN 10, station UNBJ. ...	128
Figure 5.2. Iono-free code M+N for station UNBJ, on DOY 134 of 2007.....	129

Figure 5.3. Iono-free code M+N with respect to elevation angle for station UNBJ, on DOY 134 of 2007.	129
Figure 5.4. L1C and L2P(Y) code M+N for PRN10, station UNBJ, on DOY 134 of 2007.	133
Figure 5.5. L1C (MP1) and L2P(Y) (MP2) code M+N estimates using TEQC, for PRN10, station UNBJ, on DOY 134 of 2007.	134
Figure 5.6. L1C (MP1) and L2P(Y) (MP2) code M+N estimates using TEQC, for PRN10, station UNBJ, on DOY 134 of 2007.	135
Figure 5.7. L1C (MP1) and L2P(Y) (MP2) code M+N estimates using TEQC, for PRN10, station UNBJ, on DOY 134 of 2007.	136
Figure 5.8. L1C (MP1) and L2P(Y) (MP2) code M+N estimate differences in the sense GAPS-TEQC for station UNBJ, on DOY 134 of 2007.	138
Figure 5.9. Code residuals for C2- and P2-based iono-free code observations.	141
Figure 5.10. Receiver-satellite C2-P2 bias combination derivation.	142
Figure 5.11. C2- and P2-based iono-free pseudorange residuals.	143
Figure 5.12. Rms of Figure 5.11 residuals for different elevation angle bins.	144
Figure 6.1. Stations UNBJ and SHE2.	152
Figure 6.2. Pseudo-clock file created from SHE2 data.	153
Figure 6.3. Comparison between GAPS satellite pseudo-clock solution and IGS clock solution.	154
Figure 6.4. Comparison of between-satellite clock differences of GAPS satellite pseudo-clock solution and IGS clock solution.	156
Figure 6.5. Comparison of between-satellite clock differences of GAPS satellite pseudo-clock solution for IGS clock solution (arithmetic mean of each time series removed)...	156
Figure 6.6. Comparison between GAPS satellite pseudo-clock solution and IGS clock solution.	157
Figure 6.7. Horizontal error convergence from a PPP static run using IGS clocks, and SHE2 pseudo-clocks.	159
Figure 6.8. First two hours of horizontal error convergence from a PPP static run using IGS clocks and SHE2 pseudo-clocks.	160

Figure 6.9. Height error convergence from a PPP static run using IGS clocks and SHE2 pseudo-clocks.....	160
Figure 6.10. First two hours of height error convergence from a PPP static run using IGS clocks and SHE2 pseudo-clocks.....	161
Figure 6.11. Horizontal error convergence from a PPP kinematic run using IGS clocks and SHE2 pseudo-clocks.	162
Figure 6.12. First two hours of horizontal error convergence from a PPP kinematic run using IGS clocks, and SHE2 pseudo-clocks.	163
Figure 6.13. Height error convergence of a PPP kinematic run using IGS clocks, and SHE2 pseudo-clocks.....	163
Figure 7.1. Neutral atmosphere delay as given by UNB3m prediction model and Niell mapping function.....	169
Figure 7.2. GAPS-PPP results from processing UNBJ data with variations on how the neutral atmosphere is handled.	171
Figure 7.3. UNB3m surface meteorological parameter predictions compared to measured surface parameter values for 50° N, 66° W.....	177
Figure 7.4. Distribution of ISH Database meteorological stations.....	179
Figure 7.5. Grid interpolation procedure	180
Figure 7.6. UNBw.na grid (red lines).....	191
Figure 7.7. Distribution of meteorological stations over the UNBw.na grid.....	192
Figure 7.8. Distribution of the control stations (black dots) and the calibration stations (green crosses).....	193
Figure 7.9. Height (in meters – represented by color) of the meteorological stations. ...	194
Figure 7.10. Average MSL temperature given by UNB3m and UNBw.na, in kelvins. ...	195
Figure 7.11. MSL temperature difference between UNBw.na and UNB3m, in kelvins. ...	195
Figure 7.12. Biases encountered when estimating temperature for control stations, in kelvins.....	196
Figure 7.13. Average pressure at grid nodes, given by UNBw.ca and UNB3m, in mbar.	197

Figure 7.14. Average MSL pressure difference between UNBw.na and UNB3m, in mbar.	198
Figure 7.15. Mean biases encountered when estimating pressure for control stations, in mbar.	198
Figure 7.16. Average MSL relative humidity for grid nodes, given by UNBw.na and UNB3m, in %.....	200
Figure 7.17. Difference between average MSL relative humidity provided by UNBw.na and UNB3m, in %.....	200
Figure 7.18. Mean biases encountered when estimating water vapour pressure for control stations, in mbar.	201
Figure 7.19. Distribution of radiosonde stations in North America and some nearby territories.	202
Figure 7.20. Total zenith delay estimation biases for each station, in meters.	203
Figure 7.21. Total zenith delay estimation rms values for each station, in meters.	203
Figure 7.22. Division of the four analysis regions.	204
Figure 7.23. Station biases with respect to station heights.	206
Figure 7.24. Total zenith delay estimation for station Belize.	207
Figure 7.25. Total zenith delay estimation for station Pittsburgh.	208
Figure 7.26. Total zenith delay estimation for station Salt Lake City.....	208
Figure 7.27. Total zenith delay estimation for station Bethel.....	209
Figure 7.28. Total zenith delay estimation for station Eureka.....	209

List of Symbols, Nomenclature or Abbreviations

ANTEX	Antenna Exchange (format)
APC	Antenna Phase Center
CDDIS	Crustal Dynamics Data Information System
CDGPS	Canada Differential GPS
CODE	Center for Orbit Determination in Europe
DCB	Differential Code Bias
df	Number of degrees of freedom of the adjustment
DOY	Day of Year
e	Geometric satellite elevation angle with respect to the observer
GAPS	GPS Analysis and Positioning Software
GGE	Department of Geodesy and Geomatics Engineering
GLONASS	Global Navigation Satellite System
GNSS	Global Navigation Satellite Systems
GPS	Global Positioning System
GSD	Geodetic Survey Division
H	Orthometric height
IERS	International Earth Rotation Service
IGS	International GNSS Service
IONEX	Ionosphere Map Exchange (format)
ISH	Integrated Surface Hourly (database)
Kp	Planetary K (index)

LEO	Low Earth Orbiter
MF	Mapping Function
MSL	Mean Sea Level
M+N	Multipath plus Noise
NAD	Neutral Atmosphere Delay
NASA	National Aeronautics and Space Administration
NOAA	National Oceanic and Atmospheric Administration NOAA
NRCan	Natural Resources Canada
PCV	Phase Center Variation
PPP	Precise Point Positioning
PRN	Pseudorandom Noise
R	Gas constant for dry air
r	Mean radius of the earth
RH	Relativity Humidity
RINEX	Receiver Independent Exchange (format)
RMS	Root Mean Square
sh	Ionospheric shell height
SVN	Spacecraft Number
TEC	Total integrated electron content
TECU	Total integrated electron content unit
TEQC	Toolkit for GPS/GLONASS/Galileo/SBAS Data
UNBw.na	Wide Area Neutral Atmosphere Model for North America
WVP	Water Vapour Pressure

\underline{A}	Design matrix
α	Coefficient for L1 in the iono-free combination equation
Avg and Amp	Average and amplitude
\hat{b}	Bias estimate
$b_{\text{if-P1}}$	Satellite instrumental bias between the P1 and P2 iono-free combination and P1 code
$b_{\text{P1-C1}}$	Satellite instrumental bias between P1 code and C1 code
$b_{\text{P2-C2}}^r$	Receiver P2-C2 bias
$b_{\text{P2-C2}}^{r-s}$	Receiver-satellite differential P2-C2 bias
$b_{\text{P1-C1}}^s$	Satellite P1-C1 bias
$b_{\text{P2-C2}}^s$	Satellite P2-C2 bias
β	Coefficient for L2 in the iono-free combination equation
β	Temperature lapse rate (Chapter 7 only)
β_{avg} and β_{amp}	Temperature lapse rate yearly average and amplitude
c	Speed of light
C_{if} and c_{if}	Pseudorange and carrier-phase corrections
$\underline{\text{CMP}}$	Three-dimensional vector representing the satellite center of mass position
\underline{C}_x	Parameters covariance matrix
dT and dt	Receiver and satellite clock errors
dT'	Modified receiver clock parameter

d_h^z and d_{nh}^z	Hydrostatic and non-hydrostatic neutral atmosphere zenith delays
$\underline{\delta}$	Parameters update vector
∇_ϕ and ∇_λ	Latitudinal and longitudinal vertical ionospheric delay gradients
$\delta N'_{if}$	Residual iono-free ambiguity
δR	Line-of-sight residual orbit error
δT	Line-of-sight residual neutral atmosphere error
e_0	Mean sea level water vapour pressure
E_1 and E_2	Un-modeled errors of pseudorange measurements on L1 and L2
e_1 and e_2	Un-modeled errors of carrier-phase measurements on L1 and L2
es_0	Mean sea level saturation water vapour pressure
$es(T_d)$	Saturation water vapour pressure for dew point temperature
$e_s(T_d)'$	Evaluated saturation water vapour pressure for dew point temperature
f_i	Frequency of the signal, where i represents the carrier frequency (L1 or L2)
$f_{w,0}$	Mean sea level enhancement factor
g	Standard acceleration of gravity
g_m	Acceleration of gravity at the atmospheric column centroid
γ	Factor to convert the ionospheric delay from L1 to L2 frequency
$HD_{r,i}$ and $HD_{s,i}$	Receiver and satellite pseudorange hardware delays, where i represents the carrier frequency (L1 or L2)

$hd_{r,i}$ and $hd_{s,i}$	Receiver and satellite carrier-phase hardware delays, where i represents the carrier frequency (L1 or L2)
I	L1 frequency ionosphere delay
I_i	Ionospheric delay, where i represents the carrier frequency (L1 or L2)
I_v	Vertical ionospheric delay
$I_{v,p}$ and $I_{v,0}$	Ionospheric vertical delays at the piercing point and the station location
k_1, k'_2 and k_3	Refractivity constants
λ	Water vapour pressure height factor (Chapter 7 only)
λ_1 and λ_2	Carrier-phase wavelengths on L1 and L2 frequencies
$\lambda_{g,p}$ and $\lambda_{g,0}$	Geographic longitude of the piercing point and the station
λ_p and ϕ_p	Longitude and latitude of the point of interest
M_1 and M_2	Pseudorange multipath on L1 and L2 frequencies
m_1 and m_2	Carrier-phase multipath on L1 and L2 frequencies
m_h and m_{nh}	Hydrostatic and non-hydrostatic mapping functions
mf_{nh}	Non-hydrostatic mapping function
N_1 and N_2	Carrier-phase integer ambiguities on L1 and L2 frequencies
N_{gf}	Carrier-phase geometry-free ambiguity
N'_{gf}	Modified carrier-phase geometry-free ambiguity
$N'_{gf,pl}$	Geometry-free ambiguity parameter of the phase-leveling

	technique
N_{if}	Ionosphere-free ambiguity
N'_{if}	Modified ionosphere-free ambiguity
\underline{N}_{p0}	A-priori normal matrix
\underline{N}_{pu}	Updated normal matrix;
Ω	Earth rotation angle
$\dot{\Omega}$	Angular velocity of the earth
P	Mean sea level barometric pressure measurement
\underline{P}	Weight matrix
P'	Evaluated mean sea level pressure
P_0	Mean sea level barometric pressure
P_{avg} and P_{amp}	Mean sea level barometric pressure yearly average and amplitude
P_1 and P_2	Pseudorange measurements on L1 and L2 frequencies
$pb_{r,i}$ and $pb_{s,i}$	Receiver and satellite carrier-phase initial phase bias, where i represents the carrier frequency (L1 or L2)
\underline{PCO}	Three-dimensional vector representing the satellite phase center offset
\underline{PCP}	Three-dimensional vector representing the satellite phase center position
P_{if} and Φ_{if}	Iono-free pseudorange and carrier-phase measurements
P'_{if} and Φ'_{if}	Corrected iono-free pseudorange and carrier-phase measurements

$P'_{\text{if}(C1,P2)}$	Pseudo-observable for the P1-C1 bias
$\tilde{P}'_{\text{if}(C1,C2)}$	Pseudo-observable for the P2-C2 bias
$\tilde{P}'_{\text{if}(C1,P2)}$	Pseudo-observable for the P1-C1 bias (simplified)
P_s	Surface barometric pressure
Φ_1 and Φ_2	Carrier-phase measurements on L1 and L2 frequencies
Φ_{gf} and P_{gf}	Geometry-free carrier-phase and pseudorange combinations
$\Phi_{\text{gf},\text{pl}}$	Leveled geometry-free carrier-phase
$\phi_{\text{g,p}}$ and $\phi_{\text{g},0}$	Geographic latitude of the piercing point and the station
R	Geometric distance between satellite and receiver antennas;
R_3	Rotation matrix along the Z axis
RH_0	Mean sea level relative humidity
RH_{avg} and RH_{amp}	Mean sea level relative humidity yearly average and amplitude
r_s	Slant residual
r_v	Vertical residual
σ_b	1-sigma bias uncertainty estimate
σ_I^2 , $\sigma_{\nabla\phi}^2$, and $\sigma_{\nabla\lambda}^2$	Process noise variances for parameters $I_{v,0}$, $\nabla\phi$, and $\nabla\lambda$, respectively
σ_ϕ and σ_p	Standard deviations at the zenith direction given for carrier-phase and pseudoranges
T	Slant neutral atmosphere delay
T	Surface temperature measurement (Chapter 7 only)

T'	Evaluated surface temperature
T_{avg} and T_{amp}	Mean sea level temperature yearly average and amplitude
T_0	Mean sea level temperature
T_d	Dew point temperature
T_m	Mean temperature of water vapour
$T_{r,\text{nom}}$	Nominal signal reception time
$T_{t,\text{GPS}}$	Signal transmission time in GPS time scale
$T'_{t,\text{GPS}}$	Approximate signal transmission time in GPS time scale
T_z	Zenith neutral atmosphere delay
\underline{x}	Vector of updated parameters
\underline{x}_0	Vector of a-priori parameters
X_{doy}	Computed meteorological parameter value for day of year
X_r , Y_r and Z_r	Receiver antenna coordinates
X^s , Y^s and Z^s	Satellite antenna coordinates at the signal transmission time
$X^{s,r}$, $Y^{s,r}$ and $Z^{s,r}$	Rotated satellite antenna coordinates at the signal transmission
	Time
\underline{w}	Misclosure vector

1. Introduction

Precise Point Positioning (PPP) is one of the existing techniques to determine point coordinates using a GPS (Global Positioning System) receiver. In this technique observations collected by a single receiver are used in order to determine the three components of the coordinates, as well as other parameters, such as the receiver clock error and total neutral atmosphere delay.

The PPP technique is the main object of this thesis. The main idea is that PPP can be used not only for positioning, but for a variety of tasks, such as GPS data analysis. The fact that the observation model used in this technique has to take into consideration most of the several effects present on GPS signals, and that observations are un-differenced (there are no differences between receivers or between satellites), makes PPP a powerful data analysis tool which is sensible to a variety of parameters. When the observation model is designed for positioning, most of these parameters (e.g., satellite clocks) are used as known quantities, but in this research the observation model was modified and enhanced to develop a PPP package that can be used as a tool for determining other parameters rather than position, receiver clock error and neutral atmosphere delay. These estimated parameters include ionospheric delay, code biases, satellite clock errors, and code multipath plus noise. In all of these cases there are innovations added to the technique, related to the way these quantities are estimated. In all cases the procedures are also suitable for real time, what makes PPP software a potential tool for wide area receiver

networks control and management. Depending on the type of the estimated parameters, they might simply serve as quantification in terms of data analysis and quality control, or they can be later used for positioning again (as known values).

One of the parameters used for positioning is the neutral atmosphere delay, also known as tropospheric delay. This delay is caused by the refraction suffered by GPS signals through the neutral part of the atmosphere. The prediction of the neutral atmosphere delays for positioning is also one of the subjects of this thesis. It is however treated differently from other parameter derivations because of the nature of their development and usage. Existing neutral atmosphere delay models have been studied in this thesis, and an enhanced model has been developed and has had its performance assessed. The development of the model is based on measured meteorological parameters, and the rationale of the model is established in order to make its use as practical as possible for users of positioning techniques, such as PPP.

1.1. Motivation

The original motivation of the thesis was related to the determination of the satellite non-integer phase biases, which could possibly be used in the attempt of fixing integer ambiguity values in PPP. During the process of developing a technique which could be used to determine such parameters, other problems appeared and the need of using a PPP package to solve those problems made clear that PPP could be potentially used as a

powerful data analysis tool. Given this possibility, efforts were made to investigate which type of parameters could be estimated, and in each case, how this could be done.

The general motivation of this thesis is the investigation on how a precise point positioning technique can be enhanced. The enhancements can be either related to using PPP as a tool for data analysis, or providing better a-priori information for a PPP engine, aiming at enhanced coordinates and convergence time of the solution. Therefore, the developments refer both to enhanced input information for positioning and to products generated with extended tools created in a PPP package.

1.2. Objectives and contributions

The main objectives of this work can be outlined as follows (ordered as they appear in the thesis text):

- Development of a technique to estimate ionospheric delays;
- Development of a technique to estimate satellite code biases;
- Development of a technique to estimate multipath plus noise of pseudorange measurements;
- Development of a technique to estimate satellite clock errors;
- Development of new neutral atmosphere model.

The scientific contributions of each objective are stated in the following paragraphs.

Development of a technique to estimate unbiased ionospheric delays: Ionospheric delays are not well resolved unless there is a good determination of biases involved in the measurements at different signal frequencies, which usually requires a network of tracking receivers to solve for satellite and receiver instrumental biases. The innovation of this approach is the determination of bias-free ionospheric delays, based on dual-frequency carrier-phase measurements from one single receiver;

Development of a technique to estimate multipath plus noise of pseudorange measurements: The innovation is the estimation of pseudorange multipath values using pseudorange and carrier-phase measurements inside a PPP engine. The difference with respect to other multipath estimation techniques is the fact that usually only the higher frequency components of multipath are determined. In this new technique several issues, such as ionospheric delays and carrier-phase ambiguities, are addressed in order to recover multipath values.

Development of a technique to estimate satellite code biases: Code biases are one of the relevant factors to be taken into account when processing data of a network with mixed receiver types, or using clock corrections for positioning with receiver types different from the ones used to generate the corrections. Usually these biases are estimated as a byproduct of the clock estimation process, using a network of receivers. The innovation of the approach in this thesis is the fact that these biases are estimated using a single station positioning model rather than a network clock adjustment model. Using a single

station positioning observation model makes this approach sensible to the same conditions as a positioning (and bias values) user.

Development of a technique to estimate satellite clock errors: When dealing with single receiver positioning, satellite clock corrections play a significant role in the data processing. These corrections are usually generated using pseudorange and carrier-phase measurements from a network of receivers. The innovative aspect is the development of an approach for the estimation of carrier-phase quality clock corrections using a single station which is suitable for real time applications, and could allow the integration between PPP and relative satellite positioning.

Development of a new neutral atmosphere model: Another fundamental parameter for positioning is the neutral atmosphere delay which is usually handled with a-priori information from prediction models, and sometimes also a residual delay parameter in the observation model. The innovation of this development is the creation of models which are suitable for wide area satellite based augmentation systems. The new development was based on a surface meteorological dataset, requiring a new approach to establish the model's parameters, however resulting in a more reliable model which keeps the simplicity and the practical usage procedure from earlier developments.

There are other contributions made with the development of this research, which do not necessarily have scientific value; however they are significant practical contributions, outlined below:

- Development of a precise point positioning software;
- Development of an online application for point positioning;
- Development of a neutral atmosphere model package for GNSS users.

The description of each of the practical contributions is stated in the following paragraphs.

Development of a precise point positioning software: As previously discussed, PPP is the main subject of this work, therefore a PPP software was needed in order to be used for implementing and testing novel techniques developed in this research. Even though the Department of Geodesy and Geomatics Engineering (GGE), its faculty members and its students had access to existing PPP packages and respective source codes, such as GPS-PPP (developed by Natural Resources Canada –NRCan) and BERNESE, a new package was developed. This package was named GPS Analysis and Positioning Software (GAPS, for short), where the word “Analysis” is part of the name due to the analysis tools developed and implement in it. The reasons for developing new in-house software are:

1. Learning – with the development of this new package from scratch, I had to go through all data processing details involved in PPP, getting experience with the technique, which was useful for the later new developments;

2. Control – having software running with all source code written by myself makes it easier to modify it, insert new procedures, as well as debugging it. There is also the assumption that these advantages would make the whole process less time consuming, where the time gained on modification and debugging would compensate the time spent to create the new software.

GAPS was developed in MatLab, and it is composed of around 150 functions linked by one main program, which manages the tasks required for GPS data processing. As of today, GAPS can be said to be a state-of-art precise point positioning package. After the development of GAPS, GGE became one of the research institutions having their own tool for PPP analysis and developments, as well as having know-how in terms of this technique.

Development of an online application for point positioning: One of the main tasks in developing software is testing it. This task gets easier if there are people actually using the program and assessing its performance. Because of this, GAPS was made available, initially for a limited group of users, so it could be tested. The way it was done was developing an online application interface via the internet, and creating the capability of auto processing within the software. The interface is a web page in which the user can upload his/her observation file and choose how he/she wants it to be processed.

Regarding the software itself, it was modified to be capable of downloading necessary files such as orbit and clock files from IGS (International GNSS Service) ftp server, to

automatically check for changes and update its internal files (such as satellite and receiver antenna file) if necessary, and to create result reports available to the user via the internet. Even though this on line tool was initially developed aiming at benefiting GAPS development, it showed to be an interesting tool to be available for GPS users in general. Nowadays online GAPS is available through GGE's research and learning resources web site page (<http://gge.unb.ca/Resources/Resources.html>).

Development of a neutral atmosphere model package for GNSS users: As previously mentioned, one of the topics dealt within this research was the development of neutral atmosphere models. Besides the development of new models, a pre-existent model, namely UNB3m, was validated and made available as part of the research. As it will be discussed later, UNB3m was validated using around three quarters of a million radiosonde soundings collected throughout North America. The model is available for GNSS users as a package of subroutines implemented in FORTRAN and MatLab. Besides the validation of the delay estimation subroutine, two variations of it were created: a subroutine for delay rates and one for meteorological parameters. The package can be accessed also at GGE's research and learning resources web site page (<http://gge.unb.ca/Resources/Resources.html>).

1.3. Outline of the thesis

This thesis is composed of 8 chapters. Chapter 1 is the introductory text, where the reader can have an idea about the topics that will be explored in the text, as well as

understanding the motivation and organization of the thesis. Chapter 2 explores the concepts of precise point positioning, and also presents a description of GAPS positioning engine implementation. Chapter 2 provides the basis for understanding the theory involved in following chapters. Chapters 3 to 7 explore each of the scientific contributions of this thesis. Each of these chapters presents: a brief theory about its subject; the developed technique and its innovative aspects; results obtained with the new technique with comparisons with third party results; and concluding remarks. They are ordered as previously shown on the contribution list. Even though the ordering is not obvious, it follows the development history of GAPS. Chapter 8 presents the thesis conclusions and recommendations.

2. Precise Point Positioning and GPS Analysis and Positioning Software

(GAPS)

2.1. A bit of history, and GAPS's role in PPP research and development

Precise point positioning (PPP) is a positioning technique in which a single receiver is used to determine coordinates. It is said to be “precise” because the so called “precise products” such as orbits and clocks are used in the data processing. These products were called “precise” because they were produced by means of post-processing of GPS data from several world-wide distributed monitoring ground stations, and provided information of better quality than the broadcast ephemeris message. The term PPP was proposed for the first time by Heroux and Kouba [1995], when they proposed the use of “precise” satellite orbits and clocks for point positioning. At that time, the Geodetic Survey Division (GSD), Natural Resources Canada (NRCAN) was already generating post-processed GPS satellite orbits and clocks in a standard format which were used to contribute to the International GNSS Service (IGS). They claimed that these products could be included in a point positioning software interface and provide high precision to users operating a single GPS receiver. And they were absolutely right. Although at that time they presented a simple approach that could only offer precision of about one meter, this was the very starting point of PPP development.

Later, Zumberge et. al [1997] proposed the use of PPP for analysis of data from hundreds to thousands of sites every day, with achievable results comparable in quality to what could be obtained with the simultaneous analysis of all data. This publication became one of the most known early references on PPP.

In 2001 Kouba and Heroux [2001] detailed a post-processing approach using undifferenced dual-frequency pseudorange and carrier phase observations along with IGS precise orbit products, for stand-alone precise geodetic point positioning (static or kinematic), now with cm-level precision. At that time, they already described the earth- and space-based models that must be implemented to achieve cm-level positioning. They also discussed the capability of obtaining station neutral atmosphere zenith delays with cm precision and GPS receiver clock estimates precise to 0.1 ns.

By this time PPP was already a technique widely known by the GPS community, and several papers were published highlighting different uses for single point positioning with precise orbits and clock products. For example, Bisnath and Langley [2001] proposed a geometric approach based on a kinematic, sequential least-squares filter/smoothing to be used with data from LEO's (low earth orbiters) GPS receivers and the IGS precise orbits and clock products, aiming at decimeter precision.

PPP technique established itself as a powerful positioning technique in which cm-level accuracies could be obtained. However it has always had a major drawback, which is the convergence time. The time a PPP solution takes to achieve sub-decimeter level

accuracy, which might be as high as a few tens of minutes, is nowadays the greatest hurdle for using it as a real-time world-wide high-accuracy GNSS positioning tool, since the market often requires solution (re-) initialization of a few seconds. In view of that, several research centers started research projects in the direction of introducing an ambiguity fixing process inside a PPP engine, so that the solution initialization time could go down. This was the case of Gabor and Nerem [2002], who proposed a method for calibrating satellite-dependent phase biases with a tracking network, which could later be used for eliminating these quantities present on the measurements for a stand-alone receiver, and therefore come up with ambiguities of integer nature inside the PPP engine. The method was based on the derivation of a first set of wide-lane phase-biases, based on a wide-lane phase and narrow-lane code geometry-ionosphere-free combination (also known as Melbourne-Wubben combination [Melbourne, 1985]; [Wubben, 1985]). If that is done successfully, then a second set of ambiguities could be fixed, which will have an effective wavelength of around 10 cm. At that time they concluded that the level of the existing orbit errors would not allow fixing this second set of ambiguities. Gao and Shen [2002] introduced a different method, which was not based on satellite bias calibration, but on a PPP engine built-in technique which tried to exploit integer nature of phase ambiguity. However, as time elapsed, it has become common sense within the PPP research community that it is necessary to calibrate satellite-dependent phase biases in order to fix ambiguities in PPP. This can be noticed by the increasing number of papers on that direction during the last years, such as Leandro et al. [2006], Ge et al. [2007], Banville et al. [2008], Collins [2008], and Laurichesse et al. [2008], all of them proposing the calibration of satellite phase biases. The later four publications use of the same

concept as the one proposed by Garbor and Nerem (fixing at first wide-lane ambiguities and later the other integer ambiguities needed to form the carrier-phase iono-free combination, with an effective wavelength of around 10 cm), but with some reformulation and/or additional analysis.

GAPS started to be developed in 2006, with the objective of being a tool for satellite phase-bias calibration and use. The technique which was described in the 2006 publication was based on a de-correlation of L1 and L2 ambiguities and biases, by means of PPP-based ionospheric modeling (whose procedure is described in chapter 3). The reason for looking for a different technique is the fact that in order to reliably fix the second set of ambiguities as used in Garbor and Nerem approach, it is necessary to have all geometry-related effects (neutral atmosphere, receiver coordinates and receiver clock) modeled with uncertainties reasonably near a decimeter, and this is something which might take a long time to be achieved – in some cases when the PPP solution has already converged to that level of accuracy ambiguity fixing might bring only little improvement. The concern Garbor and Nerem raised back in 2001 is still a problem to be solved in my point of view, simply by looking at the error budget of PPP. This means that the PPP float solution convergence time needs to be improved for assuring that using ambiguity fixing techniques will bring a consistent improvement to the position solution. The existing ambiguity fixing techniques might also need modifications so they can be successfully used for PPP. During the research which has been done towards an improved solution for PPP, I started to enhance GAPS observation model, and when looking into certain aspects of it, I realized that the PPP engine could be enhanced, or, could have

additional components which would potentially help on the ongoing data analysis, and on the improvement of the positioning solution. These components are presented in this thesis, as a significant contribution towards the enhancement of PPP solutions.

2.2. The positioning observation model

As mentioned in the previous section, PPP is a positioning technique in which a single receiver is used to determine coordinates, using the so called “precise products” such as orbits and clocks in the data processing. More than that, if one wants to have the ultimate achievable accuracy with PPP, all necessary observation corrections should be taken into account to achieve the best possible accuracy. Such corrections include tides, relativistic effects, and receiver and satellite antenna phase center variation among others.

Depending on the type of receiver being used (e.g. code only or code and phase; single or dual frequency), some of those corrections can be disregarded, or alternatively further precise products might be needed, such as ionospheric grids in case of single frequency receivers. If the higher possible accuracy is targeted, a “geodetic” receiver must be used, with dual frequency measurements of pseudorange and carrier-phase. In this case, other aspects are also important, such as treating the carrier-phase as an independent measurement (rather than using them to simply filter the pseudoranges), which leads to an ambiguity parameter estimation for each satellite, and also the estimation of residual neutral atmosphere delays (NAD), since NAD prediction models are not accurate enough for this type of positioning.

The PPP observation model is pretty much a standard model nowadays. Here, the word “standard” is being used because most of other PPP packages, such as CSRS-PPP [Tétreault et al. 2005], P3 [Gao and Chen, 2004] and GIPSY [Zumberge et al. 1997], use this model, with ionospheric free combination of pseudorange and carrier-phase. A few differences can be found between them, such as the estimation process of NAD (e.g., as random walk, or fixed values for given time intervals).

The precise point positioning package developed in the scope of this thesis is called GAPS, an acronym for GPS Analysis and Positioning Software. As mentioned before, the word “Analysis” is used due to the GAPS’s data analysis capabilities, i.e., the software has more applications than positioning. These applications will be discussed in the next chapters of this thesis. In this chapter I am focusing on the positioning aspect of GAPS. In order to understand the positioning procedure we can start with the equations for carrier-phase:

$$\Phi_1 = R + c(dT - dt) + T - I + \lambda_1 N_1 + hd_{r,1} - hd_{s,1} + pb_{r,1} - pb_{s,1} + m_1 + e_1, \quad (2.1)$$

and

$$\Phi_2 = R + c(dT - dt) + T - \gamma I + \lambda_2 N_2 + hd_{r,2} - hd_{s,2} + pb_{r,2} - pb_{s,2} + m_2 + e_2, \quad (2.2)$$

where: Φ_1 and Φ_2 are carrier-phase measurements on L1 and L2 frequencies, respectively, in metric units; R is the geometric distance between satellite and receiver antennas, in meters; c is the speed of light, in meters per second; dT and dt are receiver and satellite clock errors, respectively, in seconds; T is the neutral atmosphere delay, in meters; I is the L1 frequency ionosphere delay, in meters; γ is the factor to convert the ionospheric delay from L1 to L2 frequency ($77^2/60^2$), unitless; λ_1 and λ_2 are carrier-phase wavelengths on L1 and L2 frequencies, respectively, in meters; N_1 and N_2 are carrier-phase integer ambiguities on L1 and L2 frequencies, respectively, in cycles; $hd_{r,i}$ and $hd_{s,i}$ are receiver and satellite carrier-phase hardware delays, respectively, in metric units, where i represents the carrier frequency (L1 or L2); $pb_{r,i}$ and $pb_{s,i}$ are receiver and satellite carrier-phase initial phase bias, respectively, in metric units, where i represents the carrier frequency (L1 or L2); m_1 and m_2 are carrier-phase multipath on L1 and L2 frequencies, respectively, in meters; and e_1 and e_2 are other un-modeled errors of carrier-phase measurements on L1 and L2 frequencies, respectively, in meters.

Similar equations can be formed for pseudoranges, as follows:

$$P_1 = R + c(dT - dt) + T + I + HD_{r,1} - HD_{s,1} + M_1 + E_1, \quad (2.3)$$

and

$$P_2 = R + c(dT - dt) + T + \gamma I + HD_{r,2} - HD_{s,2} + M_2 + E_2, \quad (2.4)$$

where: P_1 and P_2 are pseudorange measurements on L1 and L2 frequencies, respectively, in metric units; $HD_{r,i}$ and $HD_{s,i}$ are receiver and satellite pseudorange hardware delays, respectively, in metric units, where i represents the carrier frequency (L1 or L2); M_1 and M_2 are pseudorange multipath on L1 and L2 frequencies, respectively, in meters; and E_1 and E_2 are other un-modeled errors of pseudorange measurements on L1 and L2 frequencies, respectively, in meters. The other symbols have the same meaning as in equations 2.1 and 2.2.

In order to mathematically eliminate the first-order ionospheric delay from carrier-phase and pseudorange measurements an ionospheric-free combination of the two frequencies can be used. This combination takes advantage of the fact the ionosphere is a dispersive medium, and thus the magnitude of the first-order delay is inversely proportional to the frequency squared, as:

$$I_i = \frac{40.3 \text{ TEC}}{f_i^2}, \quad (2.5)$$

where I_i is the ionospheric delay on the frequency i in metric units, TEC is the total integrated electron content, and f_i is the frequency of the signal, in hertz. The carrier and pseudorange ionospheric-free combinations can be formed as follows:

$$\Phi_{if} = \frac{f_1^2}{f_1^2 - f_2^2} \Phi_1 - \frac{f_2^2}{f_1^2 - f_2^2} \Phi_2, \quad (2.6)$$

and

$$P_{if} = \frac{f_1^2}{f_1^2 - f_2^2} P_1 - \frac{f_2^2}{f_1^2 - f_2^2} P_2. \quad (2.7)$$

One of the drawbacks in the iono-free combination is the measurement noise, about three times higher than for L1 or L2. The observation equations for the iono-free combinations read:

$$\Phi_{if} = R + c(dT - dt) + T + \lambda_{if} N_{if} + hd_{r,if} - hd_{s,if} + pb_{r,if} - pb_{s,if} + m_{if} + e_{if}, \quad (2.8)$$

and

$$P_{if} = R + c(dT - dt) + T + HD_{r,if} - HD_{s,if} + M_{if} + E_{if}. \quad (2.9)$$

The ionospheric delay terms are not present in the previous two equations, since they were eliminated in the iono-free combination operation. The use of this linear combination implies that respective wavelengths and ambiguities are also combined, resulting in:

$$\lambda_{\text{if}} = \frac{f_1^2}{f_1^2 - f_2^2} \lambda_1 - \frac{f_2^2}{f_1^2 - f_2^2} \lambda_2, \quad (2.10)$$

and

$$N_{\text{if}} = \frac{f_1^2}{f_1^2 - f_2^2} N_1 - \frac{f_2^2}{f_1^2 - f_2^2} N_2, \quad (2.11)$$

It is easy to conclude that because the coefficients multiplying the ambiguities in the equation above are not integers, the resulting ionosphere-free ambiguity (N_{if}) is also not an integer, as opposed to ambiguities on L1 (N_1) and L2 (N_2). It is possible to find coefficients that keep the integer nature of the ambiguity; however those are not practically effective as the wavelength gets reduced, and the noise amplified.

The observation equations given by equations 2.8 and 2.9 can be simplified considering that the receiver's code hardware delay will be absorbed by the receiver clock parameter, as:

$$c \cdot dT' = c \cdot dT + HD_{r,\text{if}}, \quad (2.12)$$

or similarly:

$$dT' = dT + \frac{HD_{r,\text{if}}}{c}, \quad (2.13)$$

since dT' and dT are defined in seconds, and $HD_{r,if}$ is defined in meters.

The receiver's code hardware delay gets absorbed by the clock parameter because regardless the fact that carrier-phase measurements usually have more weight, they are ambiguous (they have an ambiguity term) and thus the clock datum in the PPP solution comes really from pseudorange observations. The satellites code hardware delays ($HD_{s,if}$) have to be accounted for by applying known differential code biases to the measurements. It is important to note that in some cases it is not necessary to correct pseudoranges for satellite code biases (see chapter 4). In order to include these cases in a general formulation, one should make the hardware delay correction equal to zero. This procedure will be discussed in detail later in this chapter. The corrected pseudorange reads:

$$P'_{if} = P_{if} + HD_{s,if} . \quad (2.14)$$

The observation equations can then be rearranged as:

$$\Phi_{if} = R + c(dT' - dt) + T + \lambda_{if} N_{if} + hd_{r,if} - hd_{s,if} + pb_{r,if} - pb_{s,if} - HD_{r,if} + m_{if} + e_{if} , \quad (2.15)$$

and

$$P'_{if} = R + c(dT'-dt) + T + M_{if} + E_{if} . \quad (2.16)$$

Because I am not making the assumption that code and carrier hardware delays are the same a code hardware delay term is now present in the carrier-phase observation equation.

Assuming the hardware delays and phase biases are terms reasonably stable over time (see for instance chapter 4), they are actually absorbed by the iono-free ambiguity parameter, according to:

$$\lambda_{if} N'_{if} = \lambda_{if} N_{if} + hd_{r,if} - hd_{s,if} + pb_{r,if} - pb_{s,if} + HD_{r,if} , \quad (2.17)$$

or similarly:

$$N'_{if} = N_{if} + \frac{hd_{r,if} - hd_{s,if} + pb_{r,if} - pb_{s,if} + HD_{r,if}}{\lambda_{if}} , \quad (2.18)$$

since the ambiguity terms are being defined in cycles, while biases are being defined in meters.

Thus the carrier-phase observation equation becomes:

$$\Phi_{if} = R + c(dT'-dt) + T + \lambda_{if} N'_{if} + m_{if} + e_{if} . \quad (2.19)$$

Therefore it is easy to conclude that the PPP float ambiguity parameter is not a pure ambiguity, but an iono-free combination of two integer (pure) ambiguities (N_1 and N_2) added to a collection of hardware delays and initial phase biases (converted to cycle units, as shown in equation 2.18).

As mentioned earlier, one of the advantages of Precise Point Positioning is the high accuracy which can be obtained with a single receiver. However, to get good results the observations need to be corrected for a variety of effects before they are used. Each of these corrections will be discussed later. We should then consider the corrected observations:

$$P'_{if} = P_{if} + C_{if} , \quad (2.20)$$

and

$$\Phi'_{if} = \Phi_{if} + c_{if} , \quad (2.21)$$

where P'_{if} and Φ'_{if} are the corrected pseudorange and carrier-phase measurements, respectively; and C_{if} and c_{if} are the pseudorange and carrier-phase corrections, respectively. The pseudorange correction term includes the hardware delay as shown in

equation 2.14, so equation 2.14 can be seen as a particular case of equation 2.20. The corrected carrier-phase observation equation reads:

$$\Phi'_{if} = R + c(dT' - dt) + T + \lambda_{if} N'_{if} + m_{if} + e_{if} . \quad (2.22)$$

The difference between equations 2.22 and 2.19 is the fact in equation 2.22 the carrier-phase measurement (Φ'_{if}) is a corrected observation.

2.3. Observations adjustment

In this section I will explore the adjustment of the observations performed in GAPS to determine the parameters pertinent to positioning. These parameters are the receiver coordinates, the receiver clock error, the zenith troposphere delay and the carrier-phase ambiguities. In the equations of this section I will ignore the multipath (M_{if} and m_{if}) and noise (E_{if} and e_{if}) terms, since they are the non-modeled part of the positioning model. Let us start assuming we know a-priori values for all parameters, so we can rewrite the observation equations as below. If it is not possible to come up with approximate values for parameters such as receiver clock error and receiver position, zeros can be used instead. In GAPS the ambiguities are always initialized with zeros, and NAD with the delay provided by UNB3m model. GAPS's algorithm has been designed to handle zeros as a-priori information.

$$\Phi'_{if} = (R_0 + \delta R) + c((dT'_0 + \delta dT') - dt) + (T_0 + \delta T) + \lambda_{if} (N'_{if,0} + \delta N'_{if}) , \quad (2.23)$$

and

$$P'_{if} = (R_0 + \delta R) + c((dT'_0 + \delta dT') - dt) + (T_0 + \delta T). \quad (2.24)$$

The subscript zero indicates the a-priori values being used, and the terms accompanied with deltas are the “errors” introduced when using those a-priori values, or, in other words, the difference between the observed value and the a-priori value of each parameter. These “errors” are going to be the updates we want to compute, so the a-priori values can be corrected to approach the observed values of each parameter. We can rewrite the equations above, now using the partial derivatives of each parameter with respect to the observation:

$$\begin{aligned} \Phi'_{if} = R_0 + \frac{\partial \Phi'_{if}}{\partial X_r} \delta X_r + \frac{\partial \Phi'_{if}}{\partial Y_r} \delta Y_r + \frac{\partial \Phi'_{if}}{\partial Z_r} \delta Z_r + cdT'_0 + \frac{\partial \Phi'_{if}}{\partial dT'} \delta dT' - cdt + \\ T_0 + \frac{\partial \Phi'_{if}}{\partial T_z} \delta T_z + \lambda_{if} N'_{if,0} + \frac{\partial \Phi'_{if}}{\partial N'_{if}} \delta N'_{if} \end{aligned}, \quad (2.25)$$

and

$$P'_{if} = R_0 + \frac{\partial P'_{if}}{\partial X_r} \delta X_r + \frac{\partial P'_{if}}{\partial Y_r} \delta Y_r + \frac{\partial P'_{if}}{\partial Z_r} \delta Z_r + cdT'_0 + \frac{\partial P'_{if}}{\partial dT'} \delta dT' - cdt + T_0 + \frac{\partial P'_{if}}{\partial T_z} \delta T_z, \quad (2.26)$$

where X_r , Y_r and Z_r stand for the receiver cartesian coordinates, and T_z is the zenith neutral atmosphere delay. Now the parameters are actually the updates (δX_r , δY_r , δZ_r , $\delta dT'$, and δT_z) that each parameter should receive to get closer to its observed value. The equations can then be rearranged with the parameters on the left hand side and the rest of it on the right hand side:

$$\frac{\partial \Phi'_{if}}{\partial X_r} \delta X_r + \frac{\partial \Phi'_{if}}{\partial Y_r} \delta Y_r + \frac{\partial \Phi'_{if}}{\partial Z_r} \delta Z_r + \frac{\partial \Phi'_{if}}{\partial dT'} \delta dT' + \frac{\partial \Phi'_{if}}{\partial T_z} \delta T_z + \frac{\partial \Phi'_{if}}{\partial N'_{if}} \delta N'_{if} = \Phi'_{if} - R_0 - cdT'_0 + cdt - T_0 - \lambda_{if} N'_{if,0}, \quad (2.27)$$

and

$$\frac{\partial P'_{if}}{\partial X_r} \delta X_r + \frac{\partial P'_{if}}{\partial Y_r} \delta Y_r + \frac{\partial P'_{if}}{\partial Z_r} \delta Z_r + \frac{\partial P'_{if}}{\partial dT'} \delta dT' + \frac{\partial P'_{if}}{\partial T_z} \delta T_z = P'_{if} - R_0 - cdT'_0 + cdt - T_0. \quad (2.28)$$

The partial derivatives are evaluated as follows:

$$\frac{\partial \Phi'_{if}}{\partial X_r} = \frac{\partial P'_{if}}{\partial X_r} = -\frac{X^s - X_r}{R_0}, \quad (2.29)$$

$$\frac{\partial \Phi'_{if}}{\partial Y_r} = \frac{\partial P'_{if}}{\partial Y_r} = -\frac{Y^s - Y_r}{R_0}, \quad (2.30)$$

$$\frac{\partial \Phi'_{if}}{\partial Z_r} = \frac{\partial P'_{if}}{\partial Z_r} = -\frac{Z^s - Z_r}{R_0}, \quad (2.31)$$

where X^s , Y^s and Z^s stand for the satellites coordinates at the signal transmission time,

$$\frac{\partial \Phi'_{if}}{\partial dT'} = \frac{\partial P'_{if}}{\partial dT'} = c, \quad (2.32)$$

$$\frac{\partial \Phi'_{if}}{\partial T_z} = \frac{\partial P'_{if}}{\partial T_z} = mf_{nh}, \quad (2.33)$$

and

$$\frac{\partial \Phi'_{if}}{\partial N'_{if}} = \lambda_{if}, \quad (2.34)$$

where mf_{nh} is the non-hydrostatic mapping function. In case of GAPS, Niell [Niell, 1996] mapping function is used. The non-hydrostatic mapping function is used because it is assumed that the a-priori zenith delay provided by UNB3m model can account for most of the hydrostatic delay, and thus, most of the residual delay is actually of non-hydrostatic nature. More details about UNB3m performance will be discussed in a later chapter of this thesis.

It is worth taking a closer look in one of the elements mentioned above: the geometric range. Even though it looks like a simple computation of vector length, there are some complicating factors associated with it. This will be discussed later in this chapter.

In order to compute updates for the parameters, observation of several satellites over several epochs are used. These observations are put together in a least squares adjustment filter. There are several ways to perform the observations adjustment, and the procedure I am going to describe here is the one used by GAPS.

In GAPS the parameter updates are computed at every epoch of observation, according to:

$$\underline{\delta} = (\underline{A}^t \underline{P} \underline{A} + \underline{C}_x)^{-1} \underline{A}^t \underline{P} \underline{w}, \quad (2.35)$$

where $\underline{\delta}$ is the parameters update vector, \underline{A} is the design matrix, \underline{P} is the weight matrix, \underline{C}_x is the parameters covariance matrix, and \underline{w} is the misclosure vector. These elements are discussed in the following paragraphs.

The vector of updates consists of updates for coordinates, residual neutral atmosphere delay, receiver clock and carrier-phase ambiguities of the satellites s_1, s_2, \dots, s_n as follows:

$$\underline{\delta} = \begin{bmatrix} \delta X_r \\ \delta Y_r \\ \delta Z_r \\ \delta dT' \\ \delta T_z \\ \delta N'_{if,s1} \\ \vdots \\ \delta N'_{if,sn} \end{bmatrix}. \quad (2.36)$$

The design matrix is formed as follows:

$$\underline{A} = \begin{bmatrix} \frac{\partial \Phi'_{if,s1}}{\partial X_r} & \frac{\partial \Phi'_{if,s1}}{\partial Y_r} & \frac{\partial \Phi'_{if,s1}}{\partial Z_r} & \frac{\partial \Phi'_{if,s1}}{\partial dT'} & \frac{\partial \Phi'_{if,s1}}{\partial T_z} & \frac{\partial \Phi'_{if,s1}}{\partial N_{if,s1}} & 0 & 0 & \dots & 0 \\ \frac{\partial P'_{if,s1}}{\partial X_r} & \frac{\partial P'_{if,s1}}{\partial Y_r} & \frac{\partial P'_{if,s1}}{\partial Z_r} & \frac{\partial P'_{if,s1}}{\partial dT'} & \frac{\partial P'_{if,s1}}{\partial T_z} & 0 & 0 & 0 & \dots & 0 \\ \frac{\partial \Phi'_{if,s2}}{\partial X_r} & \frac{\partial \Phi'_{if,s2}}{\partial Y_r} & \frac{\partial \Phi'_{if,s2}}{\partial Z_r} & \frac{\partial \Phi'_{if,s2}}{\partial dT'} & \frac{\partial \Phi'_{if,s2}}{\partial T_z} & 0 & \frac{\partial \Phi'_{if,s2}}{\partial N_{if,s2}} & 0 & \dots & 0 \\ \frac{\partial P'_{if,s2}}{\partial X_r} & \frac{\partial P'_{if,s2}}{\partial Y_r} & \frac{\partial P'_{if,s2}}{\partial Z_r} & \frac{\partial P'_{if,s2}}{\partial dT'} & \frac{\partial P'_{if,s2}}{\partial T_z} & 0 & 0 & 0 & \dots & 0 \\ \frac{\partial \Phi'_{if,s3}}{\partial X_r} & \frac{\partial \Phi'_{if,s3}}{\partial Y_r} & \frac{\partial \Phi'_{if,s3}}{\partial Z_r} & \frac{\partial \Phi'_{if,s3}}{\partial dT'} & \frac{\partial \Phi'_{if,s3}}{\partial T_z} & 0 & 0 & \frac{\partial \Phi'_{if,s3}}{\partial N_{if,s3}} & \dots & 0 \\ \frac{\partial P'_{if,s3}}{\partial X_r} & \frac{\partial P'_{if,s3}}{\partial Y_r} & \frac{\partial P'_{if,s3}}{\partial Z_r} & \frac{\partial P'_{if,s3}}{\partial dT'} & \frac{\partial P'_{if,s3}}{\partial T_z} & 0 & 0 & 0 & \dots & 0 \\ \vdots & \vdots & \vdots & \vdots & \vdots & \vdots & \vdots & \vdots & \vdots & \vdots \\ \frac{\partial \Phi'_{if,sn}}{\partial X_r} & \frac{\partial \Phi'_{if,sn}}{\partial Y_r} & \frac{\partial \Phi'_{if,sn}}{\partial Z_r} & \frac{\partial \Phi'_{if,sn}}{\partial dT'} & \frac{\partial \Phi'_{if,sn}}{\partial T_z} & 0 & 0 & 0 & \dots & \frac{\partial \Phi'_{if,sn}}{\partial N_{if,sn}} \\ \frac{\partial P'_{if,sn}}{\partial X_r} & \frac{\partial P'_{if,sn}}{\partial Y_r} & \frac{\partial P'_{if,sn}}{\partial Z_r} & \frac{\partial P'_{if,sn}}{\partial dT'} & \frac{\partial P'_{if,sn}}{\partial T_z} & 0 & 0 & 0 & \dots & 0 \end{bmatrix}, \quad (2.37)$$

where the partial derivatives are evaluated as previously shown. As it can be noticed in the equation above, the design matrix is formed with its rows ordered for observed satellites, with odd rows containing carrier-phase measurements partials, and even rows with pseudorange partials. The ordering used does not influence the results at all, and the only requirement with respect to it is that the ordering should be the same as in the

weight matrix and misclosure vector. The weight matrix is formed using elevation angle dependent values, as:

$$P_{\Phi,s} = \frac{\sin(el)^2}{\sigma_{\Phi}^2}, \quad (2.38)$$

for carrier-phase, and

$$P_{P,s} = \frac{\sin(el)^2}{\sigma_p^2}, \quad (2.39)$$

for pseudorange, where σ_{Φ} and σ_p are the standard deviations at the zenith direction given for carrier-phase and pseudoranges, with standard values of 0.02 m and 2.00 m, respectively. The weight matrix therefore reads:

$$\underline{P} = \begin{bmatrix} P_{\Phi,s1} & 0 & 0 & 0 & 0 & 0 & \dots & 0 & 0 \\ 0 & P_{P,s1} & 0 & 0 & 0 & 0 & \dots & 0 & 0 \\ 0 & 0 & P_{\Phi,s2} & 0 & 0 & 0 & \dots & 0 & 0 \\ 0 & 0 & 0 & P_{P,s2} & 0 & 0 & \dots & 0 & 0 \\ 0 & 0 & 0 & 0 & P_{\Phi,s3} & 0 & \dots & 0 & 0 \\ 0 & 0 & 0 & 0 & 0 & P_{P,s3} & \dots & 0 & 0 \\ \vdots & \vdots & \vdots & \vdots & \vdots & \vdots & \ddots & 0 & 0 \\ 0 & 0 & 0 & 0 & 0 & 0 & 0 & P_{\Phi,sn} & 0 \\ 0 & 0 & 0 & 0 & 0 & 0 & 0 & 0 & P_{P,sn} \end{bmatrix}. \quad (2.40)$$

As it can be seen, no correlations are considered between any of the measurements, and therefore the weight matrix is a diagonal matrix. The misclosure vector is basically the

difference between the observed carrier-phase or pseudorange and their modeled values, computed with the parameter values as known at the time of the update. Misclosure vector values are computed as follows:

$$w_{\Phi} = \Phi'_{if} - R_0 - cdT'_0 + cdt - T_0 - \lambda_{if} N'_{if,0}, \quad (2.41)$$

and

$$w_P = P'_{if} - R_0 - cdT'_0 + cdt - T_0. \quad (2.42)$$

Following the same structure as used for design and weight matrices, the misclosure vector is formed as follows:

$$\underline{w} = \begin{bmatrix} w_{\Phi,s1} \\ w_{P,s1} \\ w_{\Phi,s2} \\ w_{P,s2} \\ w_{\Phi,s3} \\ w_{P,s3} \\ \vdots \\ w_{\Phi,sn} \\ w_{P,sn} \end{bmatrix}. \quad (2.43)$$

The parameters' covariance matrix consists of the variances and covariances for position, receiver clock, neutral atmosphere delay, and ambiguities. The equation below shows an

example of the upper triangle of a parameters covariance matrix. There is no need of showing the whole matrix, because it is symmetric.

$$\underline{C}_x = \begin{bmatrix} \sigma_X^2 & \sigma_{XY} & \sigma_{XZ} & \sigma_{XdT} & \sigma_{XT_z} & \sigma_{XN_{if,s1}} & \sigma_{XN_{if,s2}} & \cdots & \sigma_{XN_{if,sn}} \\ & \sigma_Y^2 & \sigma_{YZ} & \sigma_{YdT} & \sigma_{YT_z} & \sigma_{YN_{if,s1}} & \sigma_{YN_{if,s2}} & \cdots & \sigma_{YN_{if,sn}} \\ & & \sigma_Z^2 & \sigma_{ZdT} & \sigma_{ZT_z} & \sigma_{ZN_{if,s1}} & \sigma_{ZN_{if,s2}} & \cdots & \sigma_{ZN_{if,sn}} \\ & & & \sigma_{dT}^2 & \sigma_{dT_z} & \sigma_{dT_{N_{if,s1}}} & \sigma_{dT_{N_{if,s2}}} & \cdots & \sigma_{dT_{N_{if,sn}}} \\ & & & & \sigma_{T_z}^2 & \sigma_{T_z N_{if,s1}} & \sigma_{T_z N_{if,s2}} & \cdots & \sigma_{T_z N_{if,sn}} \\ & & & & & \sigma_{N_{if,s1}}^2 & \sigma_{N_{if,s1} N_{if,s2}} & \cdots & \sigma_{N_{if,s1} N_{if,sn}} \\ & & & & & & \sigma_{N_{if,s2}}^2 & \cdots & \sigma_{N_{if,s2} N_{if,sn}} \\ & & & & & & & \ddots & \vdots \\ & & & & & & & & \sigma_{N_{if,sn}}^2 \end{bmatrix}. \quad (2.44)$$

In the next sub-sections, details regarding computations will be discussed. First, the procedure for the geometric range is shown, and later the corrections applied to carrier-phase and pseudoranges (as shown in equations 2.20 and 2.21).

2.3.1. Geometric range computation

There are two fundamental quantities needed for the geometric range computation: the receiver's and satellite's coordinates. The receiver coordinates come from the latest computed coordinates, which are used as a-priori values for the current position update. When running the filter for the first time, approximate coordinates can be used (such as coordinates from RINEX file header), or even a vector of zeros. Let us assume in this section that we have approximate coordinates for the receiver. The second important quantity is the satellite position. In case of GAPS, these coordinates are determined using IGS (International GNSS Service) precise orbits. The coordinates of the satellite have to

be determined for the time when the signal was transmitted - the transmission time. Since the time tags we have available at the receiver are the nominal reception time, we do not know before hand what time the signal was transmitted by the satellite ($T_{t, \text{GPS}}$). In order to determine it, we can use the pseudorange measurement as follows:

$$T_{t, \text{GPS}} = T_{r, \text{nom}} - \frac{P}{c} - dt, \quad (2.45)$$

where $T_{t, \text{GPS}}$ is the transmission time in GPS time scale, $T_{r, \text{nom}}$ is the nominal reception time (the receiver time tags), P is the pseudorange measurement, c is the speed of light and dt is the satellite clock error. The pseudorange measurement to be used in this computation does not need to have any correction applied, such as troposphere or ionosphere delay corrections, since the impact of these effects on the time of transmission is negligible. It implies that pseudorange measurements from any frequency can be used. In fact, it is very important to understand that the clock errors present in the pseudorange measurements are in accordance with the receiver time tag (which also has the same receiver clock error, and thus the receiver clock error gets eliminated in the computation above), so the pseudorange should not be corrected for receiver clock offset before being used for orbits determination. Because the measurement has also the effect of the satellite clock error dt , it has to be accounted for. Ideally, the satellite clock error should be also computed for the transmission time as computed above, however the variation of the computed value of the satellite clock when accounting for the clock error as in equation 2.45 is usually negligible, i.e.:

$$\frac{\partial dt}{\partial t}.dt \cong 0, \quad (2.46)$$

so the approximate transmission time ($T'_{t, \text{GPS}}$) for satellite clock error computation purposes can be determined using only the pseudorange, as shown below:

$$T'_{t, \text{GPS}} = T_{r, \text{nom}} - \frac{P}{c}. \quad (2.47)$$

The use of equation 2.47 avoids the use of iterations, and satellite clock and orbits can be computed in a straightforward procedure.

After satellite coordinates are determined, the range could be computed as:

$$R = \sqrt{(X^s - X_r)^2 + (Y^s - Y_r)^2 + (Z^s - Z_r)^2}. \quad (2.48)$$

However, there is another effect which should be taken care of, which is called Sagnac effect. Because the earth rotates during the travel time of the signal, the coordinate system (the earth-centered and earth-fixed cartesian coordinate system) also rotates, and the satellite coordinates should refer to this “rotated” coordinate system. In order to correct for this effect, the angle of rotation during the travel time has to be determined as:

$$\Omega = \dot{\Omega} \cdot \frac{R}{c}, \quad (2.49)$$

where Ω is the rotation angle and $\dot{\Omega}$ is the angular velocity of the earth. The satellite coordinates can then be corrected by using a rotation matrix:

$$\begin{bmatrix} X^{s,r} \\ Y^{s,r} \\ Z^{s,r} \end{bmatrix} = R_3 \cdot \begin{bmatrix} X^s \\ Y^s \\ Z^s \end{bmatrix}, \quad (2.50)$$

where the superscript r stands for “rotated”, and R_3 is the rotation matrix along the Z axis:

$$R_3 = \begin{bmatrix} \cos(\Omega) & \sin(\Omega) & 0 \\ -\sin(\Omega) & \cos(\Omega) & 0 \\ 0 & 0 & 1 \end{bmatrix}. \quad (2.51)$$

The geometric range can then be recomputed with the satellite rotated coordinates:

$$R = \sqrt{(X^{s,r} - X_r)^2 + (Y^{s,r} - Y_r)^2 + (Z^{s,r} - Z_r)^2}. \quad (2.52)$$

This procedure (equations 2.35 to 2.39) often requires iterations to achieve the optimal geometric range.

2.4. Corrections

As mentioned before, there are a few corrections which have to be applied to carrier-phase and pseudorange measurements in addition to other commonly known effects (such as relativistic correction) in order to have a complete (adequate) observation model in PPP. This aspect is a limiting factor to achieve cm-level accuracy, as it is possible today, with PPP. All corrections accounted for by GAPS are listed below and will be discussed in the next subsections.

- Satellite antenna phase center offset and variation
- Receiver antenna phase center offset and variation
- Solid earth tides
- Ocean tide loading
- Differential code biases
- Phase wind-up effect

2.4.1. Satellite antenna phase center offset and variation

This section discusses the correction due to the satellite antenna phase center (APC) offset and variation, assuming that the satellite orbits being used for positioning are referred to the satellite center of mass, such as IGS orbits. This is not the case of the broadcast orbits, which do not need to receive such a correction.

Satellite orbits refer to the satellite's center of mass, whereas the measurements refer to the antenna phase center. Therefore, it is necessary to take into consideration this difference. Here I am dividing the correction in two parts: the offset and the variation. The offset is commonly represented by a constant three-dimensional vector fixed on the satellite body coordinate system, and thus the orientation of this vector depends on the satellite's orientation with respect to the earth. The variation part is an additional correction which depends on the nadir angle of the satellite-receiver vector. The offset and variation values can be retrieved from IGS antenna files (in ANTEX – ANTenna EXchange - format) which can be downloaded from the IGS web site, currently located at <ftp://igsb.jpl.nasa.gov/pub/station/general/> . The standard name of the file is `igsYY_WWWW.atx`, where *YY* represents the current IGS frame, and *WWW* represents the GPS week when the file in question was generated. The format, as well as the standards used in this file can be found in Rothacher and Schmid [2006], where one can find the definition on how the satellite antenna phase center correction has to be applied (as in the following two equations):

$$\underline{PCP} = \underline{CMP} + \underline{PCO}, \quad (2.53)$$

where: \underline{PCP} is the three-dimensional vector representing the satellite phase center position; \underline{CMP} is the three-dimensional vector representing the satellite center of mass position, and \underline{PCO} is the three-dimensional vector representing the satellite phase center offset.

$$R_{\text{corrected}} = R + \text{PCV} , \quad (2.54)$$

where R is the geometric distance, and PCV is the phase center variation.

As opposed to a formerly used standard (called “relative calibration”), when the satellite antenna offsets had fixed values for all satellites of a same satellite block, in the current standard (called “absolute calibration”) these values are actually determined for each particular spacecraft. As an observation, it should be noted that the spacecraft number “SVN” should not be confused with the pseudorandom noise “PRN” number. Different satellites can use the same PRN in different periods of time. Table 2.1 shows the GPS constellation history, since the launch of the first satellite until July of 2007 [U.S. Naval Observatory, 2007]. There are blanks for several satellites’ PRN because these satellites are no longer in operation and therefore do not have a PRN associated to them.

Because new satellites are launched and become part of the GPS constellation the file containing antenna information has to be constantly updated, (and that is also true for

LAUNCH	ORDER	PRN	SVN	LAUNCH	DATE	STD	PLANE	US SPACE	COMMAND **
*II-1			14	14	FEB 1989			19802	
*II-2			13		10 JUN 1989			20061	
*II-3			16		18 AUG 1989			20185	
*II-4			19		21 OCT 1989			20302	
*II-5			17		11 DEC 1989			20361	
*II-6			18		24 JAN 1990			20452	
*II-7			20		26 MAR 1990			20533	
*II-8			21		02 AUG 1990			20724	
*II-9			15		01 OCT 1990			20830	
IIA-10			32		26 NOV 1990	Rb	ES	20959	
IIA-11			24		04 JUL 1991	Cs	DS	21552	
IIA-12			25		23 FEB 1992	Rb	AS	21890	
*IIA-13			28		10 APR 1992			21930	
IIA-14			26		07 JUL 1992	Rb	FS	22014	
IIA-15			27		09 SEP 1992	Cs	A4	22108	
IIA-16		01	32		22 NOV 1992	Cs	F6	22231	
*IIA-17			29		18 DEC 1992			22275	
*IIA-18			22		03 FEB 1993			22446	
*IIA-19			31		30 MAR 1993			22581	
*IIA-20		07	37		13 MAY 1993		CS	22657	
IIA-21		09	39		26 JUN 1993	Cs	A1	22700	
IIA-22		05	35		30 AUG 1993	Rb	B5	22779	
IIA-23		04	34		26 OCT 1993	Rb	D4	22877	
IIA-24		06	36		10 MAR 1994	Rb	C1	23027	
IIA-25		03	33		28 MAR 1996	Cs	C2	23833	
IIA-26		10	40		16 JUL 1996	Rb	E3	23953	
IIA-27		30	30		12 SEP 1996	Cs	B2	24320	
IIA-28		08	38		06 NOV 1997	Cs	A3	25030	
**IIA-1			42		17 JAN 1997			24876	
IIA-2		13	43		23 JUL 1997	Rb	F3	25933	
IIA-3		11	46		07 OCT 1999	Rb	D2	26360	
IIA-4		20	51		11 MAY 2000	Rb	E1	26407	
IIA-5		28	44		16 JUL 2000	Rb	B3	26605	
IIA-6		14	41		10 NOV 2000	Rb	F1	26690	
IIA-7		18	54		30 JAN 2001	Rb	E4	27663	
IIA-8		16	56		29 JAN 2003	Rb	B1	27704	
IIA-9		21	45		31 MAR 2003	Rb	D3	28129	
IIA-10		22	47		21 DEC 2003	Rb	E2	28190	
IIA-11		19	59		20 MAR 2004	Rb	C3	28361	
IIA-12		23	60		23 JUN 2004	Rb	F4	28474	
IIA-13		02	61		06 NOV 2004	Rb	D1	28874	
IIA-14M		17	53		26 SEP 2005	Rb	C4	29486	
IIA-15M		31	52		25 SEP 2006	Rb	A2	29601	
IIA-16M		12	58		17 NOV 2006	Rb	B4	32260	
IIA-17M		15	55		17 OCT 2007	Rb	F2	32384	
IIA-18M		29	57		20 DEC 2007	Rb	C6		

Table 2.1. GPS satellite constellation history, as of July 2007.

GLONASS and Galileo satellites). In an ideal scenario, one should always check if there is any update of antenna file before processing GPS data in PPP mode.

As mentioned earlier, the satellite antenna offsets are represented as a three dimensional vector fixed to the satellite body coordinate system. The major component of this vector (component Z in the satellite's body coordinate system) is the component in the radial direction, i.e., which points to the earth's center of mass, and therefore the determination of this component's orientation is trivial. The orientation of the other two components depends on the position of the sun. The Y axis, which is the rotation axis of the solar panel, corresponds to the cross product of the Z axis with the vector from the satellite to the sun. The X axis completes the right-handed system [Rothacher and Schmid, 2006]. For illustration purposes, Figure 2.1 shows the antenna offsets for the GPS satellites, as of July 2007. There is no plot for the Y component because it has value equal to zero for all satellites.

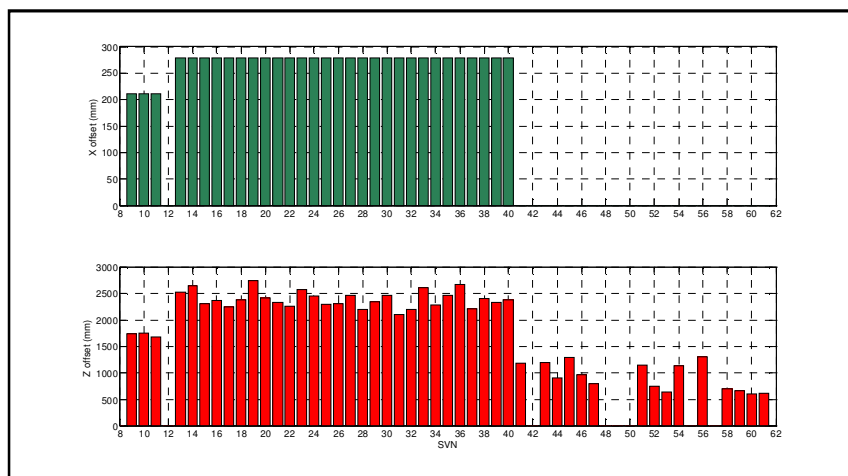


Figure 2.1. GPS satellite antenna offsets as of July of 2007 (Reference: International GNSS Service, file igs05_1421.atx). In this file there was no antenna information for SVN's 1, 2, 3, 4, 5, 6, 7, 8, 12, 42, 48, 49, 50, 55, and 57, for different reasons.

Concerning the phase center variation correction, the antenna file contains correction values distributed for several nadir angles. In order to determine the value to be used, one has to compute the nadir angle of the satellite-receiver vector at the time of the observation, and then interpolate (in this case, a linear interpolation is enough) the correction. It might be the case of having to extrapolate as well, depending on the nadir angles obtained for particular locations. The format of the file also comports variation for different azimuths, but, as of March 2008, the International GNSS Service has made available satellite APC corrections which depend on nadir angle only. Another interesting aspect is that the offsets and variations are made available with values for each frequency, even though in practice only the satellite APC iono-free combination has been determined. One should therefore have in mind that, as of March 2008, the values of the satellite APC offset and variation on L1 and L2 frequencies are simply a replication of the iono-free combination value. For detailed information on the format please refer to Rothacher and Schmid [2006]. Figure 2.2 shows the APC variations for all SVN's, as of July 2007.

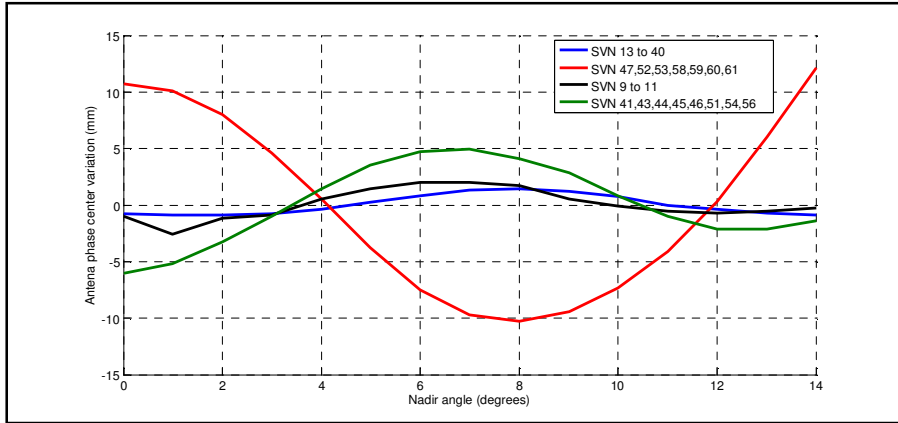


Figure 2.2. GPS satellite antenna phase center variation, as of July of 2007 (Reference: International GNSS Service, file igs05_1421.atx). Recently launched SVN's 55 and 57 have the same variation as 52, 53 and 58.

2.4.2. Receiver antenna phase center offset and variation

In this section I will discuss the correction due to the receiver antenna phase center offset and variation. Similar to the satellite APC information, the receiver-dependent offsets and variations can also be found in ANTEX files. The receiver APC offset correction also consists of a 3D offset vector, and variation corrections also have to be applied in the observation domain. They are given as:

$$\underline{PCP} = \underline{ARP} + \underline{PCO} , \quad (2.55)$$

where: \underline{PCP} is the three-dimensional vector representing the satellite phase center position; \underline{ARP} is the three-dimensional vector representing the receiver antenna reference point position, and \underline{PCO} is the three-dimensional vector representing the receiver phase center offset.

$$R_{\text{corrected}} = R + \text{PCV} , \quad (2.54)$$

where R is the geometric distance, and PCV is the phase center variation.

It is important to note that although the procedure is similar to the one used for satellites, receiver offsets are represented as 3D vector with components on North, East and Up direction in the receiver local geodetic coordinate system. Figure 2.3 shows a diagram of the UNBJ station antenna. In this example we can see that the antenna reference point of this antenna is about 30 cm above the station marker (which is actually the top of the pole to which UNBJ antenna is fixed). This offset is not part of the antenna phase center offset, and is usually referred to as “antenna height”. This value is particular for each antenna installation and it should be printed as one of the observation RINEX file header records (for instance “ANTENNA: DELTA H/E/N” record, which also supports North and East offsets – for more details about RINEX format one should refer to Gurtner and Estey [2006], or Gurtner and Estey [2007]). The receiver antenna phase center offset refers to the base of the antenna, the antenna reference point. In the case of the diagram below, the L1 and L2 APCs are 100.81 and 116.46 mm above the ARP, respectively. These values come from the absolute antenna APC calibration, which in this specific case was determined by Geo++ GmbH by means of a Robot calibration (more information concerning antenna calibration at Geo++ can be found at <http://gnpcvdb.geopp.de>).

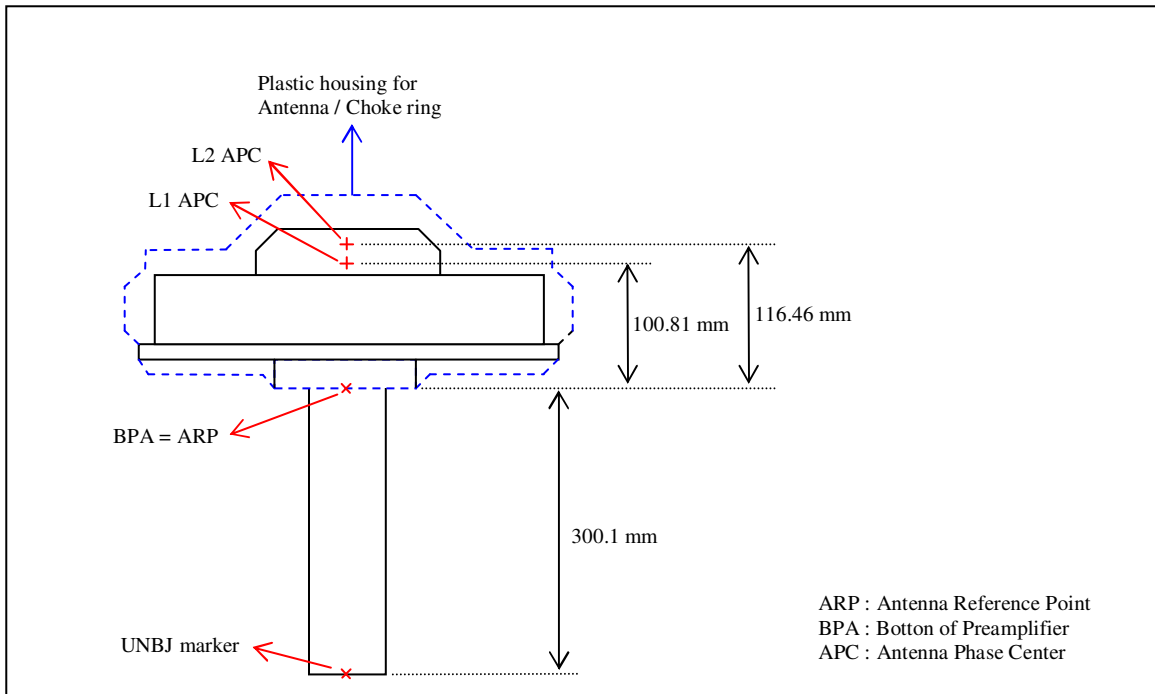


Figure 2.3. Diagram of UNBJ station antenna (RegAnt choke-ring antenna). Similar diagram can be obtained from UNBJ station log file, available at http://igsceb.jpl.nasa.gov/igsceb/station/log/unbj_20060906.log. The antenna offsets used here were obtained from ANTEX file igs05_1421.atx.

In Figure 2.4 one can see the L1 frequency receiver antenna phase center variation for UNBJ's antenna, with respect to zenith angle and azimuth, in mm. Figure 2.5 shows a similar plot, but for L2. These plots are also based on values obtained from IGS ANTEX file igs05_1421.atx. Figure 2.6 also shows the L1 and L2 antenna phase center variation, but with respect to zenith angle only. As it can be seen, the less variation is experienced at zenith direction, and maximum values of variation appear at lower elevation angles. We can also clearly see that the variation is stronger for L1 than for L2 frequency for this antenna. Mostly important, it is possible to notice that the APC variation values are at typically at sub-centimeter level for this antenna. This is also typically true for other antenna types (as can be noticed if one refers to the ANTEX file).

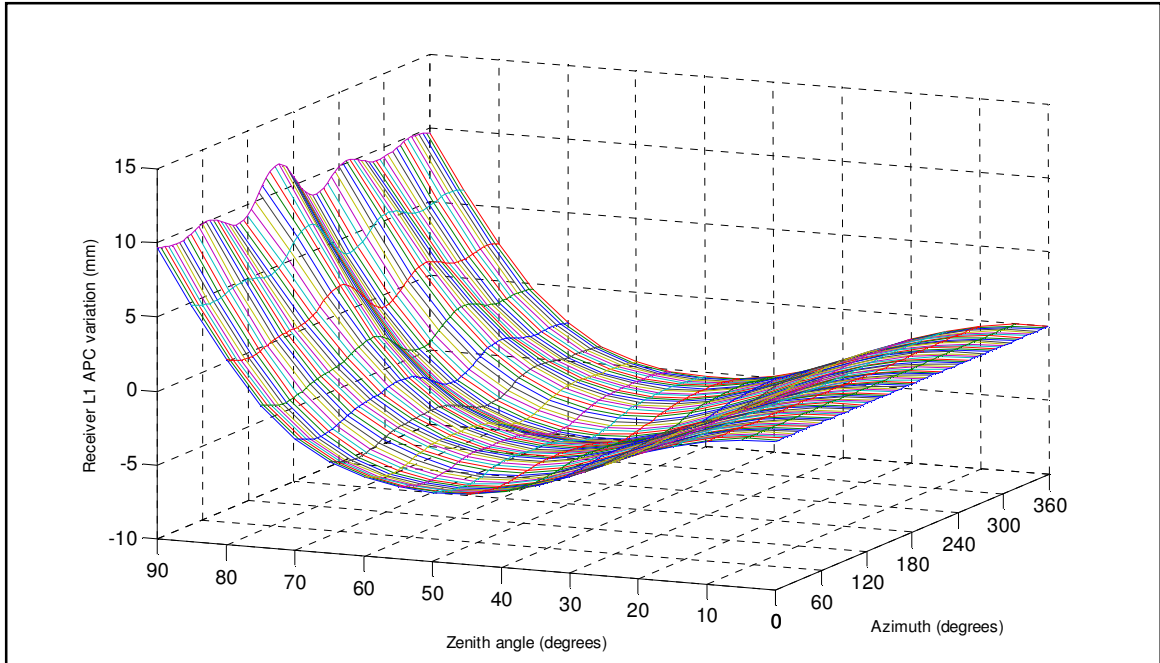


Figure 2.4. Antenna L1 phase center variation for station UNBJ's antenna, as of March 2008. Values obtained from file igs05_1421.atx.

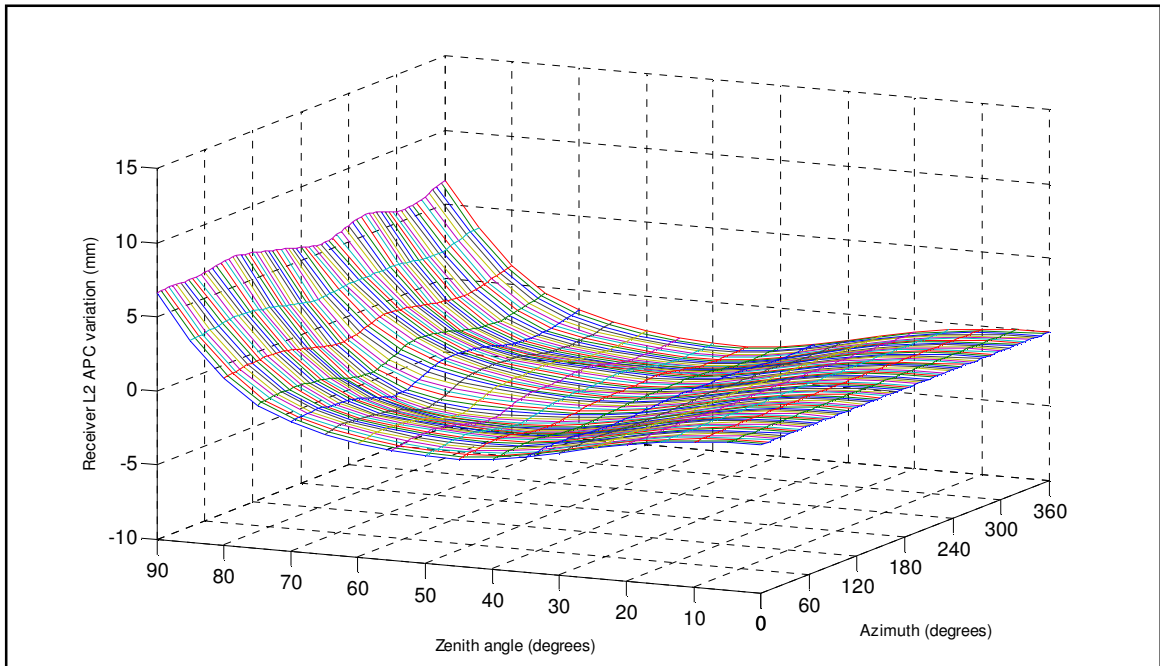


Figure 2.5. Antenna L2 phase center variation for station UNBJ's antenna, as of March 2008. Values obtained from file igs05_1421.atx.

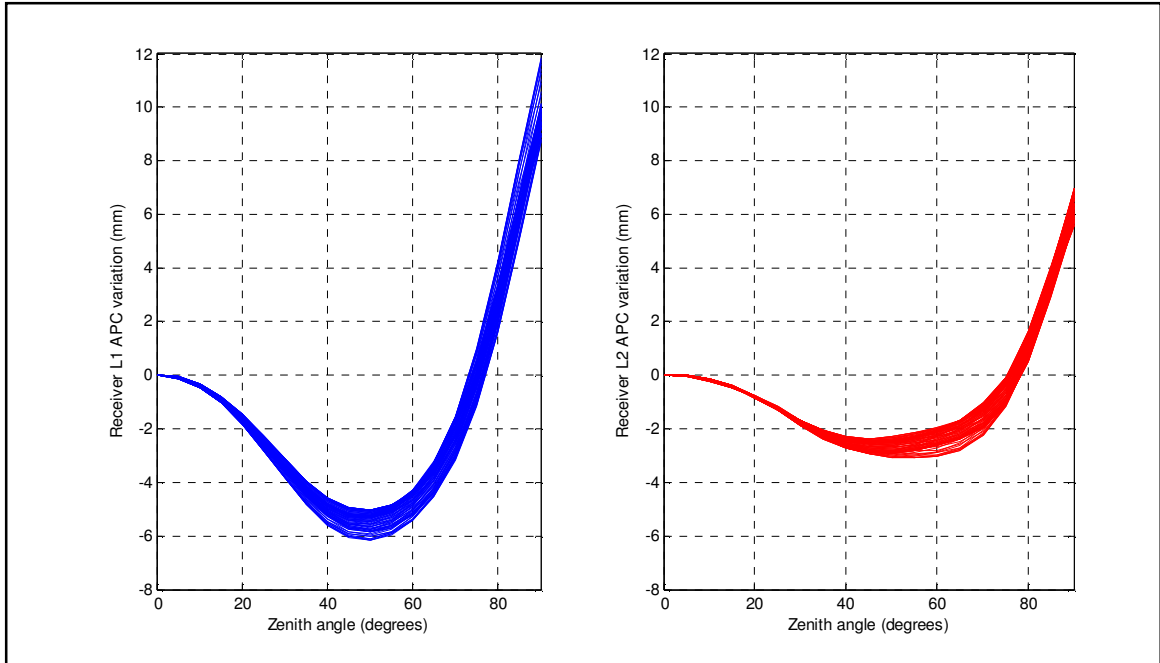


Figure 2.6. Antenna L1 and L2 phase center variation for station UNBJ's antenna, as of March 2008. Values obtained from file igs05_1421.atx.

2.4.3. Solid earth tide

In order to obtain coordinates accurate to cm level for a single receiver it is necessary to account for the site displacement due to the effects of solid earth tides. Since the earth is a body not totally rigid, its crust suffers the effect (i.e., deformation) of gravitational forces (mainly from sun and moon). These deformations, translated to displacements at individual points, can be modeled as being caused by tides of spherical harmonics [McCarthy and Petit, 2004]. The effect of solid earth tides can reach a few decimeters, and for details on how these effects should be computed one should refer to the latest version of the IERS (International Earth Rotation and Reference Systems Service) conventions. For instance (as of March 2008) one could refer to McCarthy and Petit

[2004]. Figure 2.7 shows the variation of UNBJ station site displacement due to solid earth tide over one day (5 March 2008).

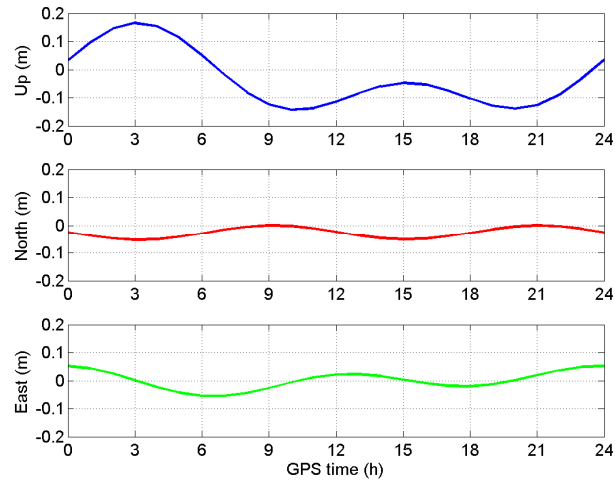


Figure 2.7. Variation of UNBJ station site displacement due to solid earth tide over one day (5 March 2008).

2.4.4. Ocean tide loading

Similarly to the “solid” earth, ocean water masses also suffer the effect of gravitational forces. These effects are widely known as the ocean tides.

Ocean tide loading (OTL) is the deformation of the earth due to the weight of the ocean tides. The water in the ocean tides moves back and forth and these mass redistributions cause periodic loading of the ocean bottom. Since the earth is not completely rigid, it deforms under this load. One can observe it as variations at your station in vertical and horizontal displacement, in gravity, tilt and in strain. The ocean tides are produced by the gravitational pull of the moon and sun and since their orbits have more than one periodicity due to the eccentricity, evection and the lot, the ocean tides can be described

as a sum of several ocean tides with each having their own period. The 11 periods, also called harmonics, with the largest amplitude are mostly used to compute the ocean tide loading [Ocean tide loading provider, 2008].

For the procedures related to the computation of ocean tide loading effects one should refer to McCarthy and Petit [2004]. The Ocean tide loading provider is an internet-based service which is maintained by Dr. Hans-Georg Scherneck at Onsala Space Observatory – Chalmers University of Technology, Sweden. This service is available at <http://www.oso.chalmers.se/~loading/> and it has been widely used by the GPS research community as means to obtain the necessary information for the computation of OTL displacements for particular stations, given by several models.

GAPS package currently does not apply corrections for OTL displacements. Other GPS packages such as GAMIT have implemented the necessary code to compute the tidal constituents for a given site from a particular model (such as GOT00.2), as well as the displacements themselves [King, 2007].

2.4.5. Differential code biases

Also known as differential hardware delays, the differential biases have to be applied in the observations in order to account for different delays experienced by the GPS signal depending on what frequency (combination) is used. Even though carrier-phase measurements also suffer such kind of effect, it gets absorbed by the PPP float ambiguity

parameter, as mentioned earlier in this chapter. In case one is attempting to fix ambiguities in PPP, the effect on phase should also be considered. Since the code measurements, as used today, do not have an ambiguity parameter to be estimated, it is essential that the biases for code observations are taken care of, in order to reach ultimate accuracies. More details about biases will be discussed in chapter 4.

2.4.6. Phase wind-up effect

The observed carrier-phase measurement depends on the orientation of the antennas of both receiver and satellite, thus it is necessary to account for the phase shift caused by this “mis-orientation”. These phase shift values change over time as the satellite moves (and therefore changes its orientation with respect to the receiver). It also depends on the receiver antenna attitude, so, in order to fully account for that effect, it is necessary to always know the orientation of the receiver antenna, which is sometimes not an easy task. The most known description on how to account for that effect can be found in Wu et al. [1992], and one could refer to this reference in order to obtain details on the procedure. The necessary elements for accounting for the phase wind-up effect are the receiver coordinate system unit vectors, and the same for the satellite. In GAPS package it is assumed that the receiver’s orientation with respect to north direction does not change. This is a reasonable assumption as far it goes to static positioning, since the receiver should ideally be oriented like that. This assumption becomes much weaker when it comes to kinematic positioning, since it is not possible (or perhaps not even reasonable) to guarantee that orientation.

3. Ionospheric delay estimation filter

3.1. Introduction

Ionosphere delay is closely related to GPS measurements because it is one of the main effects which have to be mitigated in order to determine reliable positions. Since the ionosphere is a dispersive medium, which means the value of the delay depends on the frequency of the signal, and GPS signals are broadcast on more than one frequency, using receivers capable of tracking GPS signals on two or more frequencies allows us to mathematically eliminate the first order effect of the ionosphere refraction. This is possible by means of a combination of the signals at different frequencies. This combination is widely called the iono-free combination, and it can be performed as described in the previous chapter. If on one hand the ionosphere impacts GPS signals, on other hand GPS can be used as a sensor of the ionosphere. In this chapter I am introducing an approach to using GPS as a sensor of the ionosphere. GPS receiver networks have been used for this purpose for a long time, but this new method was created to be suitable for single receiver operation. This means that this approach allows the estimated ionospheric delay to be one of the outputs of a PPP package, and in this case it is done in GAPS. Another characteristic is that only carrier-phase measurements are used, in order to avoid effects present on pseudorange measurements, as it will be explained later in this chapter. The filter to estimate the ionospheric delays is connected to the PPP filter inside GAPS. All those aspects will be discussed through this chapter.

3.2. Ionospheric delay estimation filter

In this section I will explain how the filter works, showing also another observation model which is widely used in ionospheric delay modeling, in order to justify why a novel model was necessary and to show their respective advantages and drawbacks. Let the carrier-phase observation equations be as follows:

$$\Phi_1 = R + c(dT - dt) + T - I + \lambda_1 N_1 + hd_{r,1} - hd_{s,1} + pb_{r,1} - pb_{s,1} + m_1 + e_1, \quad (3.1)$$

and

$$\Phi_2 = R + c(dT - dt) + T - \gamma I + \lambda_2 N_2 + hd_{r,2} - hd_{s,2} + pb_{r,2} - pb_{s,2} + m_2 + e_2, \quad (3.2)$$

where: Φ_1 and Φ_2 are carrier-phase measurements on the L1 and L2 frequencies, respectively, in meters; R is the geometric distance between satellite and receiver antennas, in meters; c is the speed of light, in meters per second; dT and dt are clock errors of receiver and satellite, respectively, in seconds; T is the neutral atmosphere delay, in meters; I is the ionosphere delay, in meters, for the L1 frequency; γ is the factor to convert the ionospheric delay from L1 to L2 frequency, unitless; λ_1 and λ_2 are carrier-phase wavelengths for the L1 and L2 frequencies, respectively, in meters; N_1 and N_2 are carrier-phase integer ambiguities on the L1 and L2 frequencies, respectively, in

cycles; $hd_{r,i}$ and $hd_{s,i}$ are receiver and satellite carrier-phase hardware delays, respectively, in meters, where i represents the frequency number (1 or 2); $pb_{r,i}$ and $pb_{s,i}$ are receiver and satellite carrier-phase initial phase bias, respectively, in meters, where i represents the frequency number (1 or 2); m_1 and m_2 are carrier-phase multipath on the L1 and L2 frequencies, respectively, in meters; and e_1 and e_2 are other un-modeled errors of carrier-phase measurements on the L1 and L2 frequencies, respectively, in meters.

The factor γ comes from the fact the ionospheric delay is inversely proportional to the squared frequency of the signal:

$$I_i = \frac{40.3 \text{ TEC}}{f_i^2}, \quad (3.3)$$

where f_i is the frequency of the signal, and TEC is the total electron content, in 10^{16} electrons per meter squared. Using equation 3.3 it is possible to establish a relation between delays in frequencies L1 and L2:

$$I_2 = \frac{40.3 \text{ TEC}}{f_2^2} = \frac{f_1^2}{f_2^2} I_1 = \gamma I_1, \quad (3.4)$$

thus:

$$\gamma = \frac{f_1^2}{f_2^2}. \quad (3.5)$$

Similar equations to 3.1 and 3.2 can be used for pseudorange, as follows:

$$P_1 = R + c(dt - dT) + T + I + HD_{r,1} - HD_{s,1} + M_1 + E_1, \quad (3.6)$$

and

$$P_2 = R + c(dt - dT) + T + \gamma I + HD_{r,2} - HD_{s,2} + M_2 + E_2, \quad (3.7)$$

where: P_1 and P_2 are pseudorange measurements on the L1 and L2 frequencies, respectively, in meters; $HD_{r,i}$ and $HD_{s,i}$ are receiver and satellite pseudorange hardware delays, respectively, in meters, where i represents the frequency number (1 or 2); M_1 and M_2 are pseudorange multipath on the L1 and L2 frequencies, respectively, in meters; and E_1 and E_2 are other un-modeled errors of the pseudorange measurements on L1 and L2 frequencies, respectively, in meters.

In order to eliminate geometric effects we can perform the so called geometry-free combination, which consists of a difference between the observations of the two frequencies, in length units. Let the geometry-free carrier-phase and pseudorange observation equations be, respectively:

$$\Phi_{\text{gf}} = \Phi_2 - \Phi_1, \quad (3.8)$$

and

$$P_{\text{gf}} = P_2 - P_1, \quad (3.9)$$

where Φ_{gf} and P_{gf} are the geometry-free carrier-phase and pseudorange combinations, respectively. Using equations 3.1 and 3.2 in 3.8, and 3.6 and 3.7 in 3.9 yields:

$$\begin{aligned} \Phi_{\text{gf}} = & (1 - \gamma)I + \lambda_2 N_2 - \lambda_1 N_1 + (\text{hd}_{r,2} - \text{hd}_{r,1}) - (\text{hd}_{s,2} - \text{hd}_{s,1}) \\ & + (\text{pb}_{r,2} - \text{pb}_{r,1}) - (\text{pb}_{s,2} - \text{pb}_{s,1}) + (m_2 - m_1) + (e_2 - e_1), \end{aligned} \quad (3.10)$$

and

$$P_{\text{gf}} = (\gamma - 1)I + (\text{HD}_{r,2} - \text{HD}_{r,1}) - (\text{HD}_{s,2} - \text{HD}_{s,1}) + (M_2 - M_1) + (E_2 - E_1). \quad (3.11)$$

In the two equations above, the terms $(\text{hd}_{r,2} - \text{hd}_{r,1})$, $(\text{hd}_{s,2} - \text{hd}_{s,1})$, $(\text{HD}_{r,2} - \text{HD}_{r,1})$ and $(\text{HD}_{s,2} - \text{HD}_{s,1})$ are receiver and satellite differential hardware delays for carrier-phase and pseudorange, respectively. The terms referred to pseudorange are often called differential code biases (DCB). In order to maintain consistency, I will call terms related to carrier phase as differential phase biases (dpb) in this thesis. Another term pertinent to carrier

phase is the initial phase bias (pb). Although in theory it could be possible to separate these two terms by using data from long periods of time, in practice it would be a very difficult task to be accomplished. This is because initial phase and hardware phase delays are very correlated with each other, and thus it is nearly impossible to mathematically separate them as parameters in a carrier-phase equation, since their partial derivatives (-1 and 1) are related by a single multiplication constant, making any normal matrix singular, and thus not permitting an adjustment of them as separate parameters for a single receiver, even though they are two distinct effects with different causes. Because of this, I will include the initial phase bias as part of the differential phase bias (dpb) parameter. Similar behavior is intrinsic to L1 and L2 ambiguities, which will also be reduced to a single parameter. Therefore equations 3.10 and 3.11 can be rewritten as:

$$\Phi_{gf} = (1 - \gamma)I + N'_{gf} + dpb_r - dpb_s + m_{gf} + e_{gf} , \quad (3.12)$$

and

$$P_{gf} = (\gamma - 1)I + DCB_r - DCB_s + M_{gf} + E_{gf} , \quad (3.13)$$

where: N'_{gf} is the carrier-phase geometry-free ambiguity, in meters (a prime symbol is used because the ambiguity is being represented in meters rather than in cycles); dpb_r and dpb_s are receiver and satellite differential phase biases, respectively, in meters; DCB_r and DCB_s are receiver and satellite differential code biases, respectively, in meters; m_{gf} and

M_{gf} are carrier-phase and code geometry-free multipath, respectively, in meters; and e_{gf} and E_{gf} are carrier-phase and code geometry-free un-modeled errors, respectively, in meters.

Assuming multipath is an effect which will not be modeled in this approach, parameters which have to be determined are the ionospheric delay, differential biases, and ambiguities (in case of carrier phase). Even though there is one additional parameter to be solved for carrier phase, the ambiguity, it is an observation with a noise level several order of magnitudes smaller than the pseudorange, which is an un-ambiguous observation. One very common way to take advantage of the low noise characteristic of the carrier phase, and the un-ambiguous nature of the pseudorange is using the phase-leveling technique. This technique has been used by Komjathy [1997]. It consists of basically removing the ambiguity parameter from the carrier-phase equation, using pseudorange. In order to achieve better results in this process, this pseudorange-based ambiguity term is computed using a certain number of observations, which might correspond to a satellite arc in which there is no cycle slip. The observation equation of the ambiguity parameter in the phase-leveling technique ($N'_{gf,pl}$) can be used as follows:

$$N'_{gf,pl} = P_{gf} + \Phi_{gf}, \quad (3.14)$$

and therefore:

$$\bar{N}'_{gf,pl} = N'_{gf} + DCB_r - DCB_s + \bar{M}_{gf} + \bar{E}_{gf} + dpb_r - dpb_s + \bar{m}_{gf} + \bar{e}_{gf} . \quad (3.15)$$

It is important to notice that the multipath terms are now mean values, because equation 3.15 is evaluated using several observations over time, which eliminates higher frequency components of multipath terms, keeping the mean value of the multipath over the observation arc. The same occurs for other errors. The ambiguity term can then be removed from the carrier phase equation, according to:

$$\Phi_{gf,pl} = \Phi_{gf} - \bar{N}'_{gf,pl} , \quad (3.16)$$

yielding:

$$\Phi_{gf,pl} = (1 - \gamma)I - DCB_r + DCB_s + (m_{gf} - \bar{m}_{gf}) + (e_{gf} - \bar{e}_{gf}) - \bar{M}_{gf} - \bar{E}_{gf} , \quad (3.17)$$

where $\Phi_{gf,pl}$ is the leveled carrier-phase. As seen in equation 3.17, the ambiguity parameter is gone now. It also applies to differential phase biases and all mean values of effects pertinent to carrier-phase observations (i.e. multipath and other errors). The variation of multipath and other errors in carrier phase over time (terms inside parentheses) are still present in the leveled-phase equation. Even though there is an attenuation of the carrier-phase multipath effect in the leveled phase, a mean pseudorange multipath and average of other pseudorange errors are added to the observation (the last two terms of the equation above). Therefore there is an exchange between phase mean

multipath by the pseudorange mean multipath over the arc, which can be several orders of magnitude higher than the same effect on carrier phase. The effect of the multipath on pseudorange is further explored in the next chapter.

Because receiver differential code biases are common for all satellites being observed simultaneously, and satellite differential code biases are common for all receivers observing a particular satellite, these parameters can be solved for as a by-product of the ionospheric delay estimation, using a network of GPS receivers. Another advantage of using a network of receivers is that the mean pseudorange multipath from several receivers tends to average out when used to estimate one or more common parameters, since multipath for different receivers is uncorrelated. The effect of using several receivers to reduce the impact of multipath is also discussed in chapters 5 and 6. Another interesting aspect is that satellite differential code biases are very useful for single frequency users. This is because satellite clocks are usually determined using a combination of measurements on two frequencies, and offsets should be applied to these clock values to make them useful for receivers with one frequency only. More details about biases and satellite clocks are discussed in chapters 5 and 6.

The observation model of equation 3.17 is not adequate for single receiver data processing for several reasons. In a single receiver scenario, there are several satellites, and thus several satellite differential code bias parameters, and only one receiver, which makes it impossible to determine values for each of those terms. The impact of the mean pseudorange multipath will be higher than in a network approach, because there will not

be other receivers' data to be used to minimize the effect with an averaged uncorrelated multipath. This means that the use of pseudorange brings practically no benefit in a single receiver scenario. Rather than using phase leveling, the single receiver approach which is being presented here makes use of carrier phase observables only. Looking back to equation 3.12, it is possible to notice that for a single receiver, satellite and receiver differential phase biases are highly correlated with the ambiguity parameter. As discussed earlier, this means that these parameters cannot be separately estimated in this case. However, since the goal of the approach is to obtain the ionospheric delays and not the biases, the latter ones can be grouped with the ambiguity parameter to be estimated as a single value, according to:

$$\Phi_{gf} = (1 - \gamma)I + Nb'_{gf} + m_{gf} + e_{gf} , \quad (3.18)$$

where

$$Nb'_{gf} = N'_{gf} + dpb_r - dpb_s . \quad (3.19)$$

Again, assuming carrier-phase multipath as an un-modeled effect in this model, there are two parameters to be estimated: the ionospheric delay and the ambiguity parameter. In order to achieve a solution for that, more than one observation must be used, and, more than that, the system of equations is solvable only if the equations refer to the same ionospheric delay parameter, otherwise there would be one delay parameter for each

observation, plus the ambiguity parameter, which would make the number of unknowns larger than the number of observations. This problem can be solved by establishing a relationship between delays observed by different satellites, at different epochs, with different ionospheric piercing points. A first step is accounting for the slant delay, since the delay experienced by each observation depends on the amount of ionosphere the signal has to go through. This can be done by means of a mapping function, according to:

$$I = MF \cdot I_v, \quad (3.20)$$

where I_v is the vertical ionospheric delay, and MF is the mapping function. The mapping function which is used in this approach considers a spherical shell model for the ionosphere, and can be computed according to:

$$MF = \frac{1}{\sin(\beta)} = \frac{1}{\sqrt{1 - \left(\frac{r \cdot \cos(e)}{r + sh} \right)^2}}, \quad (3.21)$$

where β is the complement of the angle of incidence of the satellite (S) to observer (O) geometric line at the ionospheric shell (I), r is the mean radius of the Earth, sh is the ionospheric shell height and e is the geometric satellite elevation angle with respect to the observer. Figure 3.1 illustrates all necessary elements for the computation of this mapping function, which can be evaluated using the sine's law, according to:

$$\cos(\beta) = \sin(90 - \beta) = \frac{r \cdot \sin(e + 90)}{r + sh} = \frac{r \cdot \cos(e)}{r + sh}. \quad (3.22)$$

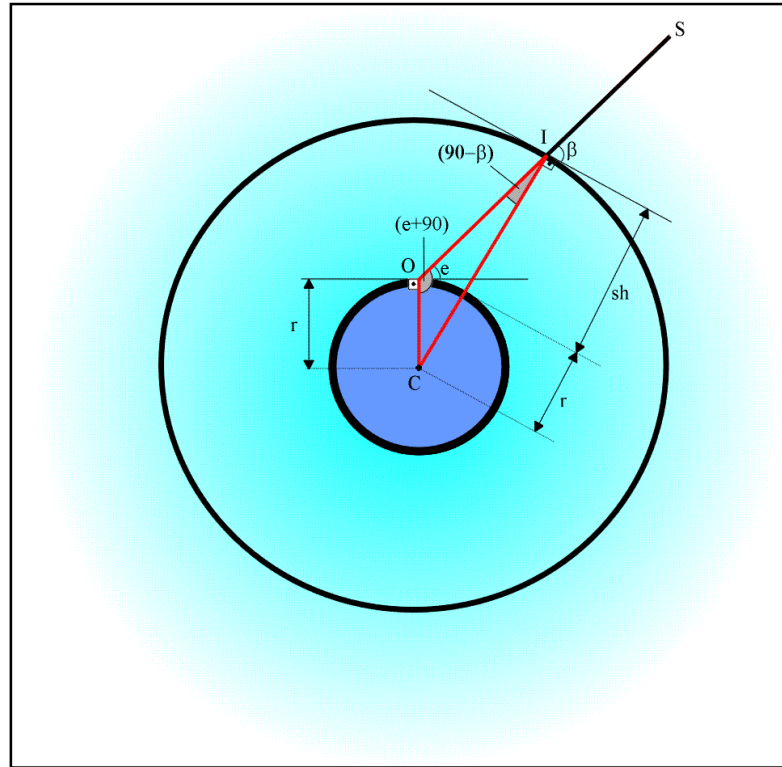


Figure 3.1. Elements of the spherical ionospheric shell model.

Similar ionospheric mapping function models have been used for example in CDGPS (Canada Differential GPS) system [Lahaye, 2006].

Another aspect which should be taken into account is that the position of the piercing point (represented by I in Figure 3.1) is different for each satellite, and different for the same satellite observed at different epochs. If the signals are piercing the ionosphere at different points, they are experiencing delays which are different, due to the variation of the ionosphere behavior at different regions at the same time. In order to account for that,

a bilinear model is used. This model is similar to models used in Komjathy [1997] and Kolb et al. [2005], and can be represented as follows:

$$I_{v,p} = I_{v,0} + \nabla_{\phi} (\phi_{g,p} - \phi_{g,0}) + \nabla_{\lambda} (\lambda_{g,p} - \lambda_{g,0}), \quad (3.23)$$

where:

$I_{v,p}$ and $I_{v,0}$ are the ionospheric vertical delays at the piercing point and the station location, respectively, in meters; ∇_{ϕ} and ∇_{λ} are the latitudinal and longitudinal vertical ionospheric delay gradients, respectively, in meters per degree; $\phi_{g,p}$ and $\phi_{g,0}$ are the geographic latitude of the piercing point and the station, respectively, in degrees; and $\lambda_{g,p}$ and $\lambda_{g,0}$ are the geographic longitude of the piercing point and the station, respectively, in degrees.

If equations 3.23 and 3.20 are introduced into equation 3.18, the following is obtained:

$$\Phi_{gf} = (1 - \gamma)MF(I_{v,0} + \nabla_{\phi} (\phi_{g,p} - \phi_{g,0}) + \nabla_{\lambda} (\lambda_{g,p} - \lambda_{g,0})) + Nb'_{gf} + m_{gf} + e_{gf}, \quad (3.24)$$

and ignoring the non-modeled effects of the model:

$$\Phi_{gf} = (1 - \gamma)MF(I_{v,0} + \nabla_{\phi} (\phi_{g,p} - \phi_{g,0}) + \nabla_{\lambda} (\lambda_{g,p} - \lambda_{g,0})) + Nb'_{gf}. \quad (3.25)$$

The equation above shows the observation model used in the ionospheric delay estimation filter, where three parameters of a spherical ionospheric shell model ($I_{v,0}$, ∇_ϕ , and ∇_λ) are estimated at each epoch together with ambiguity parameters (Nb'_{gr}). The shell model parameters are the same for all satellites, while there is an individual ambiguity term for each satellite. The adjustment is performed by means of a least-squares filter, similar to the one used for coordinate determination (shown in previous chapter), thus:

$$\underline{\delta} = (\underline{A}'\underline{P}\underline{A} + \underline{C}_x^{-1})^{-1} \underline{A}'\underline{P}\underline{w}, \quad (3.26)$$

where $\underline{\delta}$ is the update vector, \underline{A} is the design matrix, \underline{P} is the weight matrix, \underline{C}_x is the parameter covariance matrix, and \underline{w} is the misclosure vector.

The update vector is computed every epoch, and the parameters get updated as:

$$\underline{x} = \underline{x}_0 + \underline{\delta}, \quad (3.27)$$

where \underline{x} is the updated parameters vector, and \underline{x}_0 is the previously updated parameters vector. The parameters covariance matrix also gets updated, according to:

$$\underline{C}_x = (\underline{A}'\underline{P}\underline{A} + \underline{C}_{x,0}^{-1})^{-1}, \quad (3.28)$$

where $\underline{C}_{x,0}$ is the previously updated parameter covariance matrix. The weight matrix is built using an elevation angle dependent model, as follows:

$$\sigma_i^2 = \frac{\sigma_0^2}{\sin(e_i)}, \quad (3.29)$$

where σ_i^2 is the variance of the observation i , e_i is the correspondent elevation angle, and σ_0^2 is the geometry-free carrier-phase a-priori variance. The model also accounts for the variation of the parameters over time, by considering some of them as stochastic parameters. After the covariance matrix of the parameters is updated according to equation 3.28 and before it is used again as in equation 3.26, it receives a process noise contribution, according to:

$$\underline{C}_x = \underline{C}_x' + \underline{C}_n, \quad (3.30)$$

where \underline{C}_x' is the parameters covariance matrix before the update, \underline{C}_x is the same after the update, and \underline{C}_n is the process noise covariance matrix (where “n” stands for noise), where:

$$\underline{C}_n = \begin{bmatrix} \sigma_I^2 & 0 & 0 & 0 & \dots & 0 \\ 0 & \sigma_{\nabla_\phi}^2 & 0 & 0 & \dots & 0 \\ 0 & 0 & \sigma_{\nabla_\lambda}^2 & 0 & \dots & 0 \\ 0 & 0 & 0 & 0 & \dots & 0 \\ \vdots & \vdots & \vdots & \vdots & \ddots & \vdots \\ 0 & 0 & 0 & 0 & \dots & 0 \end{bmatrix}, \quad (3.31)$$

where σ_I^2 , $\sigma_{\nabla_\phi}^2$, and $\sigma_{\nabla_\lambda}^2$ are the process noise variances for parameters $I_{v,0}$, ∇_ϕ , and ∇_λ , respectively. The process noise matrix is filled with zeros for elements with any index greater than 3 because those elements refer to the ambiguity parameters, and those are considered to be constant over time. There are only two cases when the diagonal elements related to ambiguities are different from zero: at the very first epoch of a satellite observation arc, when there is no a-priori knowledge about the ambiguity parameter value; and when the ambiguity parameter has to be initialized. There are two main reasons why these parameters might have to be initialized: if a cycle slip in at least one of the frequencies is detected; or if the observation fails in the quality control which is based on residuals control of the position estimation. These two controls are effected inside the PPP filter, which means that when an observation arrives at the ionospheric delay estimation filter, it has been validated by the positioning filter. Figure 3.2 shows the scheme of this relationship.

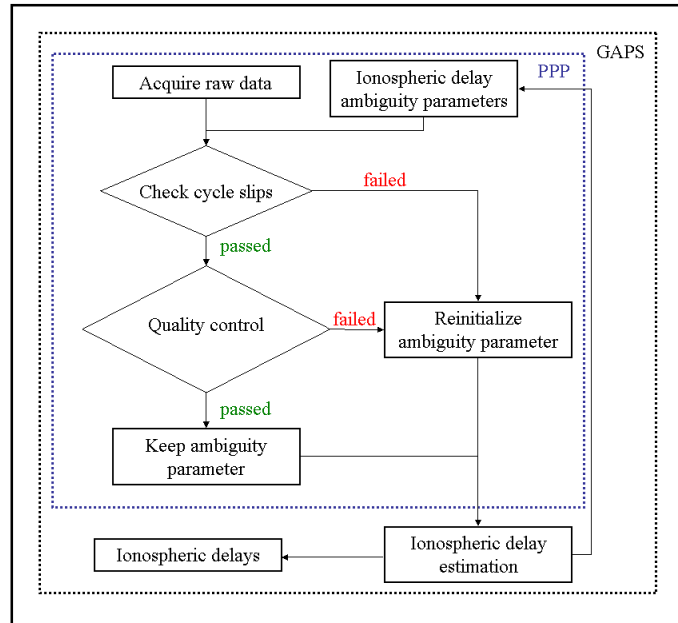


Figure 3.2. Relationship between positioning and ionospheric delay filters in GAPS.

The “PPP” box represents the positioning filter. Even though the ionospheric delay ambiguity parameters are sent back to the positioning filter (so it can reinitialize them if necessary), they are not used in any way for positioning. The ionosphere delay filter depends on the PPP filter, but the opposite is not true.

3.3. Results analysis

In order to illustrate the type of results which will be analyzed in this chapter, Figure 3.3 shows an example of ionospheric delays converted to TEC units computed using GAPS. The data is from IGS (International GNSS Service) station UNBJ, observed on January 1st 2007.

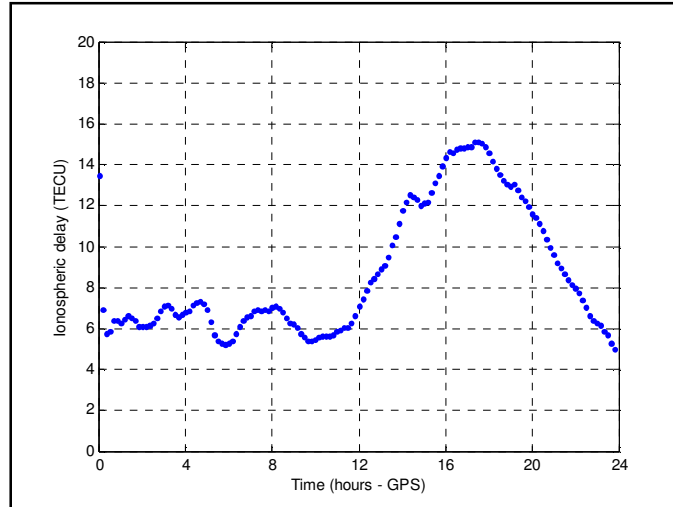


Figure 3.3. Vertical ionospheric delays computed with GAPS for station UNBJ, data observed at January 1st 2007.

TECU stands for total electron content units, and it can be related to delays in length units for the different frequencies by means of equation 3.3. Evaluating 3.3 for frequencies of L1 and L2, 1 TECU represents approximately 0.1624 m and 0.2674 m of delay on L1 and L2, respectively. According to Klobuchar [1996], the ionospheric delays get to their maximum values at around 14 h local time. Station UNBJ is at approximately -67 degrees longitude, which means maximum delays are expected to occur between 18 h and 19 h GPS Time. In figure 3.3, it can be seen that the maximum delay value indeed occurs in this interval.

In this chapter the performance of the ionospheric delay estimation filter is assessed in several ways, as listed below:

- Analysis of adjustment residuals;

- Comparison of results for nearby stations;
- Comparison of results with other solutions.

Each of the items above will be explored in the next sections of the chapter. Six GPS monitoring stations were chosen to be used. The choice was made trying to have a reasonable distribution in geodetic latitude. The stations used are:

- UNB1/UNBJ – Fredericton, New Brunswick, Canada ($45^{\circ} 57' N$);
- FRDN – Fredericton, New Brunswick, Canada ($45^{\circ} 56' N$);
- BRAN – Burbank, California, USA ($34^{\circ} 10' N$);
- LEEP – Hollywood, California, USA ($34^{\circ} 08' N$);
- MANA – Managua, Nicaragua ($12^{\circ} 09' N$);
- RIOG – Rio Grande, Tierra del Fuego, Argentina ($53^{\circ} 47' S$);

Figure 3.4 shows the stations listed above. As can be noticed, there are two pairs of stations which are close to each other (UNBJ/FRDN, and BRAN/LEEP). These pairs were chosen to be used for nearby stations results analyses, as will be discussed later.

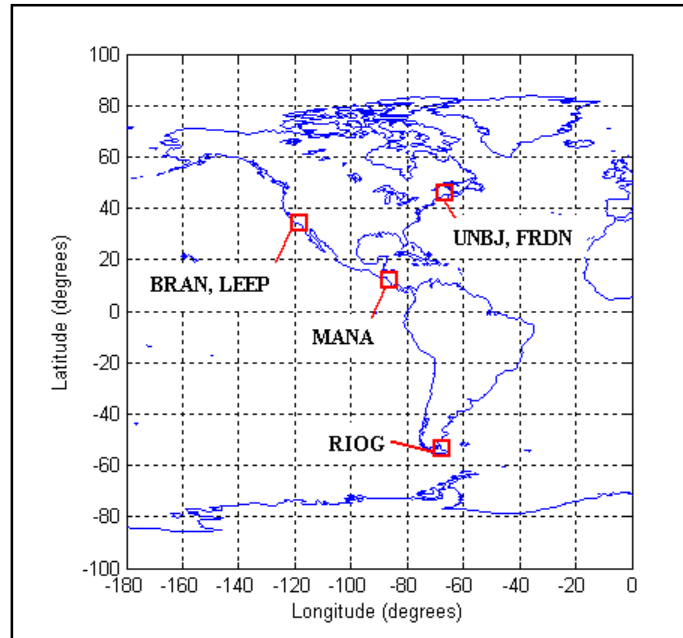


Figure 3.4. Stations used in the ionospheric delay filter analysis.

In order to assess the performance of the filter under different ionospheric disturbance conditions, two sets of five consecutive days were chosen for the analysis. One of the sets was chosen in a period with high activity, while the other is a quiet period. The choice was based on planetary K (K_p) index values, which were obtained from the Space Environment Center, National Oceanic and Atmospheric Administration (NOAA), US Dept. of Commerce, Boulder, CO [Space Environment Center, 2007]. The K_p indexes are a measure of the earth's geomagnetic field activity, and have values which can range from 0 to 9. The two 5-day periods were chosen in order to have values close to 9 and 0, as high activity and quiet day periods, respectively. The 5-day period for high activity is 7 November 2004 to 11 November 2004 (DOY 312 to 316). This period has been studied as a high ionospheric activity example by other authors, such as Maruyama [2006]. Figure 3.5 shows the K_p index values for this period. As can be seen, K_p index values

reach the value 9 on some occasions during these days, with overall high values over the time period.

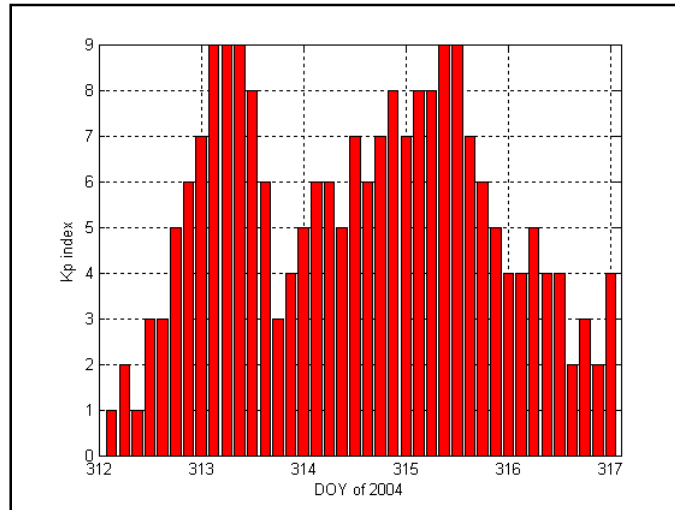


Figure 3.5. Kp index values for days of year 312 to 316 of 2004.

Figure 3.6 shows Kp index values for the time period considered as quiet. As can be noticed, values range from 0 to a maximum of 3, over the whole period.

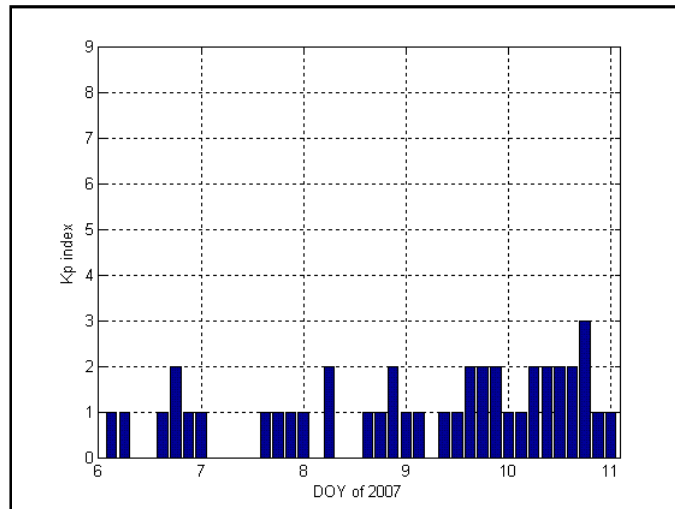


Figure 3.6. Kp index values for days of year 006 to 010 of 2007.

The next four sections (3.2.1, 3.2.2, 3.2.3, and 3.2.4) discuss the results obtained with the dataset which was just described.

3.3.1. Analysis of adjustment residuals

In this section, the residuals of the ionospheric delay filter adjustment are analyzed. The residuals of the adjustment are important because they can provide useful information concerning the capability of the model of describing the observations, as well as the effects suffered by them. One of these effects is fundamental in this specific case, which is the ionospheric refraction. As described in the beginning of the chapter, in this approach the ionospheric delays are modeled by means of a bilinear model which describes the behavior of vertical delays over the station region (as can be seen in equations 3.24 and 3.25). The residuals can be computed as follows:

$$r_s = \Phi_{gf} - \left((1 - \gamma)MF(I_{v,0} + \nabla_{\phi}(\phi_{g,p} - \phi_{g,0}) + \nabla_{\lambda}(\lambda_{g,p} - \lambda_{g,0})) + Nb'_{gf} \right), \quad (3.32)$$

where r_s is the slant residual (the terminology “slant” will be discussed later).

Considering equation 3.24 it is possible to see that the residuals will represent a measure of the non-modeled parameters, which means:

$$r_s = m_{gf} + e_{gf}. \quad (3.33)$$

Therefore the residual values have a straight relation with multipath and other errors, such as receiver noise, and also modeling errors. One of these sources of errors is of particular interest in this case, which is the model non-capability of fully describing the ionosphere behavior, or, in other words, the fact that in real life the ionosphere can not be perfectly modeled with a bilinear model. Based on this, the spread of the residuals can be used as a measure of how far, or close, the model is from describing the reality. Another interesting analysis which can be made with the residuals is based on the assumption that the model does describe reality, which means the residuals are dominated basically by observation noise, and in this case, they should have a Gaussian-like distribution. In order to perform these analyzes the slant residuals are computed according to equation 3.32. These residuals are being called “slant” because they refer to the observations in their observed direction, even though the ionospheric delay model describes the ionosphere by means of vertical delays. Another residual measure which will be used here, to be called vertical residuals, is computed according to:

$$r_v = \frac{\Phi_{gf}}{MF} - \left((1 - \gamma)(I_{v,0} + \nabla_{\phi}(\phi_{g,p} - \phi_{g,0}) + \nabla_{\lambda}(\lambda_{g,p} - \lambda_{g,0})) + \frac{Nb'_{gf}}{MF} \right), \quad (3.34)$$

or

$$r_v = \frac{r_s}{MF}, \quad (3.35)$$

where r_v is the vertical residual. These two types of residuals refer to slightly different things, but still very correlated: the slant residuals represent the capability of the model to describe the slant ionospheric delays suffered by GPS signals, while the vertical residuals represent the capability of the model to describe the ionosphere in terms of vertical delays. The difference comes from the fact that a unique vertical delay error will produce different errors in slant directions, depending on their inclination, and this relation is accounted for with the mapping function.

The results will be shown in a station-wise sequence, with two sets (for low and high activity periods) of figures for each station, showing the ionospheric delay values, slant residuals, and vertical residuals, and one table summarizing the statistics of the results.

Figures 3.7 and 3.8 show the results for station UNB1/UNBJ.

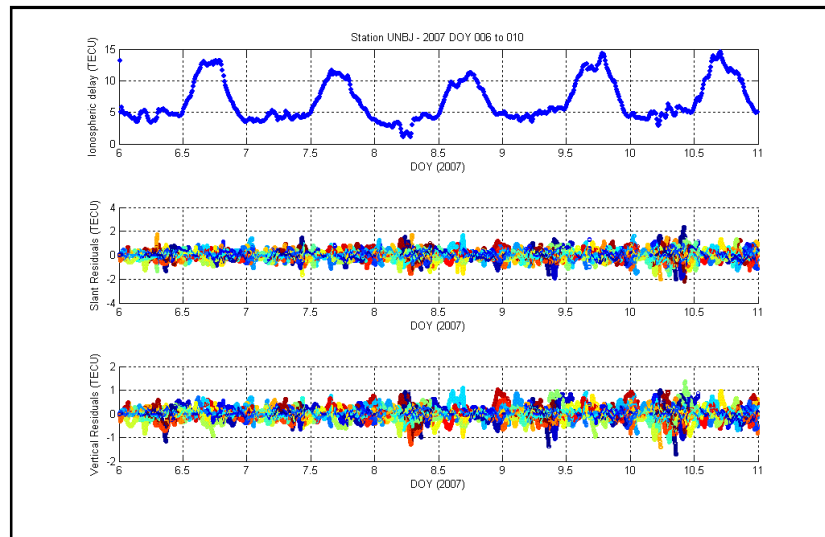


Figure 3.7. Ionospheric delays and residuals for station UNBJ, 2007 DOY 6 to 10.

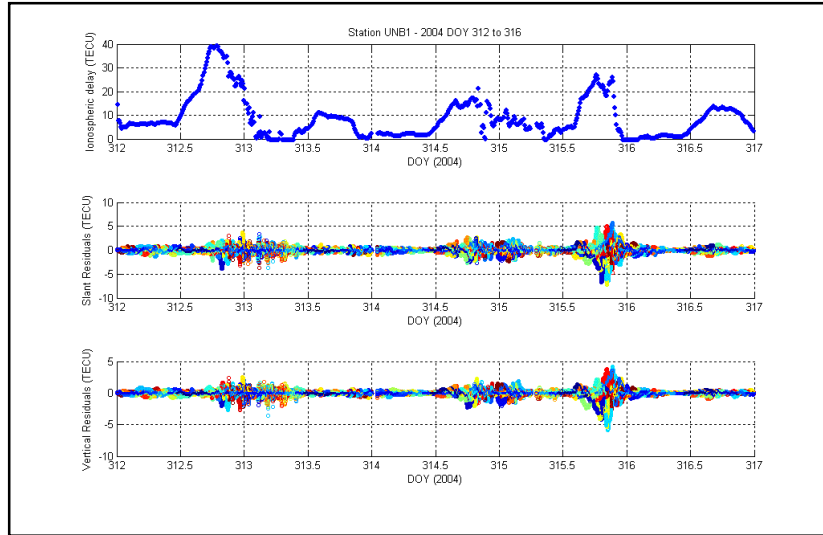


Figure 3.8. Ionospheric delays and residuals for station UNB1, 2004 DOY 312 to 316.

During the quiet period the residuals for UNBJ had values usually within 2 and 1 TECU for slant and vertical values, respectively, while for the disturbed period the amplitude of the residuals reached around 5 TECU at certain hours. It can also be seen that the spread of the residuals is reasonably stable over the days of the quiet period, which does not occur during the disturbed period, where variations in residual spread can be easily seen. In the second plot the station name is UNB1 because the observations were made prior the station name change (from UNB1 to UNBJ) which occurred in 2006 [Langley, 2006]. Figures 3.9 and 3.10 show the results for station FRDN.

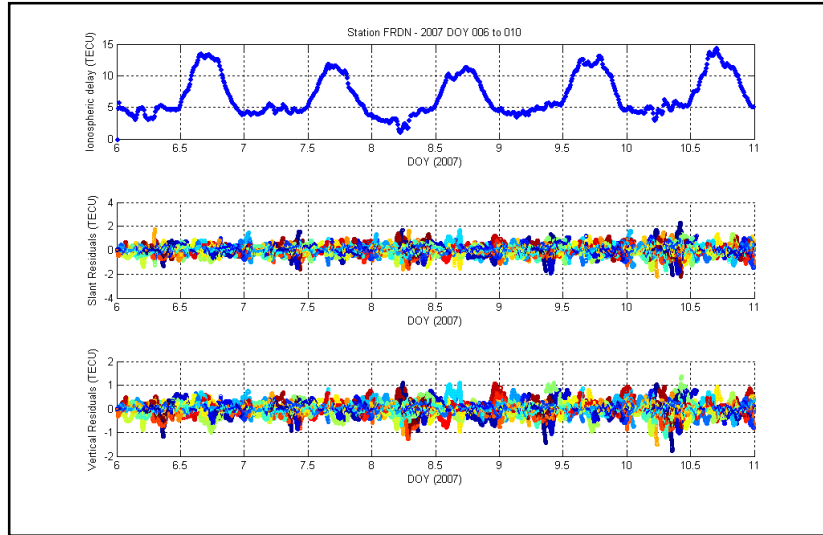


Figure 3.9. Ionospheric delays and residuals for station FRDN, 2007 DOY 6 to 10.

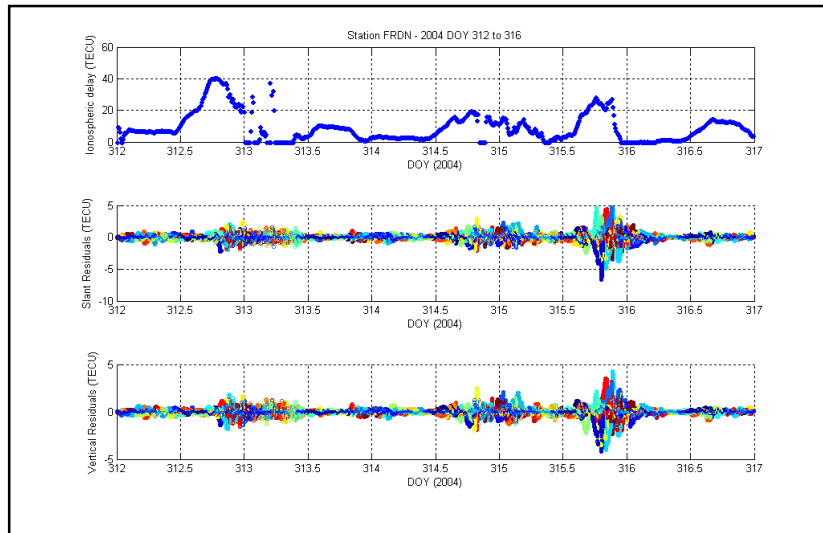


Figure 3.10. Ionospheric delays and residuals for station FRDN, 2004 DOY 312 to 316.

Results for FRDN are very similar to the ones obtained for UNBJ. That can be easily explained by the proximity of the two stations. A comparison of results between these two stations will be discussed in next section. Figures 3.11 and 3.12 show the results for station BRAN.

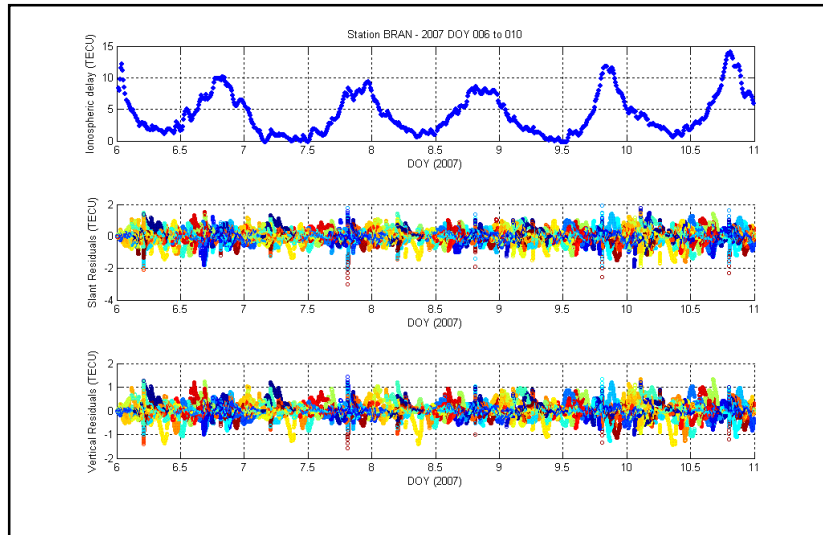


Figure 3.11. Ionospheric delays and residuals for station BRAN, 2007 DOY 6 to 10.

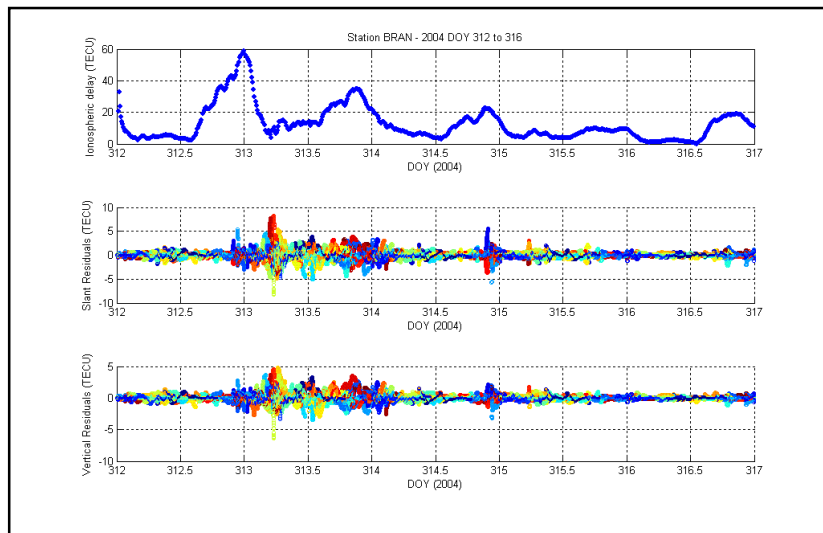


Figure 3.12. Ionospheric delays and residuals for station BRAN, 2004 DOY 312 to 316.

The residuals behavior for station BRAN is similar to UNB1/UNBJ and FRDN. One interesting feature is that the larger residuals spread doesn't necessarily occur at the exact times of maximum ionospheric delays, as can be seen in Figure 3.12 for example. This is because larger residuals will be experienced when the behavior of the ionosphere doesn't match with the model, and this behavior mis-modeling might occur at times which are

not the exact maximum delay times. One possible reason for the mis-modelling is the fact that a reasonably simple model (i.e. a bilinear model) is used to represent a large area of the atmosphere. Figures 3.13 and 3.14 show the results for station LEEP.

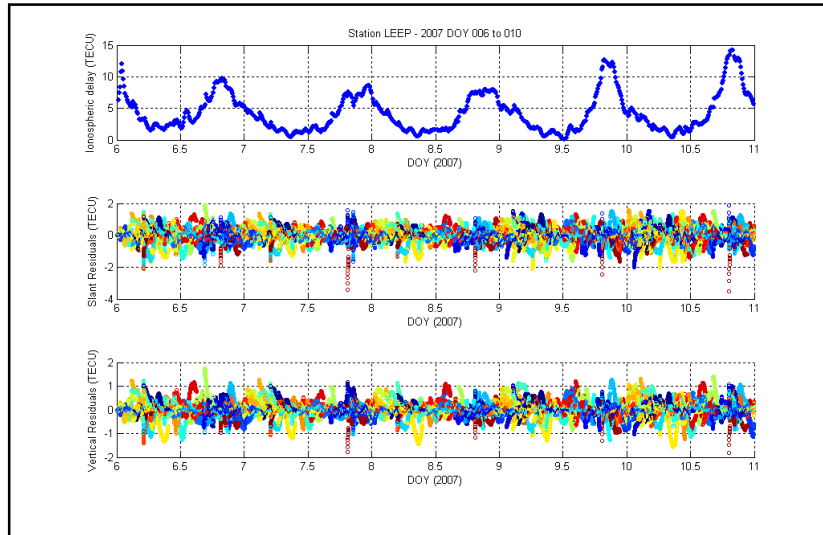


Figure 3.13. Ionospheric delays and residuals for station LEEP, 2007 DOY 6 to 10.

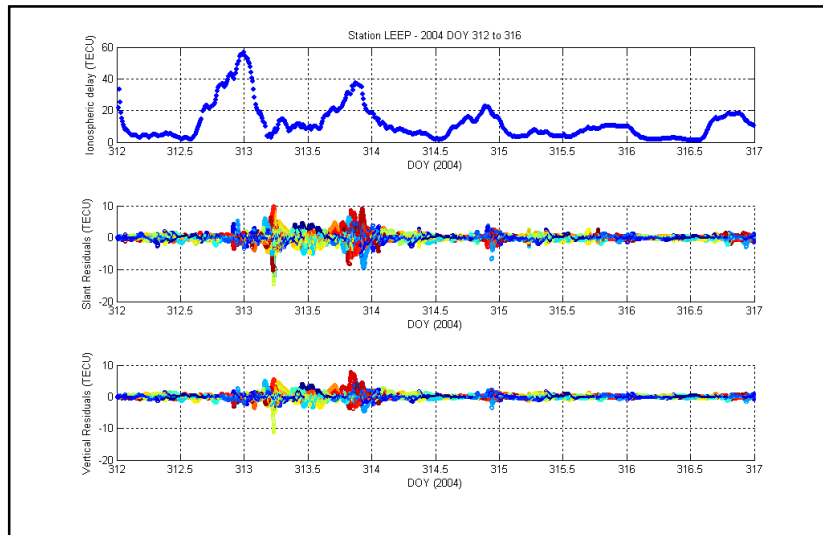


Figure 3.14. Ionospheric delays and residuals for station LEEP, 2004 DOY 312 to 316.

Station LEEP is located near station BRAN, both of them in California, USA, so in the same way as UNB1/UNBJ and FRDN, LEEP and BRAN have results which are similar. The similarity of ionospheric delay values comes from the fact that the vertical TEC is being computed for nearly the same position, thus, the same results should ideally be obtained. The similarity of residuals comes also from the fact that the two receivers observe the same constellation of satellites. Figures 3.15 and 3.16 show the results for station MANA.

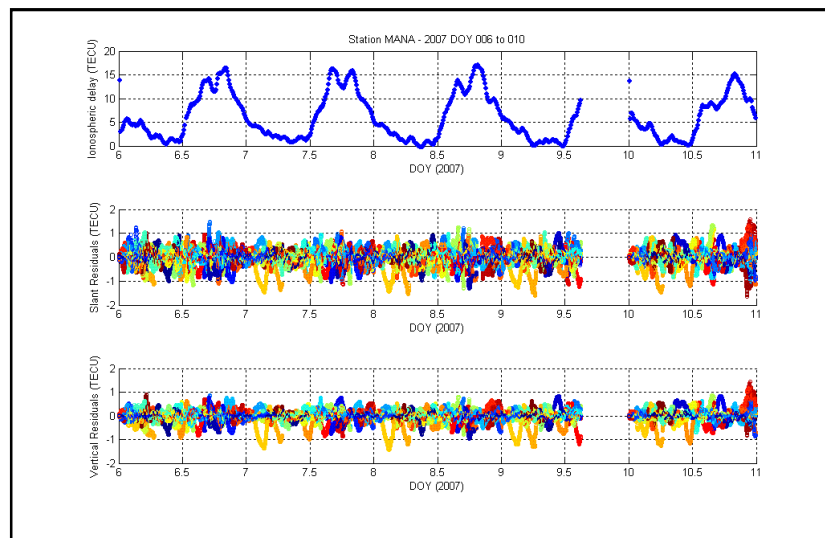


Figure 3.15. Ionospheric delays and residuals for station MANA, 2007 DOY 6 to 10.

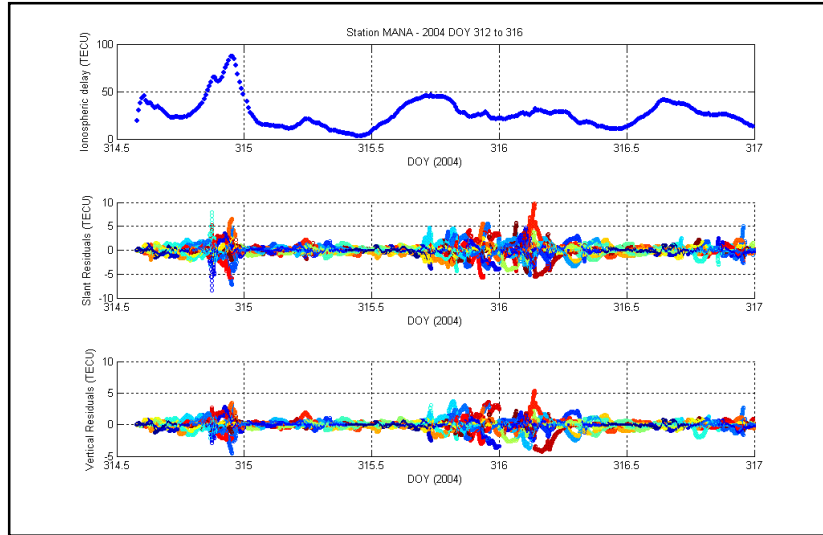


Figure 3.16. Ionospheric delays and residuals for station MANA, 2004 DOY 312 to 316.

On 9 January 2007 station MANA didn't have observations for the last hours of the day, which caused the gap which can be seen in Figure 3.15. During the storm period, data of this station was available only from part of DOY 314 onwards, as it can be seen in Figure 3.16. MANA is the nearest station to the equator which was used, and during the storm period TEC values of more than 80 TECU (at the end of DOY 314) were observed. Figures 3.17 and 3.18 show the results for station RIOG.

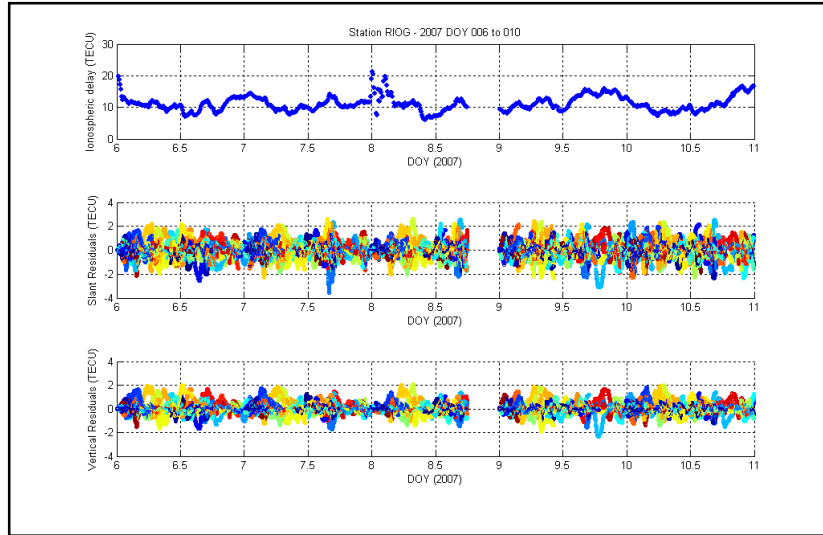


Figure 3.17. Ionospheric delays and residuals for station RIOG, 2007 DOY 6 to 10.

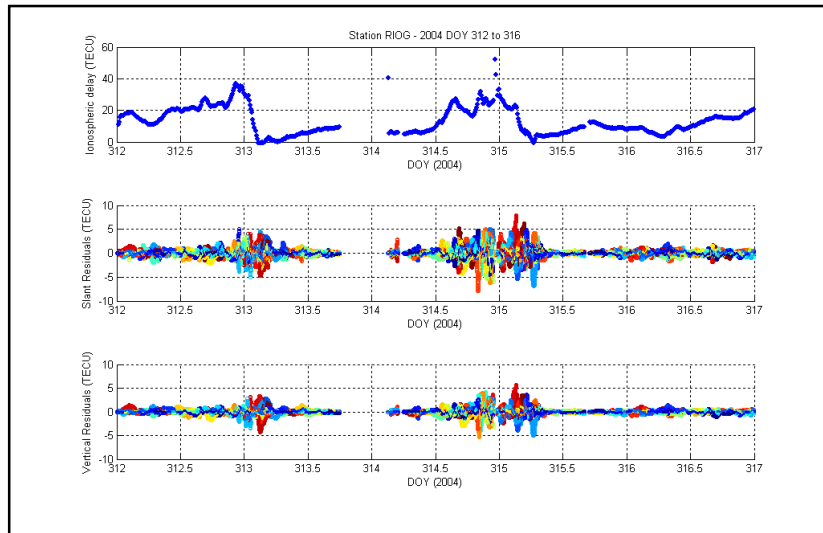


Figure 3.18. Ionospheric delays and residuals for station RIOG, 2004 DOY 312 to 316.

Like stations MANA, station RIOG had periods of time with no data available. The visible outliers in the results (upper plots of each figure) were caused by re-initialization of the filter.

3.3.2. Comparison of results for nearby stations

In this section, results obtained for stations which are located near each other are compared. It is easy to see in Figure 3.4 that stations that can be used for that are BRAN and LEEP; and UNB1/UNBJ and FRDN. It is worth mentioning that the data processing for each of the stations is performed in a totally independent way from the other (stations). On the other hand one should consider that nearby stations are affected by the same effects related to satellite geometry. Figures 3.19 and 3.20 show the comparison for stations BRAN and LEEP, for the quiet and disturbed period, respectively.

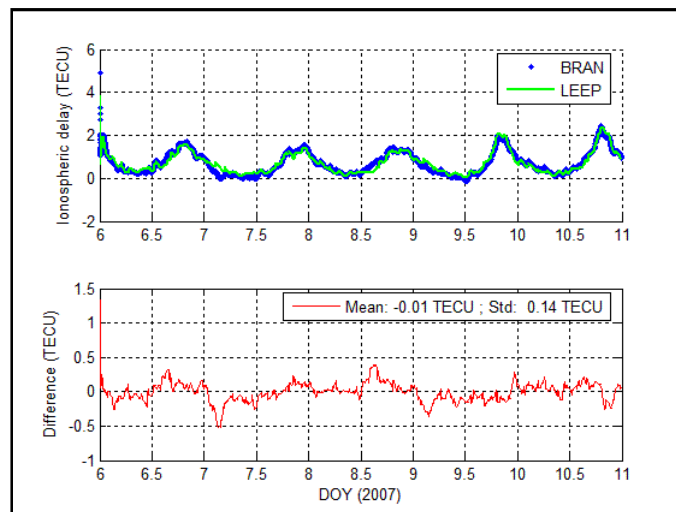


Figure 3.19. Comparison of results for stations BRAN and LEEP, 2007 DOY 6 to 10.

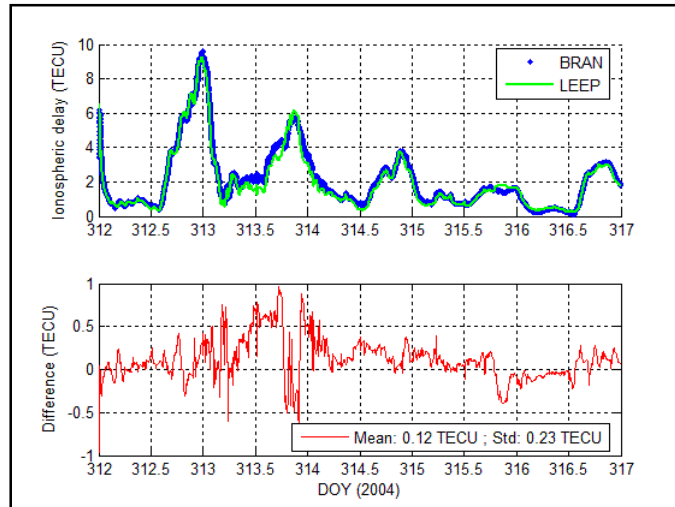


Figure 3.20. Comparison of results for stations BRAN and LEEP, 2004 DOY 312 to 316.

From the plots above one can notice that there is a reasonable overall agreement between the solutions for the two different stations. The differences for the quiet period are an approximately zero-mean series, with standard deviation of 0.14 TECU. During the disturbed period, the zero-mean property of the differences is lost somewhat, with a bias of 0.12 TECU. One possible reason for this bias might be that it is more difficult to estimate the absolute (unbiased) ionosphere during storm periods, which depends on correctly determining the biased ambiguity parameters. The spread of the differences is also worse for the disturbed period, with standard deviation of 0.23 TECU, i.e., nearly one and a half times the corresponding value for the quiet period. It is also noticeable that major differences occur on DOY 313, when the Kp index reached a value of 9 for several hours. Figures 3.21 and 3.22 show the comparisons for stations UNB1/UNBJ and FRDN, for the quiet and disturbed period, respectively.

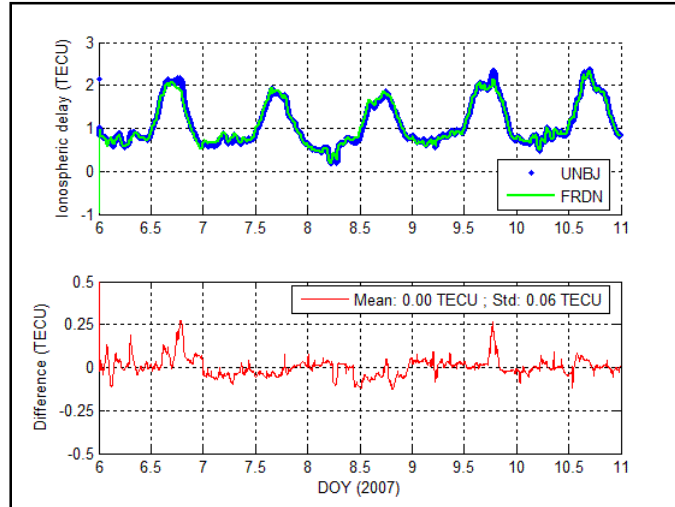


Figure 3.21. Comparison of results for stations UNBJ and FRDN, 2007 DOY 6 to 10.

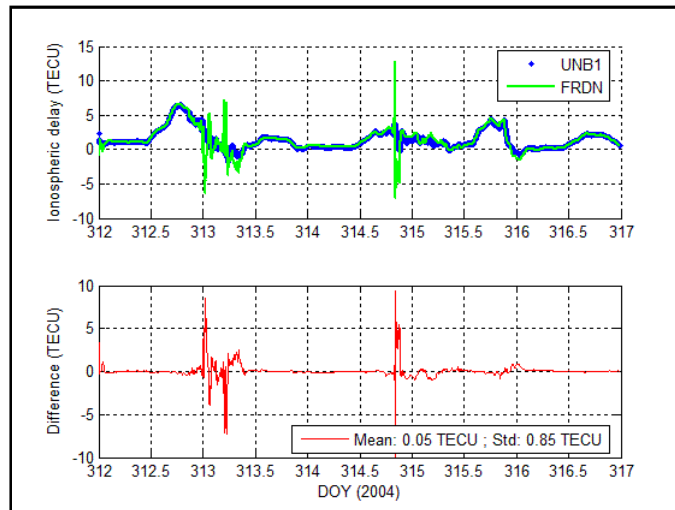


Figure 3.22. Comparison of results for stations UNB1 and FRED, 2004 DOY 312 to 316.

The results for these two stations are quite similar during the quiet period, with a bias approximately equal to zero, and a standard deviation of about 0.06 TECU. These results can be considered to be on the same order of magnitude as for the BRAN and LEEP comparison during the quiet day. During the storm period, it is clear that there are two periods in which there is a disturbance in FRDN values. These periods match with periods in which the Kp index reached high values during that week. These disturbances

have been caused by problems with the data itself (e.g. cycle slips) during that period. Similar effects can be experienced, not only for ionospheric delay, but also other parameters, in cases in which there are several losses of lock of many satellites during the same period. Regardless, for these two disturbance periods, the agreement between the two series is reasonably good, however the overall statistics get impacted by those effects, and a standard deviation as high as 0.85 TECU was obtained.

One should have in mind that the most important aspect of this comparison is checking if the values determined for the “ambiguity plus biases” parameters are converging to the correct values, since a bias in those parameters will result in a bias in the ionospheric delay itself. Considering that different receivers are used at those stations (as can be seen in Table 3.1), the receiver bias part of the ambiguity parameter is different for each station, as well as the ambiguity itself.

Table 3.1. Receiver types of the stations used in this analysis (according to their respective site logs – accessed on September 2007).

Station	Receiver type
UNB1/UNBJ	Javad TPS LEGACY
FRDN	AOA BENCHMARK ACT
BRAN	Ashtech Z-XII3
LEEP	Ashtech Z-XII3
MANA	Trimble 4000SSI
RIOG	Ashtech Z-XII3

When processing different stations under the same portion of the ionosphere, the agreement of the results is extremely dependent on the correct computation of the ambiguity parameter (which, again, includes carrier phase ambiguities and biases). The

computation of inter-frequency biases (they are called “inter-frequency” because they refer to a differential delay of observations on the L1 and L2 frequencies) has been the object of many research studies. As an example, Komjathy et al. (2005) have found that the consistency of receiver biases they could find with their technique is generally better than 1 TECU for mid-latitude sites, and better than 2 TECU for equatorial sites.

According to Komjathy (2007), the technique employed to obtain those results is still in use at JPL (Jet Propulsion Laboratory). If we look at the results obtained in this analysis, we will find an overall ionospheric delay agreement of better than 1 TECU for the nearby stations. More than that, this agreement was shown to be better than 0.2 TECU during quiet periods.

3.3.3. Comparison of results with other solutions

In this section I will show a comparison between the ionospheric delay estimations obtained with GAPS and other solutions. The solutions chosen for this comparison are the ones provided by IGS (International GNSS Service), by means of publicly available files in IONEX format (details about IONEX format can be found in Schaer et al. (1998)). Global TEC grid maps are one of the product types made available by IGS. IGS claims an accuracy of 2-8 TECU for final, and 2-9 TECU for its rapid TEC maps (International GNSS Service (2007)). It is important to have in mind that numbers provided by this comparison are not a direct measure of quality, since it is impossible to tell which solution is providing the biggest share of error; they are simply a direct measure of agreement between the two solutions. It is also worth mentioning that the goals of these two techniques are different, where one aims at having a good global

ionosphere map (IGS map), while the other (GAPS) is designed to provide the best measure of the ionosphere condition at a certain location and time. In practice, it means that one should consider that while an ionospheric delay is being determined for each particular station position at every epoch with GAPS, this same delay is being interpolated in space and in time from a grid to provide IGS' estimate for the same quantity, a procedure which always provides estimates which are smoothed in space and time. Details on procedures to use IGS ionospheric maps can be found in Schaer et al. [1998].

The next plots (Figures 3.23 to 3.28) show the results obtained with GAPS (blue dots) in comparison with values obtained from the IGS map (red lines) for the respective day and location.

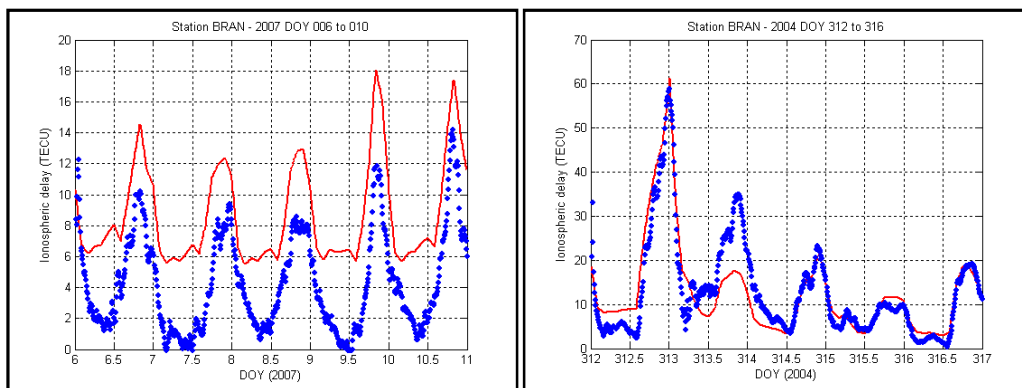


Figure 3.23. Comparison of results provided by GAPS (blue dots) and IGS (red line) for station BRAN.

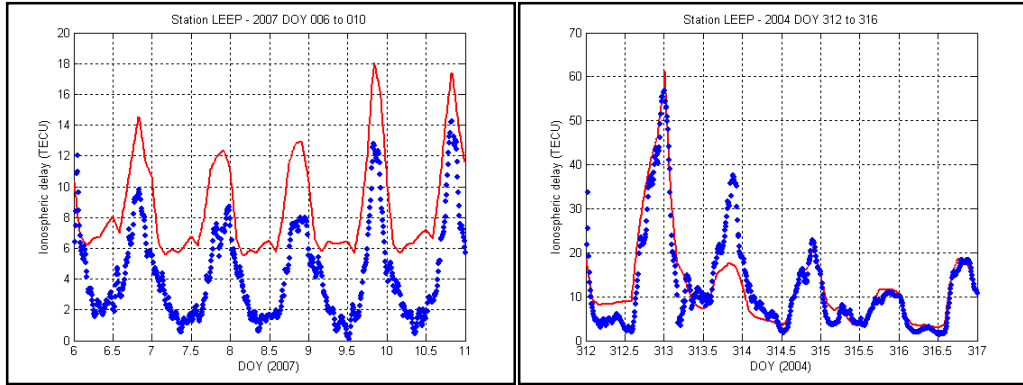


Figure 3.24. Comparison of results provided by GAPS (blue dots) and IGS (red line) for station LEEP.

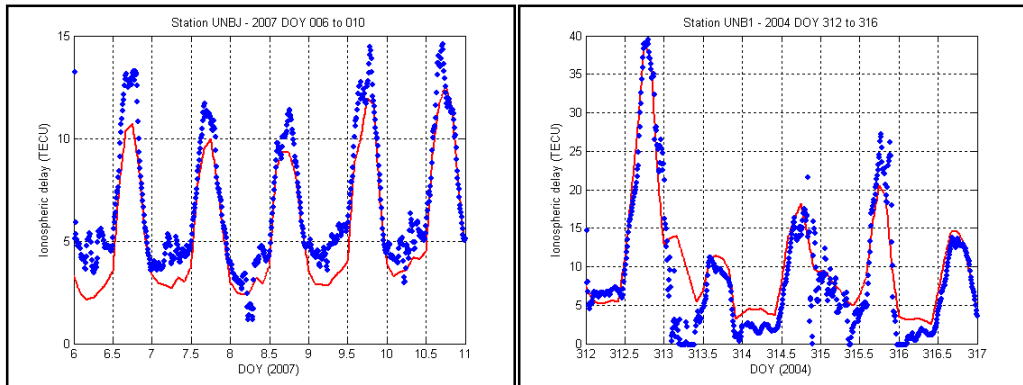


Figure 3.25. Comparison of results provided by GAPS (blue dots) and IGS (red line) for station UNBJ/UNB1.

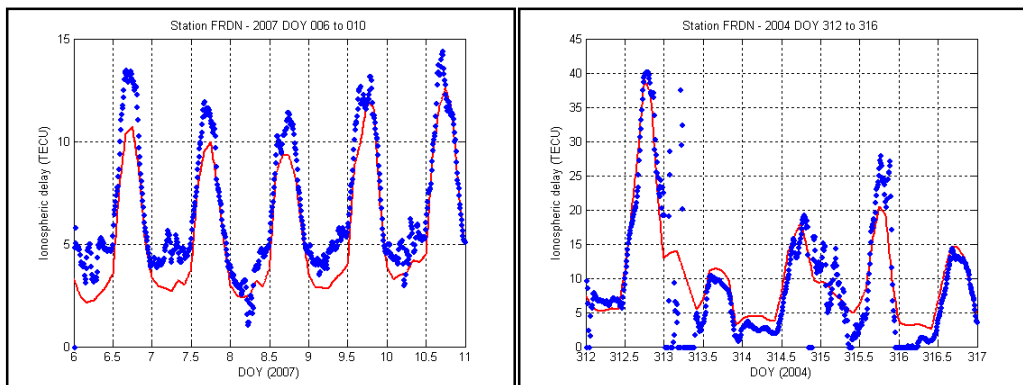


Figure 3.26. Comparison of results provided by GAPS (blue dots) and IGS (red line) for station FRDN.

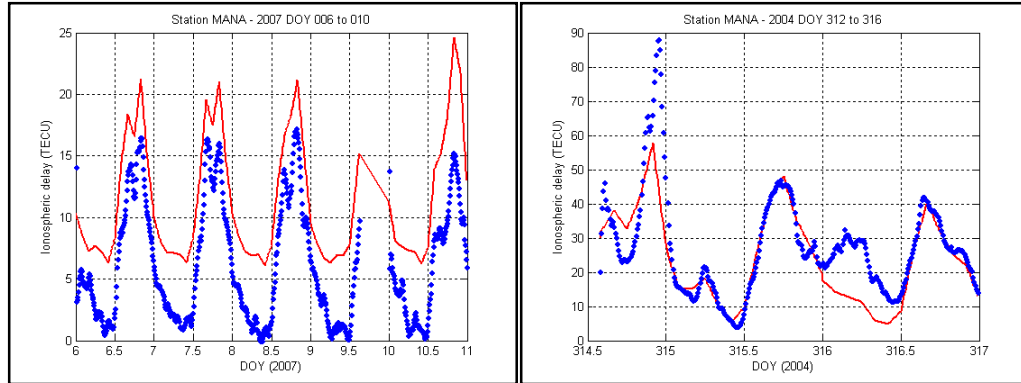


Figure 3.27. Comparison of results provided by GAPS (blue dots) and IGS (red line) for station MANA.

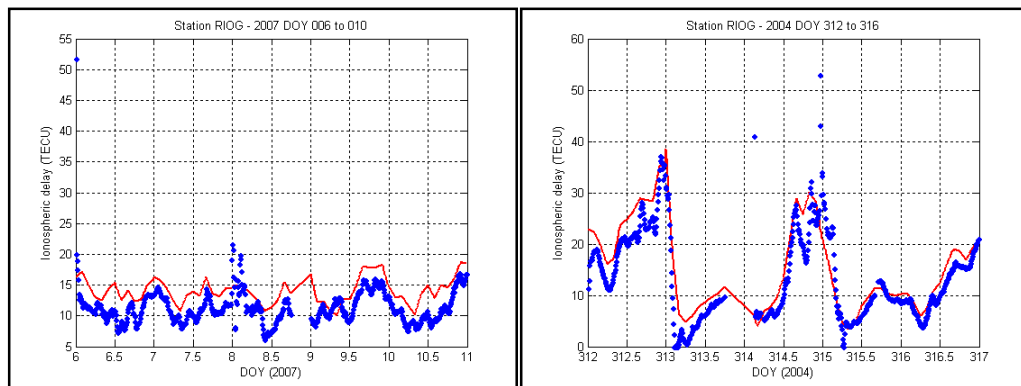


Figure 3.28. Comparison of results provided by GAPS (blue dots) and IGS (red line) for station RIOG, quiet period.

There are two effects in the above plots which deserve some discussion. One is the already mentioned interpolation smoothing effect from using IGS maps. Differences which might have been caused by this kind of effect can be seen for stations BRAN and LEEP on DOY 313, and station MANA on DOY 314. The other effect is the bias which usually exists between the two solutions. This is an effect of a disagreement between the satellite and receiver inter-frequency biases that are determined (explicitly or not) by the two techniques. Even though in the two cases the same effect from inter-frequency biases has to be handled, this is done in a completely different way in each technique, but even

then the ionospheric delays, which in theory are bias-free, should match. Table 3.2 shows the statistics of the comparison for each of the stations:

Table 3.2. Statistics of GAPS and IGS maps comparison (in the sense GAPS-IGS)

		Bias (TECU)	Std. Dev. (TECU)	RMS (TECU)
Quiet period	BRAN	-4.34	1.38	4.56
	LEEP	-4.31	1.31	4.50
	UNBJ	1.18	0.97	1.52
	FRDN	1.19	0.90	1.49
	MANA	-5.22	1.51	5.44
	RIOG	-2.66	2.23	3.47
Disturbed Period	BRAN	0.33	4.83	4.84
	LEEP	-0.44	4.56	4.58
	UNB1	-1.54	3.42	3.75
	FRDN	-1.23	4.14	4.31
	MANA	3.46	8.32	8.99
	RIOG	-2.16	3.80	4.36

It is noticeable that RMS values are better during the quiet period for all stations, which means that these techniques lose some of the modeling ability as the ionosphere gets disturbed. This effect should be expected because the assumptions behind the modeling techniques are less valid during storms when unpredictable effects happen. One of these assumptions, in case of GAPS, is that the ionosphere over the station can be modeled with two gradient parameters. In this case, it might be possible that better results during storm conditions can be obtained with more complex models, such as a quadratic function as used by Rho et al. [2004].

In general, the numbers shown in Table 3.2 are in agreement with the accuracy range claimed by IGS for its ionosphere maps (2-8 TECU for final maps – final maps were used

in this analysis). However, one should consider that the higher end of IGS claimed accuracy probably occurs at disturbed periods. We can see also that the biases (which can be translated into an agreement of instrumental biases determination) are in general within the level of agreement reported by Komjathy (2005) for JPL's biases consistency. These numbers become even more meaningful if one considers that we are comparing a station-network technique (IGS), with a single-station technique (GAPS). One of the possible causes for the difference between GAPS and IGS results is the fact that the ionospheric shell model used in each procedure is different. As a recommendation for future work I would suggest to modify GAPS' implementation to match IGS maps ionospheric shell model and analyze the differences that would be obtained. Another assessment which can be done in the future is using the computed delays for positioning of an independent station.

3.4. Chapter remarks

In this chapter I introduced a filter with which is possible to estimate ionospheric delays using a stand-alone receiver. This filter can be conveniently attached to a PPP engine. The observation model is based on geometry-free carrier-phase measurements, and considers the ionosphere as a earth-concentric spherical shell. The variation of the zenith ionospheric delays over the shell surface is modeled with a bi-linear polynomial. In analyses made with data of stations on south, central and north America, I found that the model residuals are usually less than 2 TECU pick to pick during ionosphere calm periods, and can reach values as high as 10 TECU (as far as the realized tests go) during

ionospheric storm picks. When comparing delay values independently obtained from two nearby stations, the results showed a very good agreement, of usually better than 0.3 TECU, besides two short periods of time when data of station FRDN seems not have been well handled by GAPS. When comparing the results with values provided by IGS, the time series behavior between the two estimates (IGS and GAPS) were found to be quite similar, however the results look to be biased at times. The overall agreement RMS seems to be around 4 TECU or so. Part of the mismatch might be caused by different assumptions used in the two estimates, such as the ionospheric shell height.

4. Estimation of code biases by means of PPP

One of the capabilities for data analysis that was implemented in GAPS, is the estimation of code biases. In this approach, the observations are treated in the same way as that for positioning, thus the impact of satellite biases is the same as for point positioning using IGS products. In this chapter, the code bias estimation approach is validated by comparing GAPS' satellite P1-C1 bias (i.e., the bias between the L1P(Y) and C/A code measurements) estimates with values determined by IGS analysis centers. In addition to that, P2-C2 bias (i.e., the bias between L2P(Y) and L2C code measurements) estimates for IIR-M satellites have been estimated. The scientific contribution of this chapter is to present an approach for PPP-based bias determination. I have also determined values for differential P2-C2 bias, which can be used in the future as a reference for further investigations related to P2-C2 satellite biases. Preliminary results of P1-C1 and P2-C2 bias determination have been published by Leandro et al. [2007]. Results for P1-C1 biases show a reasonable agreement with results provided by other research institutions, as will be discussed. The results show that the differential P2-C2 satellite biases for three of the modernized satellites are very similar, with the value likely between 0 and 20 cm.

4.1. Introduction

Hardware delay is one of the effects which has to be taken into account when using GPS under certain conditions (e.g. single point positioning). These delays can be different for

each observable and for each frequency, which means that depending on the observable which is being used in a given application, accounting for hardware delays might be an mandatory step achieving the targeted accuracy. A hardware delay is usually determined in a relative sense, where a given observable and frequency (or frequency combination) is used as standard. Because of this, the values which are determined are usually called relative biases, since they represent the bias between two observable types, and can be represented either in time or in length units. One can separate the instrumental biases into two classes: the inter-frequency biases, which are the biases between observables on different frequencies; and, the intra-frequency biases, which are the biases between two observables on the same frequency.

The inter-frequency bias is a matter of interest for estimating ionospheric delays, which requires a comparison between observations on different frequencies. It is also of interest for positioning with single-frequency receivers, because the satellite clocks are usually computed using the ionospheric delay free (iono-free) combination and thus the bias between the receiver's observable type (usually C/A or L1 P(Y) code) and the iono-free observable should be accounted for to allow a correct time transfer and consequently adequate positioning.

In this chapter I will refer to GPS observables in the text using the same naming convention as in the RINEX standard [Gurtner and Estey, 2006], where L1 C/A code is called C1, L1 P(Y) code is called P1, L2C code is called C2, and L2 P(Y)code is called P2. Additionally, it is worth mentioning that only L2C code measurements derived using

both CM (civil-moderate) and CL (civil-long) code sequences are used. Also, P2 code observed using a cross-correlation technique is to be called P2' hereafter.

The intra-frequency biases are of interest for two types of applications: network data processing and single receiver data processing. Sometimes, networks are formed by receivers of several types, collecting different observable types. Currently, the only intra-frequency bias of wide interest for the GPS community is the P1-C1 bias. P1 and C1 observables may have to be mixed in networks formed by non-cross-correlation receivers (which collect P1 and P2, such as Javad Legacy), non-cross-correlation receivers reporting C1 (which collect C1 and P2, such as Trimble NETR5, Leica GRX1200PRO, Novatel OEM4), and cross-correlation receivers (which collect C1 and P2', such as Rogue SNR-12, Trimble 4000SST, Topcon TT4000SSI). On the single receiver side, the need to account for biases depends on whether the receiver is using the same observables which were used to compute satellite clock errors or not.

It is important to mention that the hardware delays, and consequently the biases, exist for both receivers and satellites. In a point positioning scenario, the receiver's biases are usually absorbed by the receiver clock error parameter in the adjustment as long as only one type of observable is being used, thus only the satellite biases have to be taken into account in this case. In the same sense, instrumental biases are in general not an issue for relative positioning, because they are eliminated together with satellite and receiver clocks in the double-differencing.

4.2. PPP-based P1-C1 code bias estimation

One simple way of estimating code biases is by comparing two different codes simultaneously observed by the same receiver. This technique delivers the receiver-satellite differential bias, which means the receiver part of the estimated quantity still has to be eliminated in order to obtain the satellite bias. Because the biases can be considered as a more or less constant correction over time for the satellite clock error estimates used in positioning, it is desirable that these biases are estimated in a way in which the consistency between biases and clock products is assured. This is usually done, since the differential satellite code biases are generally estimated together with the satellite clocks, as it is done for example at the Center for Orbit Determination in Europe (CODE) [CODE, 2007]. In the PPP-based technique, we match this approach by using the clock products for estimating the satellite differential biases, as will be seen later.

In order to estimate code biases, a novel technique based on precise point positioning was developed inside GAPS. To explain how this technique works, we should start with the simplified pseudorange observation equation. The equation assumes that IGS clock products are being used, thus the clocks are referenced to a P1 and P2 iono-free combination:

$$P_{if(P1,P2)} = R + c(dT - dt) + T + m_{P_{if(P1,P2)}} + e_{P_{if(P1,P2)}}, \quad (4.1)$$

where:

$P_{if(P1,P2)}$ is the P1 and P2 iono-free pseudorange measurement; R is the geometric range; T is the neutral atmosphere delay; c is the speed of light; dT is the receiver clock offset; dt is the satellite clock offset; $m_{P_{if(P1,P2)}}$ is the iono-free code multipath, and; $e_{P_{if(P1,P2)}}$ represents other errors in the measurements.

As one can notice, there are no biases being considered in Equation 4.1, because the same observation combination as the one used to determine satellite clocks (in this case, P1 and P2 iono-free combination) is being used at the receiver. In the case of single frequency observations, the satellite code bias should be considered, as shown below for the P1 code measurement simplified equation:

$$P_1 = R + c(dT - dt) + T + I + b_{if-P1} + m_{P1} + e_{P1}, \quad (4.2)$$

where the additional terms are:

P_1 is the P1 pseudorange measurement; I is the ionospheric delay; b_{if-P1} is the satellite instrumental bias between the P1 and P2 iono-free combination and P1 code (necessary in this equation because we are using IGS iono-free clocks but dealing with L1 frequency measurements – in this case, P1); m_{P1} is the P1 multipath, and, e_{P1} represents other errors for P1 measurements.

One can notice that an explicit receiver bias term is missing in Equations 4.1 and 4.2. This is because, as mentioned before, in a PPP scenario the receiver code biases are absorbed by the receiver clock parameter (dT in equations 4.1 and 4.2). If one is using C1 rather than P1 measurements for positioning, a similar equation should be used, with the addition of the P1-C1 bias:

$$C_1 = R + T + I + c(dT - dt) + b_{if-P1} + b_{P1-C1} + m_{C1} + e_{C1}, \quad (4.3)$$

where b_{P1-C1} is the satellite instrumental bias between P1 code and C1 code, and C_1 is the C1 code measurement.

An iono-free observable using C1 and P2 codes would still require the use of the P1-C1 bias, as follows:

$$P_{if(C1,P2)} = R + T + c(dt - dT) + \alpha \cdot b_{P1-C1} + m_{P_{if(C1,P2)}} + e_{P_{if(C1,P2)}}, \quad (4.4)$$

where α is the coefficient for L1 in the iono-free combination equation:

$$P_{if(C1,P2)} = \alpha \cdot C1 - \beta \cdot P2, \quad (4.5)$$

where α can be computed as:

$$\alpha = \frac{f_1^2}{f_1^2 - f_2^2}, \quad (4.6)$$

and β can be computed as:

$$\beta = \frac{f_2^2}{f_1^2 - f_2^2}. \quad (4.7)$$

Using information related to orbits, clock, atmosphere and receiver position which is inherent to a precise point positioning filter (i.e., they are either used as known information or estimated as parameters), it is possible to create a pseudo-observable as follows:

$$P'_{\text{if}(C1,P2)} = P_{\text{if}(C1,P2)} - R - T - c(dT - dt), \quad (4.8)$$

and therefore:

$$P'_{\text{if}(C1,P2)} = \alpha \cdot b_{P1-C1} + m_{P_{\text{if}(C1,P2)}} + e_{P_{\text{if}(C1,P2)}}, \quad (4.9)$$

where $m_{P_{\text{if}(C1,P2)}}$ and $e_{P_{\text{if}(C1,P2)}}$ are un-modeled parameters, where $e_{P_{\text{if}(C1,P2)}}$ includes residual orbit errors, residual satellite clock errors, residual neutral atmosphere delay errors, and receiver noise. The equation above might be simplified resulting in the following equation:

$$\tilde{P}'_{\text{if}(C1,P2)} = \alpha \cdot b_{P1-C1} \cdot \quad (4.10)$$

One single observation of one single receiver is enough to determine the satellite P1-C1 bias. However, because of the part of the observation which is not modeled (multipath, noise, and residual systematic effects), the determination with one single measurement would not be accurate. This can be clearly seen in Figure 4.1, where each blue dot represents the determination of the PRN03 satellite P1-C1 bias from a single observation, i.e., one independent epoch solution for the bias. It is possible to notice that even though the dots are scattered around a stable level (the bias), there is a significant amount of noise. Looking at the corresponding elevation angle plot it is possible to see that the noise level is higher for lower elevation angles, as one should expect.

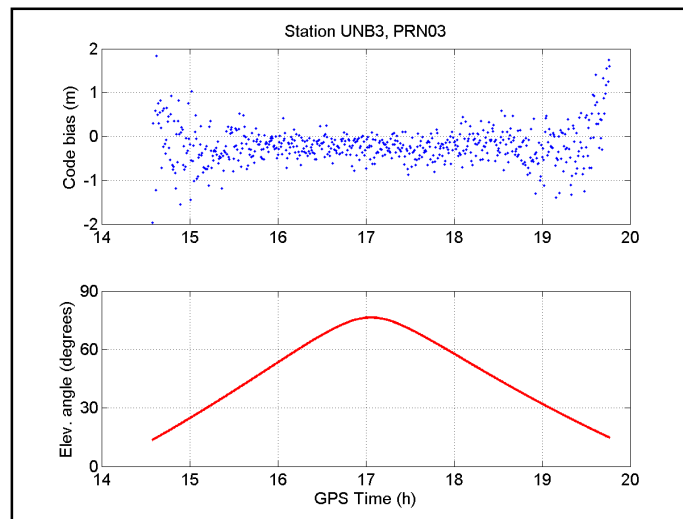


Figure 4.1. P1-C1 bias estimation, according to Equation 4.10, for station UNB3, PRN03, on DOY 280 of 2007.

What would be feasible though is using several observations of a receiver (in other words, a complete arc of a given satellite), which would reduce the effect of the noise. Also, using receivers in different locations (and thus with different multipath patterns) would reduce the effect of the multipath. Using several observations from one or several receivers requires an adjustment procedure, which might follow the standard least-squares technique:

$$\hat{\mathbf{b}} = (\underline{\mathbf{A}}^T \underline{\mathbf{P}} \underline{\mathbf{A}})^{-1} \underline{\mathbf{A}}^T \underline{\mathbf{P}} \underline{\ell}, \quad (4.11)$$

where:

$\hat{\mathbf{b}}$ is the estimate of the bias; $\underline{\mathbf{A}}$ is the design matrix, which, in this case, is a column vector where all elements are α ; $\underline{\ell}$ is the vector of observations (in this case, $\tilde{P}'_{\text{if}(C1,P2)}$); and $\underline{\mathbf{P}}$ is the weight matrix.

The weights of $\underline{\mathbf{P}}$ should vary according to the elevation angle of each observation.

Assuming the effect of multipath is less critical for higher elevation angles, an elevation-based weighting scheme (similar to what was used earlier) should help to reduce the impact of multipath on the bias estimation. The uncertainty of a single bias determination can be estimated according to:

$$\sigma_b = \sqrt{\frac{(\ell - \hat{b})^t P(\ell - \hat{b})}{(A^t P A) df}}, \quad (4.12)$$

where

σ_b is the 1-sigma uncertainty estimate; df is the number of degrees of freedom of the adjustment, which is the number of observations minus one, assuming the observations are un-correlated.

Figure 4.2 shows the epoch per epoch estimates for PRN03 P1-C1 bias over 10 days, using UNB3 data.

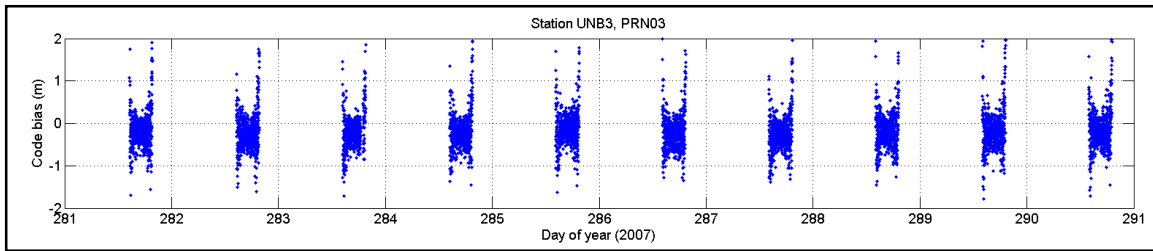


Figure 4.2. Epoch per epoch estimates for PRN03 P1-C1 bias over 10 days, using UNB3 data (elevation cutoff 10 degrees).

It is possible to notice that the behavior pattern of the bias estimates repeats every day, which is expected for any geometry-dependent effect such as multipath. It is also possible to notice that the mean value of the estimates is somewhat stable over the days. In order to better visualize that, Figure 4.3 shows the daily bias estimates and their respective estimated uncertainties (1-sigma), which are represented by the blue line. The dashed red line represents the overall bias estimate, which is $(-22.7 \pm 0.4 \text{ cm})$. All estimations shown in Figure 4.3 were done according to Equations 4.11 and 4.12.

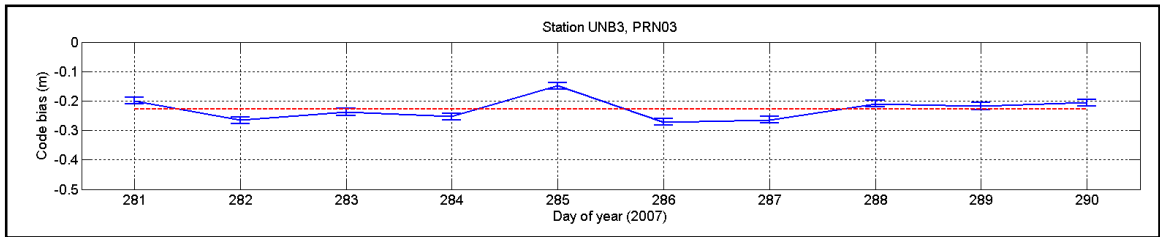


Figure 4.3. Daily PRN03 P1-C1 estimations using UNB3 data.

In the plot above, we can see that the daily estimates fluctuate around the 10-day overall estimate by a few centimeters. We can also notice that the 1-sigma error bars usually do not bound the average values represented by the dashed red line. This means that the uncertainty estimate is optimistic, probably because residual effects which vary from one day to another – these effects might likely be residual orbit errors, residual satellite clock errors, or residual neutral atmosphere delay estimation errors. In future work it would be worth looking into what is the exact reason for the unrealistic bias uncertainty estimates.

Even though the estimated uncertainties are not a faithful representation of reality, the variation of the daily bias solutions with respect to the mean is reasonably small, with values usually below 4 cm. Figure 4.4 shows the difference between each daily estimate and the overall estimate.

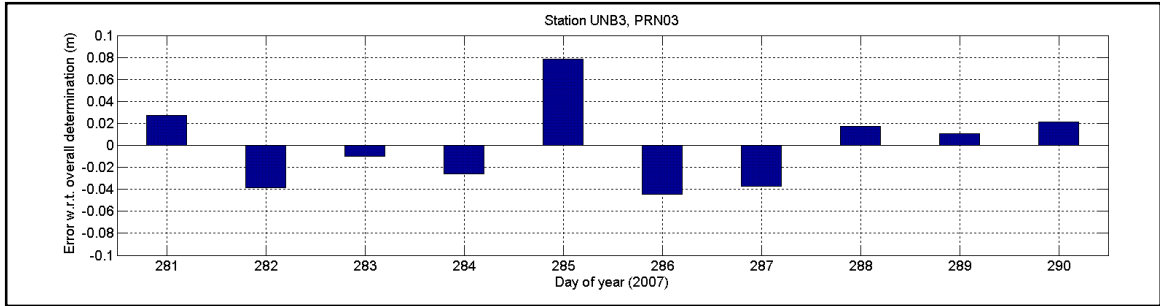


Figure 4.4. Deviation of bias daily estimates from the 10-day estimate.

In the plot above, we can see that there is a reasonable stability of the daily bias estimates for PRN03 over the 10-day period. Similar computation were made in order to verify if this is also true for estimates of biases of other satellites, using the same data, in the same period. Figure 4.5 shows the daily results for all 30 satellites observed at UNB3 during this period.

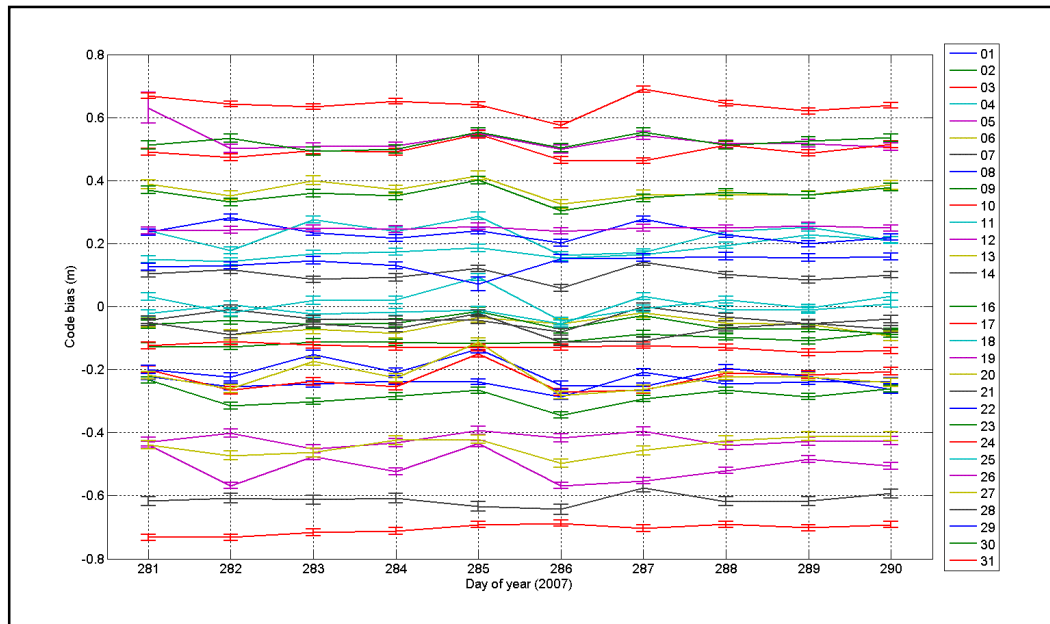


Figure 4.5. Daily P1-C1 bias results for all satellites, using UNB3 data.

In Figure 4.5, we can see that the daily solution for each satellite is reasonably stable over time (in this case 10 days), similar to PRN03. Another noticeable characteristic of the estimation shown above is that the mean value of all the satellite biases is very close to zero. Figure 4.6 shows the mean value of the P1-C1 bias among all satellites for each of the ten days. The overall value (over the 10-day period) of the mean is -0.3 ± 1.3 cm, which means it is statistically equivalent to zero.

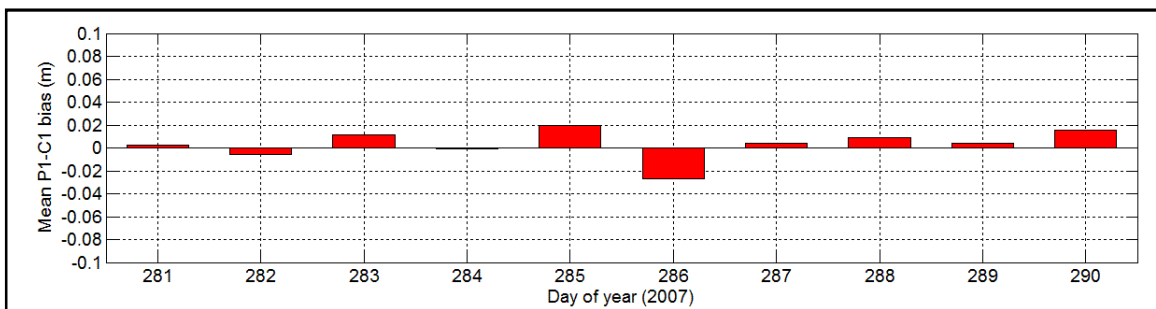


Figure 4.6. Daily mean P1-C1 biases.

This effect (near zero mean) occurs because in PPP data processing any effect common to all satellites is absorbed by the receiver clock parameter. This indicates that the receiver-dependent hardware delay (in other words, the receiver code bias) is absorbed by the clock parameter (under the assumption that this bias is the same for all receiver channels), and thus the PPP code bias estimates are receiver-bias free (i.e., they are a direct measure of the satellite differential code biases). One can say that when computing differential code biases with the PPP approach, an implicit zero-mean condition is applied, by means of the receiver clock estimation. This effect applies when estimating the biases and also when using bias values for point positioning, which means that the set

of satellite biases used for positioning may have any mean value, as long as the differences among satellite biases is consistent.

As a next step, I use the 10-day UNB3 dataset previously mentioned to determine the mean satellite P1-C1 code bias for each satellite for that whole period. Figure 4.7 shows the resulting satellite P1-C1 bias.

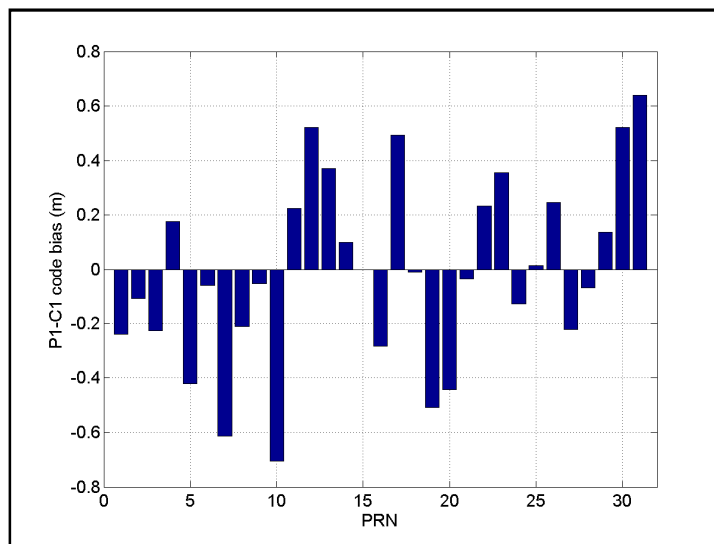


Figure 4.7. Satellite P1-C1 code biases determined using the 10-day UNB3 dataset

In order to have a an idea of how close these values are from an independent solution I have obtained CODE's monthly GPS P1-C1 DCB (differential code bias) solution (from the global IGS network) for October of 2007. The claimed uncertainties for this particular CODE DCB solution range from 0.06 cm to 0.36 cm.

CODE has accounted for P1-C1 code biases since GPS week 1057 (beginning 9 April 2000) by solving for satellite-specific differential (P1-C1) DCB parameters as part of the

clock estimation procedure. Their approach works as long as a mixture of data of cross-correlation style receivers and modern receivers is processed. At present, between 30 and 40 stations from a total of 80 stations used for the clock estimation may be related to a cross-correlation style receiver providing C1 and P2' code measurements [CODE, 2007]. The P2' code is the P2 code observed by a cross-correlation receiver and within CODE standard nomenclature it is called X2.

The comparison between GAPS and CODE solutions is shown in Figure 4.8, where we can see that there is reasonable agreement between them.

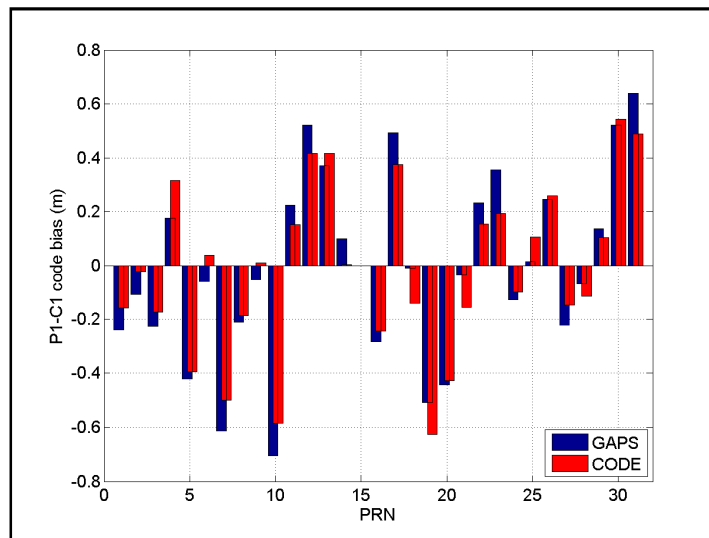


Figure 4.8. Comparison between P1-C1 satellite biases provided by CODE and computed with GAPS (using data from UNB3).

Figure 4.9 shows the difference between these two solutions, in the sense of GAPS-CODE, where the discrepancies are within about -15 cm and 15 cm. The RMS of the differences is 9 cm.

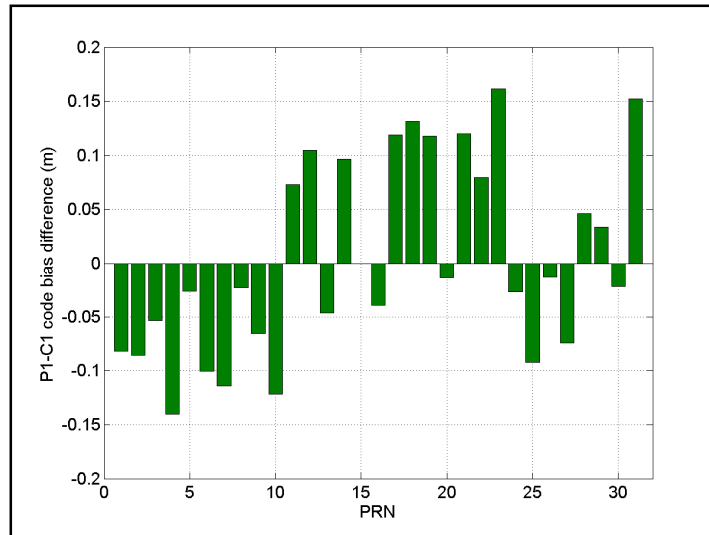


Figure 4.9. Difference between P1-C1 satellite biases provided by CODE and computed with GAPS (using data from UNB3).

Even though the RMS obtained (9 cm) is not small when compared to CODE’s bias uncertainties, this agreement should still be regarded as very good, considering that we are estimating a bias set valid for nearly the whole GPS constellation with one single receiver, using data observed over 10 days. This means that CODE’s determination is done with roughly 240 times more data than what was used in the UNB3 determination, and using a well distributed worldwide network.

Another aspect which should be mentioned is that, if we consider CODE DCB values as truth, GAPS’ estimated standard deviations are quite optimistic. Figure 4.10 shows the uncertainties (1-sigma) computed for GAPS, CODE, and the difference between the two solutions.

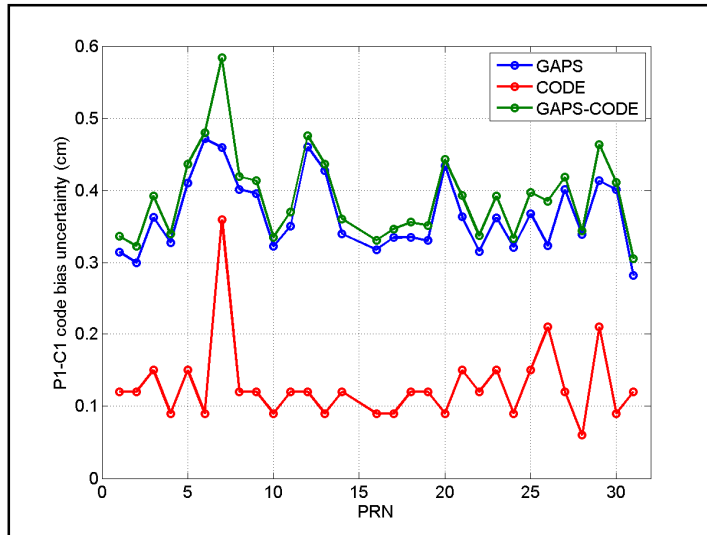


Figure 4.10. Estimated uncertainties for the two solutions and their difference.

As it can be seen in the plot above (in which the y axis is in cm), the uncertainties estimated for the difference between the two solutions are quite a bit less than the actual computed differences (shown in Figure 4.9).

In an attempt to obtain more meaningful estimates for the code biases, I have made an estimation with a number of different stations. The data which was used for this analysis is from the IGS L2C Test Network. There are two reasons for using this dataset: (1) Since this is an IGS network which was built for test purposes, this data, as of January 2007, was not supposed to be used for ongoing precise products generation. Therefore, it can be considered an independent data set when I compare GAPS' results with CODE's; and, (2) The data contains L2C observations, which will be used in the analysis of the next section. In next section more details about the L2C Test Network and the L2C signal will be given. The data used in this analysis was collected over the whole month of January 2007. There is no particular reason for the choice of this time period, and in the future

other time periods should be investigated in further research. As of January 2007, the network was composed of the following receivers:

Table 4.1. L2C Test Network stations (as of January 2007)

Station	Latitude (degrees)	Longitude (degrees)
BHAO	36.09	128.58
GANP	49.02	20.19
HRAC	-25.53	27.41
KOKC	22.07	-159.39
MCMC	-77.50	166.40
NYAC	78.55	11.51
OURI	-22.95	-49.90
PGC5	48.38	-123.27
RIOP	-20.79	-49.36
ROSA	-22.52	-52.95
UNAC	40.03	-105.12
UNB3	45.57	-66.38

For two reasons, only a subset of 8 stations (GANP, HRAC, KOKC, MCMC, NYAC, PGC5, UNAC, and UNB3) was used in my analysis. The first reason is the availability of files in RINEX 2.11 format, which is supported by GAPS. The second reason is the data availability – there was data missing for some stations.

Figure 4.11 shows the results of P1-C1 bias determination for each station/day. Each line represents the results for all PRN's, computed from data from one station over one day (i.e., one line per station/day). It can be noticed that the agreement over the different days/stations is of several decimeters. As was previously shown, the bias determination made with data from one station on one day has an RMS of nearly one decimeter as compared with CODE's published biases.

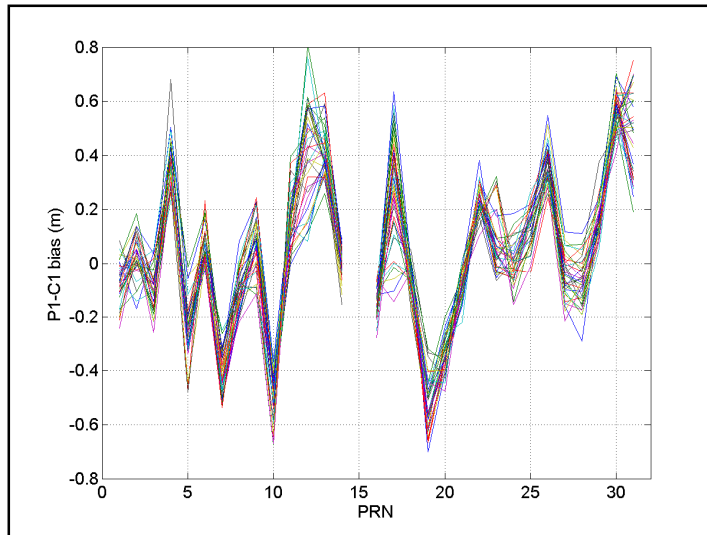


Figure 4.11. P1-C1 bias determination results for each station/day.

Figure 4.12 shows the estimated uncertainties for each day/station, where it can be seen that they are mostly in the range of 3-5 cm.

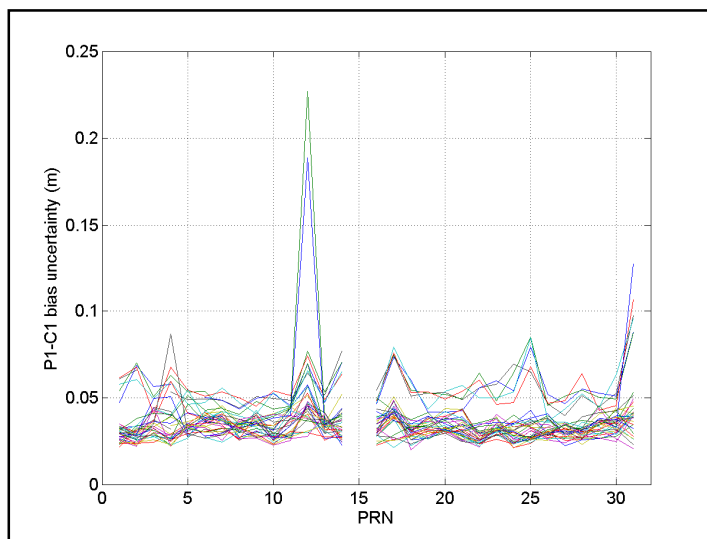


Figure 4.12. Estimated uncertainties for P1-C1 bias determined for each station/day.

Satellites from Block IIR-M (PRNs 12, 17 and 31) show a generally worse agreement (Figure 4.11) and uncertainty (Figure 4.12) because these results are affected by the untreated P2-C2 bias, and the impact of this is different for each station depending on the receiver P2-C2 bias value, and the availability of the IIR-M satellite over the day for this station. For these satellites, the observable C2 was used instead of P2, to allow the P2-C2 bias determination which will be discussed in the next section. As will be discussed later, at this point results for these satellites still have effects which have to be removed.

The first great advantage of combining data from different stations is getting data at different elevation angles for a given satellite, mainly data at high elevation angles, which has less impact of effects such as multipath and residual neutral atmosphere delay errors. The second advantage is the possibility of averaging out part of the geometry-dependent effects, which include multipath, residual neutral atmosphere delay errors and residual orbit errors. Satellite clock error is not a geometry-dependent effect (i.e., it affects all stations in the same way), and thus it is not reduced with combination of more data – the only way to reduce its residual effects is using data over longer periods of time, under the assumption that the residual satellite clock error will behave as a zero-mean effect over long periods of time. Figure 4.13 shows the overall result for a unique P1-C1 bias determination using the whole 31-day period covered by this dataset, for each satellite.

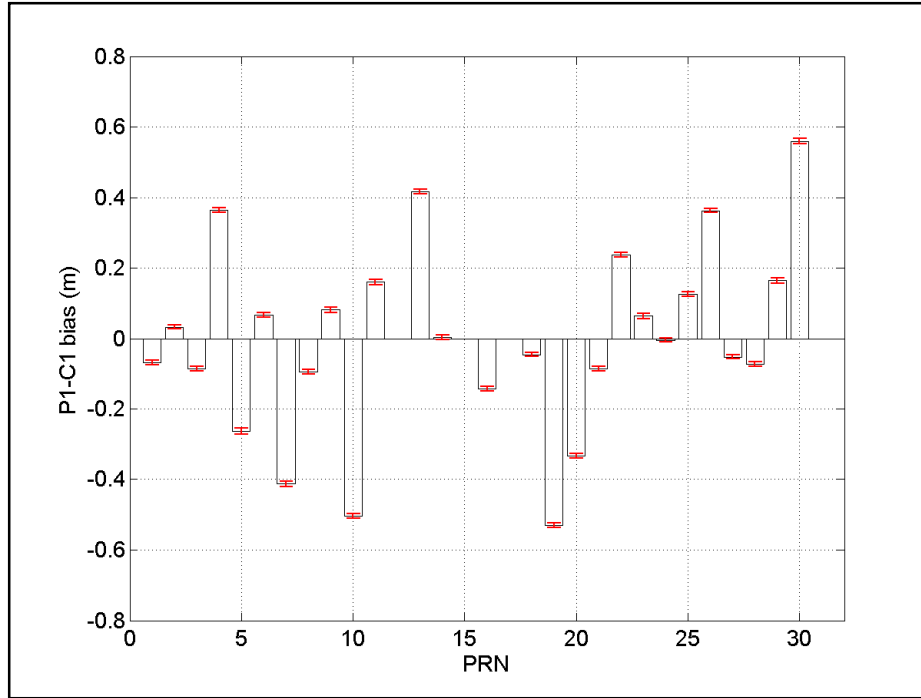


Figure 4.13. GAPS-determined P1-C1 biases (white bars) and respective uncertainties (red error bars) for non-Block IIR-M satellites.

In the plot above PRNs 12, 17 and 31 are missing for the reasons already explained. The shape of the bars is similar to the ones in Figure 4.7, with a few centimeter level differences. As can be noticed, the uncertainties are quite a bit smaller than the single day/station result uncertainties shown in Figure 4.11. The improvement in uncertainty is an expected effect from combining data and can be very easily understood by looking into basic error propagation laws. As before, all the computations were done following the equations shown earlier in this section. In order to verify the agreement between this solution and CODE's solution, Figure 4.14 shows the comparison between them.

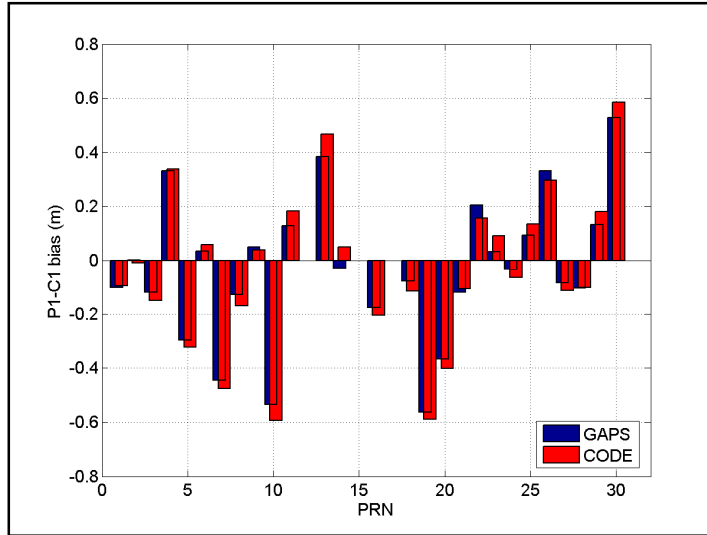


Figure 4.14. Comparison between P1-C1 determined with GAPS and CODE's values.

As before, there is a reasonable agreement between GAPS results and P1-C1 values provided by CODE. Figure 4.15 shows a plot with the differences in the sense GAPS-CODE. The scale of the Y axis is the same as in Figure 4.9, which makes it easy to notice the improvement in agreement, when comparing the network bias determination with the single station determination.

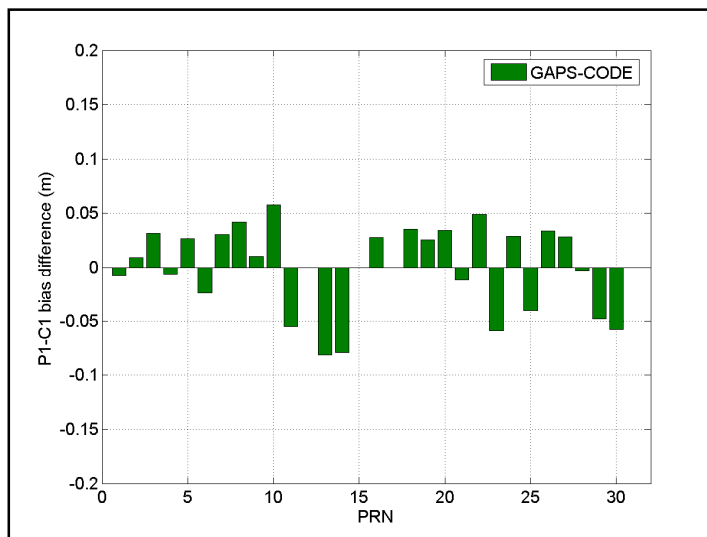


Figure 4.15. Differences between P1-C1 determined with GAPS and CODE's values.

The RMS of these differences is 4.1 cm, which is more than two times better than the agreement reached with the single station approach. The maximum absolute discrepancy is 8.1 cm. All the discrepancy-related values are less than the uncertainty of code measurements themselves and therefore, taking into consideration the noise level of pseudoranges to which these biases would be applied, there is no statistical difference between these solutions. Nevertheless, we should take a look at the estimated uncertainty with respect to the actual discrepancies. Figure 4.16 shows the uncertainties of the GAPS solution, of the CODE solution, and of the difference between them. As in Figure 4.10, the unit of the Y axis is centimeters.

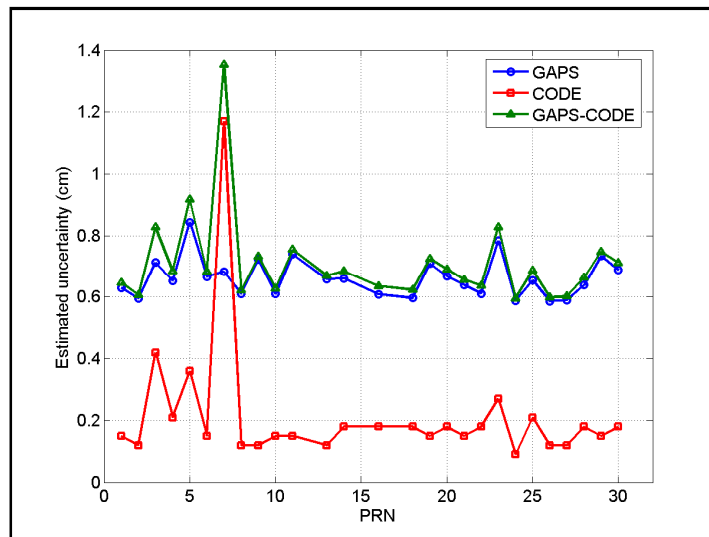


Figure 4.16. Estimates uncertainties for P1-C1 bias solutions and their differences.

As before, the uncertainties are optimistic and therefore are much less than the actual discrepancies. One thing which is interesting to notice is that the overall behavior of the

uncertainties is somehow similar between the two solutions, if some outlying satellites (e.g. PRN 7) are not considered.

4.3. PPP-based P2-C2 code bias estimation

The United States has started a modernization program to provide better service to Global Positioning System (GPS) users, with launches of modernized GPS satellites. The subgroup of these new satellites is called Block IIR-M, where "R" stands for replenishment and "M" for modernized. In this modernization process, GPS has gained a new open civil signal (called L2C), centered on the L2 frequency. The first modernized satellite, for which PRN17 was assigned, was launched on 25 September 2005 and the new L2C signal from this satellite has been fully available since 15 December 2005. Even before PRN17 was placed in orbit, the L2C signal became an issue of worldwide interest to the GPS research communities. Currently L2C is being transmitted by six satellites: PRN17, PRN31, PRN12, PRN15, PRN29 and PRN07. Enhanced receivers capable of tracking the modernized GPS signal have been developed and provided by a number of manufacturers. The IGS has organized a network of L2C signal tracking stations which have been established in different places around the world. The role of projects involving the new signal is to analyze its quality, as well as the impact of its use for positioning and navigation.

Until the end of 2005, only one code was broadcast on frequency L2, the encrypted military P2 code, and for this reason intra-frequency biases have never been an issue on

L2. With the launch of the first IIR-M GPS satellites, a second code started to be broadcast on L2, the L2C code (called C2 code in RINEX version 2.11 standard), where C stands for civil (thus, an open civil signal). Around the same time, many of the GPS receiver manufacturers started to produce and to put on the market receivers capable of tracking the L2C signal, which made this new observable a matter of interest for the GPS community. The International GNSS Service organized a network of continuously operating L2C-capable GPS receivers, called the L2C Test Network. These receivers are operated by a number of institutions all over the world.

One of the aspects of the new code which has to be investigated is the bias between itself and the pseudoranges from P(Y) tracking, which will become necessary for L2C users when a reasonably full modernized satellite constellation is available, to allow positioning based on L2C rather than on L2P(Y) for certain satellites. The knowledge of the differential biases is a requirement for mixing different code types; otherwise the biases need to be estimated as parameters, what might not be desirable in certain cases. In this chapter we are presenting a determination of the P2-C2 satellite biases. This determination was made possible using data from the L2C Test Network, and a technique based on precise point positioning, which itself is another novel aspect of this work.

One of the issues to be considered when dealing with the new signal is the impact of mixing L2C-capable and legacy receivers within a network, or processing data from an L2C-capable receiver with satellite clock values generated using a legacy receiver network. Because hardware delays of receivers and satellites for L2C measurements

(called C2 in the RINEX 2.11 standard) might not be necessarily the same of those for P2 (pseudoranges based on semi-codeless L2 P(Y)-code tracking), a bias between P2 and C2 code measurements must be considered when mixing observations from different signals and/or tracking techniques . This bias will be called here the P2-C2 bias, using the same standard nomenclature used for P1-C1 biases. Code biases are present in the receiver and the satellite hardware, but in a positioning scenario, receiver code biases are usually absorbed by the receiver clock parameter and do not need to be separately accounted for. In a scenario of network clock (receivers and satellites) estimation using mixed receiver types (e.g., legacy and L2C-capable), both receiver and satellite biases have to be considered as parameters in the observational model.

Knowing these values allows us to begin using C2 code as an observable for positioning, applying satellite clock values computed using P2 as the observable on L2, as in the case of IGS clock products. The dataset used is the data observed by the IGS L2C Test Network.

The L2C Test Network was created in an effort of the IGS to create a pool of data from globally distributed L2C-capable receivers. It has been established as voluntary contributors start to submit their data to be stored on the NASA Goddard Space Flight center CDDIS (Crustal Dynamics Data Information System) ftp server. L2C Test data can be accessed from <<ftp://cddis.gsfc.nasa.gov/gps/data/l2ctest/>>.

All receivers of this network are non-cross-correlation receivers reporting only C1 for the L1 frequency, which means the codes available in addition to L2C's are C1 and P2.

Following the same procedure used to derive Equation 4.4, we can now derive the observation equation of the iono-free code combination using C1 and C2 (or L2C-based) codes:

$$P_{\text{if}(C1,C2)} = R + T + c(dT - dt) + \alpha \cdot b^s_{P1-C1} + \beta \cdot b^r_{P2-C2} + \beta \cdot b^s_{P2-C2}, \quad (4.13)$$

where b^s_{P1-C1} is the satellite P1-C1 bias, b^r_{P2-C2} is the receiver P2-C2 bias, b^s_{P2-C2} is the satellite P2-C2 bias and β is one of the coefficients of the iono-free combination, as in Equation 4.4 – but now using C1 and C2 codes.

The P2-C2 receiver bias term is not absorbed by the receiver clock parameter because L2C observables were available only for three satellites at the time of the data collection, and the consequence is that we are forced to use the other satellites to be able to provide a PPP solution, which means the receiver clock is absorbing the receiver P1-C1 bias only. We know that only P1-C1 biases are being absorbed by the clock because we actually force that, by giving more weight to legacy satellites than for modernized ones in the PPP solution. The satellite P1-C1 bias is present in this equation simply because no biases were applied to the observations prior to data processing.

In order to isolate the parameter of interest – the satellite P2-C2 bias, we used a zero-mean condition for each station solution, which eliminates the receiver-dependent part of the bias. The satellite P1-C1 bias was taken care of by removing it using the values provided by CODE for January 2007. CODE’s determination can be used here since its consistency with our approach has been checked, as shown in the previous section.

After eliminating the biases which are not of interest for this analysis, it is possible to create the pseudo-observable for the P2-C2 bias, as done for P1-C1, as follows:

$$\tilde{P}'_{if(C1,C2)} = \beta \cdot b_{P2-C2}. \quad (4.14)$$

The bias estimate can be computed using the same procedure, by least squares technique, as shown in Equations 4.11 and 4.12.

Figure 4.17 shows the values obtained for several solutions for different receivers on different days (not in any specific ordering) with their respective uncertainties. It is possible to notice that the range of the estimated biases for the three satellites is usually small, considering the estimated uncertainties, which overlap each other in many cases. There is some variation on the behavior of the biases, whose reason is likely the difference in the satellite geometry depending on the location of each station. As shown before in Figure 4.12, differences of determination by different receivers might get up to around 2 decimeters, what means the use of a network of receivers reasonably distributed is crucial for obtaining meaningful estimates. Another indication of this which was

shown earlier was the clear decrease (more than 2 times) of the P1-C1 bias RMS when estimating them using a network rather than a single receiver.

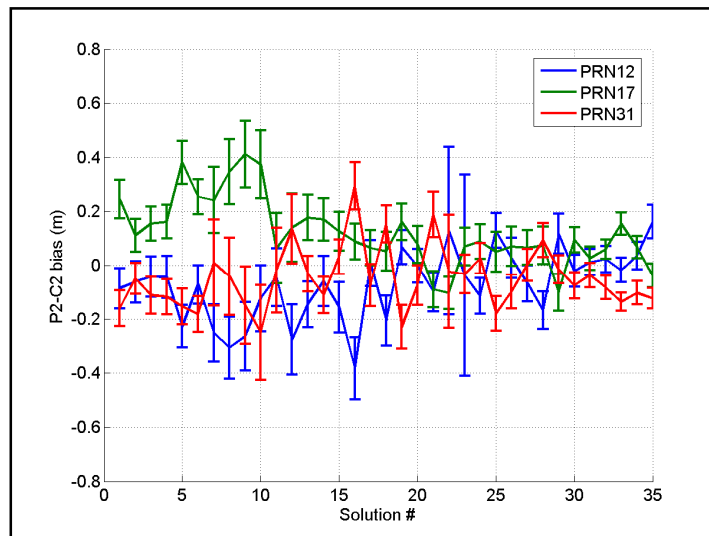


Figure 4.19. Results of the P2-C2 satellite bias determination for several days and stations.

Table 4.3 shows the overall results obtained for the satellite P2-C2 biases and respective standard deviations.

Table 4.3. P2-C2 satellite biases.

PRN	Bias (cm)	Std. dev. (cm)
12	-3.8	1.9
17	9.0	1.7
31	-6.5	1.6

Table 4.3 shows that the range of the determined values is reasonably small if compared to the range of the P1-C1 biases. P2-C2 biases determined for PRNs 12 and 31 showed to be not statistically distinguishable, still reasonably different from PRN17. There have been two other determinations for P2-C2 biases. The first published determination was made in Leandro et al. [2007] (2). Later in the same year, al-Fanek et al. [2007] also

published results for these quantities (3). Table 4.4 shows the biases and their uncertainties for these three determinations ((1) to (3), respectively). The zero-mean condition was applied to all determinations.

Table 4.4. P2-C2 satellite biases.

PRN		Bias (cm)	Std. dev. (cm)
12	1	-3.8	1.9
	2	-6.0	6.0
	3	-12.6	-
17	1	9	1.7
	2	11.7	8.1
	3	11.3	-
31	1	-6.5	1.6
	2	-4.7	7.1
	3	1.3	-

al-Fanek et al. [2007] didn't provide uncertainties for their determination, however they mention a stability of 2 cm over a two-week period. In order to assess this number, one should have in mind that their determination was evaluated with two receivers, sharing the same antenna. As previously shown in this work, estimates coming from the same station (i.e., similar geometry) are likely stable over time (see e.g. Figure 4.5) to a few cm level. This does not mean that this estimation has centimeter level accuracy, although they usually have a good precision. Another interesting point is that in their work, al-Fanek et al. [2007] used a simulator-receiver setup to determine and later remove the receiver-dependent P2-C2 bias, however one should have in mind that the biases, as treated here, really refer to the whole setup of antenna, pre-amplifier, cables and receiver, therefore perhaps values coming from their determination are not truly comparable to mine. Even then, the differences between my determination (1) and determination (3) are

less than 10 cm and might well be caused by the fact that in (3) only one station (two receivers, but one single antenna) was used for the estimation.

As can be seen, P1-C1 biases of the three modernized satellites are reasonably similar, a similar characteristic to what we have detected for the P2-C2 biases. We can also see that these values are different from zero, even though small. This happens because they were determined in conjunction with the P1-C1 biases of all satellites, which causes the increase in the range of bias values, as can be seen in Figure 4.2.

When looking into the differences between solutions (1) and (2), we can see that the biases are different by around 2-3 cm, which is very reasonable when compared to the uncertainties of the biases, mainly the ones from (2).

4.5. Chapter remarks

In this chapter, I presented a new technique to estimate satellite differential code biases based on PPP. A comparison of estimated satellite P1-C1 biases with a monthly CODE solution showed an overall agreement of around 9 cm and 4 cm, for a single station and a network of stations, respectively.

Satellite P2-C2 differential code biases were also estimated (for PRN12, 17 and 31 modernized satellites). Bias values of two satellites (PRN12 and PRN31) are very similar, but different from PRN17 by around 12-15 cm. As more modernized satellites are

launched, this situation might change, which means that if new satellites have different values for their P2-C2 biases, the range of the differential biases will increase, forcing the values to be farther from zero, in case a zero-mean condition is used.

For future research, I suggest work on different validation procedures, maybe with different sources and a larger dataset. Also, activities should be established to keep tracking the bias value behaviors as new modernized satellites are launched, as well as tracking the behavior of these values over time.

5. Code multipath and noise estimation with PPP

In this chapter I discuss another special capability of GAPS, designed to provide estimates of code multipath plus noise (i.e., un-modeled errors). In addition to describing and analyzing the technique, I will briefly discuss another technique which can be used for the same purpose, which has been described in Langley [1998] and has been widely used by the scientific community as one of the utilities of the TEQC software [UNAVCO, 2007]. A comparison between GAPS' and TEQC's estimate is done. I also present results from a case study involving L2C data quality analysis. The estimation of code biases shown in the previous Chapter can be actually seen as a byproduct of a code multipath plus noise estimation process. This is because of one of the main characteristics of the multipath plus noise estimation technique presented here - the average effect is not lost since it does not directly depend on phase ambiguities.

5.1. Iono-free code multipath plus noise estimates

The derivation of the PPP-based code multipath plus noise estimation approach is actually very simple, since many of the aspects involved in it were already discussed in other Chapters. In order to understand the derivation of the multipath plus noise (M+N) estimates, we should start with the simplified code measurement equations, similar to the ones used in Chapter 2 (Equations 2.3 and 2.4):

$$P_1 = R + c(dT - dt) + T + I + HD_{r,1} - HD_{s,1} + M_1 + E_1, \quad (5.1)$$

and

$$P_2 = R + c(dT - dt) + T + \gamma I + HD_{r,2} - HD_{s,2} + M_2 + E_2, \quad (5.2)$$

where all the elements of the equations above have been already described in Chapter 2. In this chapter we are interested in getting an estimate of the multipath and noise (i.e., other un-modeled errors) present in the equations above, i.e., $M_1 + E_1$ for P1 (or C/A) and $M_2 + E_2$ for P2. The equations of this chapter will show the un-modeled error term as E to maintain the consistency with other Chapters, even though I will refer to the combination of multipath and other errors as multipath plus noise (M+N) in the text. In order to isolate these elements, it is necessary to know all the others, i.e., receiver coordinates, satellite coordinates, receiver clock error, satellite clock error, neutral atmosphere delay, ionospheric delay, and receiver and satellite hardware delays. In the approach I am going to explore here, we separate these terms using the knowledge of most of the other elements in equations 5.1 and 5.2, which is achieved by using precise orbits and clocks. As an alternative to the knowledge of all these effects, they can be eliminated by means of a particular combination between code and phase measurements, such as the one shown by Langlely [1998]. The drawback of doing so is that a bias term is introduced in the equation. This is because the code measurements (P1 or P2) is combined with a particular phase combination (L1 and L2) in which the ionospheric

delay and the geometric effects are the same as in the code measurements (divergence-free phase combination), thus all terms can get eliminated, besides code and phase multipath, noise, hardware delays and phase ambiguity.

To introduce the derivation of multipath plus noise within the PPP package, we start considering the iono-free code combination:

$$P_{if} = R + c(dT - dt) + T + HD_{r,if} - HD_{s,if} + M_{if} + E_{if} , \quad (5.3)$$

where the first order ionospheric delay does not exist. Higher order terms of the ionospheric delay are part of E_{if} in this case. The big disadvantage of this observable, in the scope of this chapter, is that we are no longer able to distinguish between L1 and L2 multipath and noise. Another aspect of the equation above is that satellite hardware delays can be easily accounted for by using the same observable types as the ones used for the satellite clock generation (which is usually done using an iono-free combination too), or alternatively applying code bias corrections (as discussed in more detail in Chapter 4). If satellite code biases are adequately accounted for in a consistent manner for all satellites, the receiver hardware delay will consequently be absorbed by the receiver clock parameter (as discussed in Chapter 2). Therefore, assuming that satellite code biases are adequately handled, we can use a further simplified equation for the iono-free pseudorange:

$$P_{if} = R + c(dT - dt) + T + M_{if} + E_{if} , \quad (5.4)$$

where the hardware delay terms were dropped. The iono-free code multipath and noise observable can be easily derived from equation 5.4 rearranging it, as:

$$P_{if} - [R + c(dT - dt) + T] = M_{if} + E_{if} . \quad (5.5)$$

Looking at the equation above it is possible to notice that the multipath and noise estimate consists of the non-modeled effects on the PPP model. From this fact, it is possible to have an idea of what are the effects contributing for the “noise” estimate. Some of these are receiver noise, residual neutral atmosphere delay, residual satellite orbit and clock error, residual receiver clock error, residual code bias errors and so on. Some of these effects, such as residual clock errors, are very small (1-2 cm – if precise satellite clocks are used) if compared to the magnitude of the effects of interest in this case (i.e., code multipath at low elevation angles). However, in cases in which the satellite is at very high elevation angles, when the contribution of multipath is very small, these other previously mentioned sources of error might have a non-negligible contribution to the multipath and noise estimates. Another aspect which has to be taken into account is that we might have systematic components affecting the estimate of M+N due to some of the residual effects aforementioned. This is the case of the residual neutral atmosphere delay, which in PPP is modeled as a zenith delay parameter mapped to the slant direction using a mapping function (see Chapter 2). Error magnitudes which are reasonably small for the zenith delay parameter, might become significant factors when

mapped to low elevation angles (for more details on neutral atmosphere modeling please refer to Chapter 7), or in cases of an asymmetric atmosphere it might be not possible to reasonably model it using a zenith delay parameter plus a symmetric mapping function.

Another aspect that should be pointed out is that it might not be possible to provide reliable M+N estimates during the first several minutes (up to around 120 minutes depending on the case, according to my experience) of observation, because the PPP parameters used in Equation 5.5 might not have been converged to stable, precise values. This might be the case of receiver coordinates, receiver clock error, and zenith neutral atmosphere delay. Using a station with known position, and constraining this position before processing the data, considerably helps to reduce this convergence time, to a few minutes.

Figure 5.1 shows the iono-free code multipath plus noise (M+N) estimates for PRN 10, as observed at station UNBJ, on DOY 134 of 2007. The upper plot shows the M+N estimates, and the lower plot shows PRN 10 elevation angle.

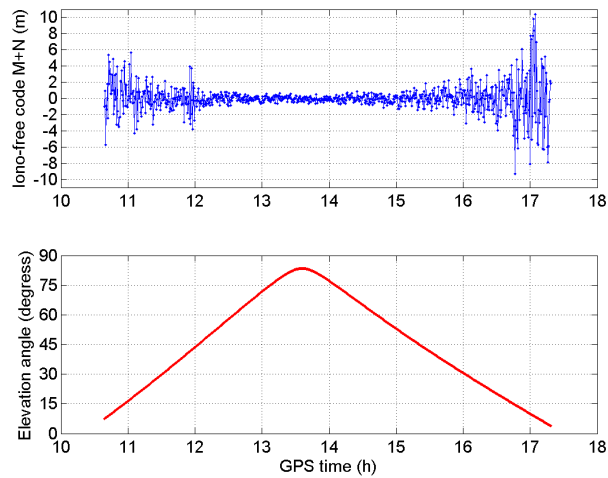


Figure 5.1. Iono-free code multipath plus noise estimates for PRN 10, station UNBJ.

It is possible to notice that, during this satellite pass, the noise level is less at high elevation angles, and more when the satellite is observed at lower elevations. If we look at different satellites for station UNBJ over one day, it is possible to understand how the noise level varies with respect to elevation angle and azimuth. Figure 5.2 shows the code M+N level (represented by color, in meters) for station UNBJ over 24h on DOY 134 of 2007. It is possible to notice that in this case the noise level varies mainly with respect to elevation angle. It is also possible to notice that depending on the azimuth, the signal starts to be tracked at lower or higher elevation angles (the data processing elevation angle mask was set to zero in this case). This is probably caused by obstacles that exist around the station at certain directions and prevent from a near zero elevation angle satellite view.

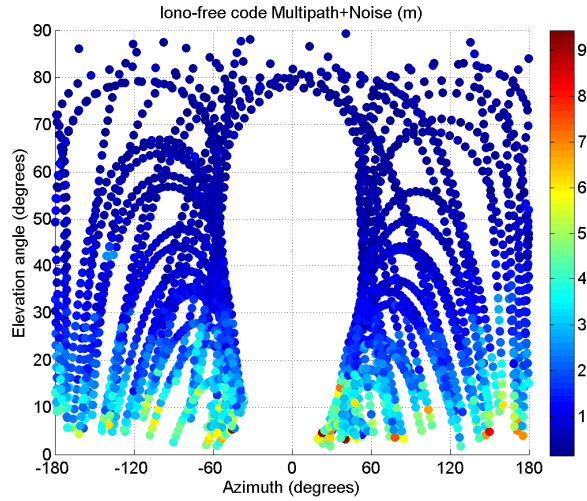


Figure 5.2. Iono-free code M+N for station UNBJ, on DOY 134 of 2007.

In Figure 5.3 we can see the variation of the iono-free code M+N with respect to elevation angle only. As already mentioned, the noise level is higher at lower elevation angles, as expected.

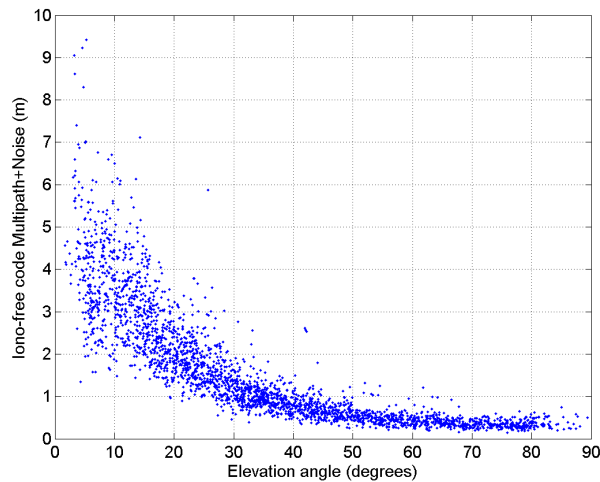


Figure 5.3. Iono-free code M+N with respect to elevation angle for station UNBJ, on DOY 134 of 2007.

Although using the iono-free code M+N estimate does not allow to assess measures of M+N for L1 and L2 frequencies separately, it provides an estimate which has very close relationship to the quality of the measurements used in PPP, since iono-free combination

is in general the preferred combination for stand-alone positioning. Later in this chapter I will discuss an application of iono-free code M+N estimates, for L2C signal analysis. Before that I will discuss the derivation of L1 and L2 M+N estimates in the next section.

5.2. L1 and L2 code multipath plus noise estimates

In this section we will explore the estimation of M+N values for the two frequencies separately, starting from the two simplified pseudorange equations (similar to (5.1) and (5.2)) below:

$$P_1 = R + c(dT - dt) + T + I + HD_{r,1} - HD_{s,1} + M_1 + E_1, \quad (5.6)$$

and

$$P_2 = R + c(dT - dt) + T + \gamma I + HD_{r,2} - HD_{s,2} + M_2 + E_2, \quad (5.7)$$

The idea of subtracting known effects from the pseudorange measurements is still the same, so we can rearrange L1 and L2 equations, similarly to what was done in (5.5):

$$P_1 - [R + c(dT - dt) + T] = HD_{r,1} - HD_{s,1} + M_1 + E_1 + I, \quad (5.8)$$

and

$$P_2 - [R + c(dT - dt) + T] = HD_{r,2} - HD_{s,2} + M_2 + E_2 + \gamma I . \quad (5.9)$$

As it can be noticed, there are still two types of effects present on the right-hand side of the equation, which are the ionospheric delay and hardware delay biases. The biases (hardware delays) are still present because we are using satellite and receiver clocks solution which are based on iono-free combination (the reason why they are gone in the iono-free estimation case). As it was explored in Chapter 3, GAPS has a built-in ionosphere estimation engine. This means that we can use the ionospheric delay estimated values into the code M+N estimation engine, since all of these engines are integrated inside GAPS. This allows us to further rearrange the equations above to:

$$P_1 - [R + c(dT - dt) + T + I] = HD_{r,1} - HD_{s,1} + M_1 + E_1 , \quad (5.10)$$

and

$$P_2 - [R + c(dT - dt) + T + \gamma I] = HD_{r,2} - HD_{s,2} + M_2 + E_2 . \quad (5.11)$$

The hardware delay biases are still present on the right-hand side of the equation. In order to handle them GAPS assumes they are stable over time, i.e., they are constant. Given this assumption it is possible to eliminate them from the M+N estimates by removing their mean values:

$$M'_1 + E'_1 = HD_{r,1} - HD_{s,1} + M_1 + E_1 - \text{mean}(HD_{r,1} - HD_{s,1} + M_1 + E_1), \quad (5.12)$$

and

$$M'_2 + E'_2 = HD_{r,2} - HD_{s,2} + M_2 + E_2 - \text{mean}(HD_{r,2} - HD_{s,2} + M_2 + E_2), \quad (5.13)$$

which implies that the estimates are related to the variation of the M+N around their mean:

$$M'_1 + E'_1 = M_1 + E_1 - \text{mean}(M_1 + E_1), \quad (5.14)$$

and

$$M'_2 + E'_2 = M_2 + E_2 - \text{mean}(M_2 + E_2), \quad (5.15)$$

under the assumption that the hardware delay biases are constant, i.e.:

$$HD_{r,1} - HD_{s,1} = \text{mean}(HD_{r,1} - HD_{s,1}), \quad (5.16)$$

and

$$HD_{r,2} - HD_{s,2} = \text{mean}(HD_{r,2} - HD_{s,2}). \quad (5.17)$$

Figure 5.4 shows the estimates of L1C and L2P(Y) code M+N (given by equations 5.12 and 5.13) for PRN10 as observed at station UNBJ, on DOY 134 of 2007.

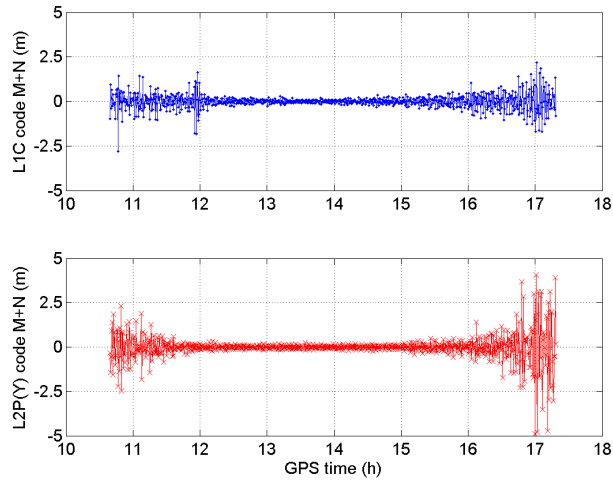


Figure 5.4. L1C and L2P(Y) code M+N for PRN10, station UNBJ, on DOY 134 of 2007.

As shown in Figure 5.4, the L2P(Y) code M+N values look to be in general higher than L1C ones, with the exception of a short period slightly before 12 h. The standard deviation for each code is 0.42 m and 0.71 m, for L1C and L2P(Y), respectively.

5.3. Comparison with TEQC

In order to have an idea on whether GAPS' M+N estimates are realistic, they will be compared to results from another piece of software: TEQC. TEQC software provides what it is referred to as MP1 and MP2 estimates. These estimates are done by removing geometric and ionospheric effects from code measurements making use of a particular

combination of dual-frequency carrier-phase. The result is the code multipath plus noise, added by carrier-phase multipath plus noise, ambiguities, and biases (e.g. hardware delays). The constant part (ambiguities and biases) are removed by reducing the estimates to a zero-mean process, in similar way as in equation 5.13. The technique used by TEQC is actually based on the same code and carrier combination described in Langley [1998], and a more detailed description of TEQC algorithm can be found in Estey and Merteens [1999]. Figure 5.5 shows MP1 and MP2 estimates provided by TEQC for the same data set used for Figure 5.4 (PRN10, station UNBJ, on DOY 134 of 2007).

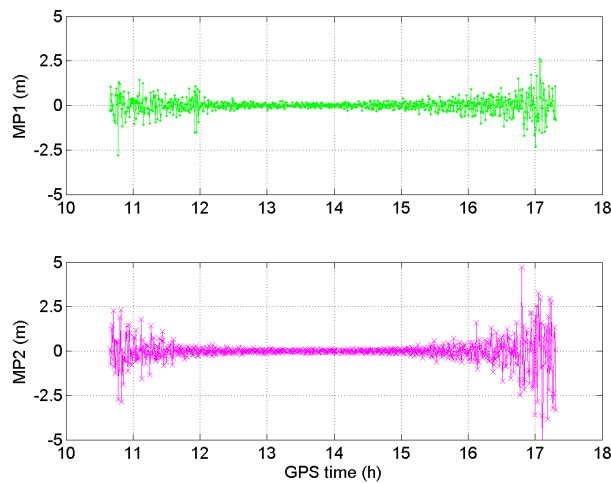


Figure 5.5. L1C (MP1) and L2P(Y) (MP2) code M+N estimates using TEQC, for PRN10, station UNBJ, on DOY 134 of 2007.

The standard deviation for L1C and L2P(Y) is 0.45 m and 0.70 m, respectively. These values are similar to the ones estimated with GAPS (0.42 m and 0.71 m, respectively). The results from GAPS and TEQC are different, as expected, because of what these two estimates represent are slightly different. While TEQC estimates are a measure of the code multipath plus noise, plus the divergence-free carrier-phase multipath plus noise,

GAPS estimates are a measure of code M+N plus un-modeled effects on the pseudorange. This means that with GAPS we are measuring a composite of the quality of the observation and of the observation model. Both techniques provide measures of code M+N, however, the definition of the noise component “N” is slightly different. Nevertheless, being multipath and receiver noise major contributions to these two types of estimation, the results are somehow similar. Figures 5.6 and 5.7 show a comparison between GAPS’ and TEQC’s M+N estimates (PRN10, station UNBJ, on DOY 134 of 2007), zooming in the middle of the satellite arc (with lower noise level) and in the beginning of the arc (higher noise level), respectively.

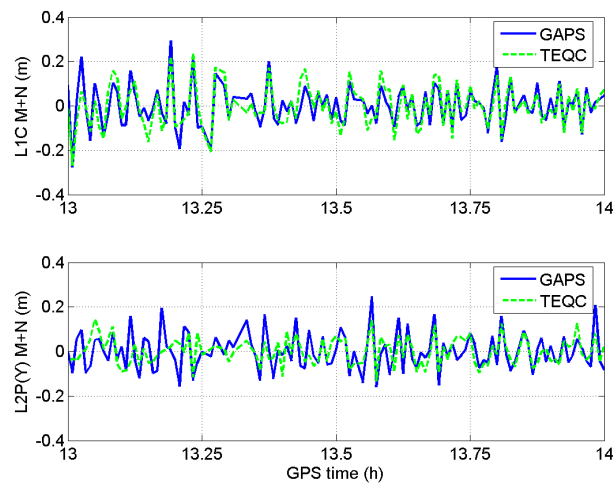


Figure 5.6. L1C (MP1) and L2P(Y) (MP2) code M+N estimates using TEQC, for PRN10, station UNBJ, on DOY 134 of 2007.

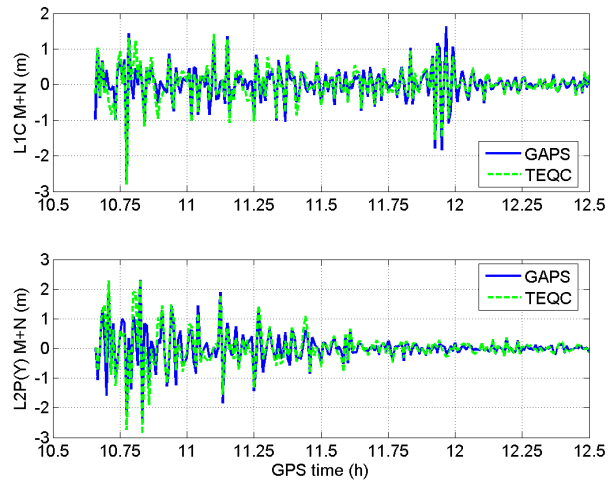


Figure 5.7. L1C (MP1) and L2P(Y) (MP2) code M+N estimates using TEQC, for PRN10, station UNBJ, on DOY 134 of 2007.

As it can be seen, although the values computed with the two different techniques are not exactly the same, the behavior of the M+N time series follows a similar pattern. In Table 5.1, we can see a comparison of the M+N values computed for each GPS satellite, as observed at UNBJ, on DOY 134 of 2007.

Table 5.1. Multipath plus noise values computed for each satellite observed by UNBJ station.

PRN	L1C M+N		L2P(Y) M+N		Maximum el. angle (degrees)
	GAPS (m)	TEQC (m)	GAPS (m)	TEQC (m)	
1	0.65	0.65	0.85	0.83	87
2	0.38	0.39	0.51	0.55	80
3	0.47	0.48	0.72	0.73	77
4	0.37	0.41	0.60	0.60	80
5	0.55	0.60	0.86	0.84	50
6	0.53	0.56	0.72	0.74	44
7	0.54	0.57	0.75	0.78	39
8	0.60	0.66	0.80	0.85	59
9	0.65	0.65	1.02	0.96	69
10	0.42	0.43	0.71	0.67	83
11	0.44	0.45	0.67	0.70	71
13	0.51	0.59	0.77	0.78	48
14	0.45	0.46	0.66	0.68	80
16	0.50	0.50	0.63	0.61	88
17	0.44	0.44	0.49	0.54	81
18	0.45	0.43	0.62	0.65	90
19	0.59	0.59	0.83	0.85	83
20	0.49	0.50	0.73	0.80	44
21	0.64	0.71	0.98	0.96	66
22	0.59	0.59	0.80	0.76	79
23	0.52	0.58	0.73	0.74	57
24	0.77	0.73	1.18	1.07	53
25	0.59	0.58	0.90	0.90	79
26	0.59	0.58	1.01	1.01	83
27	0.63	0.66	0.78	0.77	64
28	0.55	0.56	0.93	0.88	82
29	0.64	0.63	0.94	0.94	79
30	0.58	0.64	0.85	0.87	56
31	0.42	0.47	0.48	0.53	78
32	0.61	0.64	0.73	0.77	67
ALL	0.54	0.56	0.81	0.84	-

From the table above, it is possible to see that the M+N values computed for each satellite using GAPS and TEQC are quite similar with differences mostly at the cm-level. The overall (i.e., computed from data of all satellites) L1 and L2 values for UNBJ (represented by “ALL” in the table) are also similar. It is also possible to notice that the values provided by GAPS are systematically slightly lower than TEQC’s. This effect might be due to the fact that GAPS uses only observations which have passed on

previous quality control tests, such as outliers detection, and thus it unlikely uses 100% of the observations. The screened out observations are usually the ones with more unmodeled errors. In Figure 5.8, the histograms show the differences between values estimated with GAPS and TEQC for each satellite (in the sense of GAPS-TEQC). Please note that the vertical ranges are different for each plot.

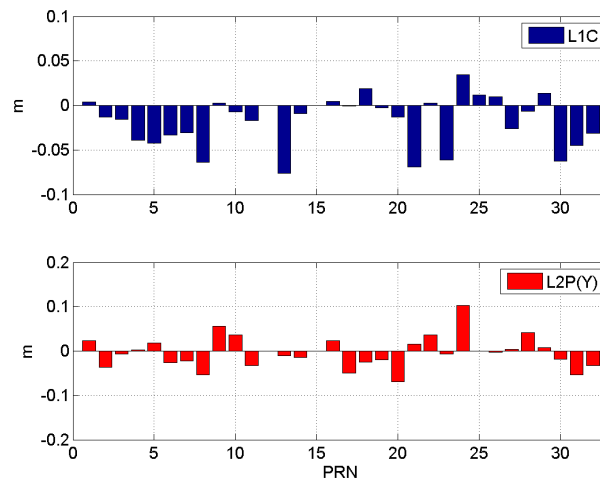


Figure 5.8. L1C (MP1) and L2P(Y) (MP2) code M+N estimate differences in the sense GAPS-TEQC for station UNBJ, on DOY 134 of 2007.

The RMS of the differences shown above is 3 cm, for both L1C and L2P(Y) codes, what leads us to the conclusion that, despite the differences between the two techniques, they provide measures of L1 and L2 multipath plus noise estimates with a consistency of better than 5 cm (when compared against each other) for this data set.

5.4. Analysis of L2C code quality

In this section, an investigation of the quality of the L2C code measurements is presented. Preliminary analyses in this area have been previously made, such as in Sükeová et al. [2007]. In this analysis I am working with the iono-free code M+N estimates, making a comparison between values estimated from the combined L1C and L2P(Y) codes, and the combined L1C and L2C codes. The dataset used in this section is from station UNB3, which uses a Trimble NetR5 receiver. The main reason for using that station is the fact that the NetR5 receiver has the advantage of tracking simultaneous L2C and L2P(Y) signals. This characteristic is fundamental for the analysis of the possible improvements brought by the use of L2C, since the legacy and modernized signals are observed under the exact same conditions. University of New Brunswick has even made data available containing simultaneous observations of carrier phase, code, and signal-to-noise ratio for the two signals. This was possible by using a specific in-house station setup, plus the capability of creating files in RINEX 3.0 format (in fact UNB3 was, to the best of my knowledge, the first station to have data available in that format) [Langley and Leandro, 2007].

As mentioned in Chapter 4, GAPS was modified in order to be capable of processing L2C data. The M+N computation equation for L2P(Y) is identical to equation 5.5, written as:

$$P_{if,L2P(Y)} - [R_{P2} + c(dt_{P2} - dt_{P2}) + T_{P2}] = M_{if,L2P(Y)} + E_{if,L2P(Y)} \cdot \quad (5.18)$$

However in case of the L2C-based measurements, the unknown L2C-related bias has to be considered. Because of this, (5.18) should be rewritten for the L2C case as:

$$P_{if,L2C} - [R_{C2} + c(dt_{C2} - dt_{C2}) + T_{C2}] = M_{if,L2C} + E_{if,L2C} + \beta \cdot B_{P2-C2}^{R-S}, \quad (5.19)$$

where B_{P2-C2}^{R-S} is the receiver-satellite differential P2-C2 code hardware delay (P2 and C2 are RINEX v2.11 nomenclature for L2P(Y) code and L2C code, respectively), and β is the L2 iono-free combination coefficient, where:

$$\beta = \frac{f_2^2}{f_1^2 - f_2^2}, \quad (5.20)$$

and, f_1 and f_2 are the L1 and L2 frequencies, respectively. In equations 5.18 and 5.19 the terms inside brackets have subscripts “P2” and “C2” to differentiate which kind of determination they come from.

As mentioned earlier, one of the effects which might be an object of concern for the unmodeled errors term (E) is the residual neutral atmosphere. It is important to have in mind that there are simultaneous measurements of (5.18) and (5.19), thus these observations are subject to the exact same conditions. Since we know that for high elevation angles there is very low impact of multipath and residual atmosphere, it is possible to use (5.18) and (5.19) above a certain elevation angle threshold (in this analysis I have neglected the first and last 10 minutes of data in each satellite pass – this time interval was determined

empirically for the particular data set which was used) to derive an estimate of the receiver-satellite bias combination, by combining equations 5.18 and 5.19:

$$\{P_{if,L2P(Y)} - [R_{P2} + c(dt_{P2} - dt_{P2}) + T_{P2}]\} - \{P_{if,L2C} - [R_{C2} + c(dt_{C2} - dt_{C2}) + T_{C2}]\} = \beta \cdot B_{P2-C2}^{R-S}, \quad (5.21)$$

or

$$(M_{if,L2C} + E_{if,L2C} + \beta \cdot B_{P2-C2}^{R-S}) - (M_{if,L2P(Y)} + E_{if,L2P(Y)}) = \beta \cdot B_{P2-C2}^{R-S}. \quad (5.22)$$

Figure 5.9 shows the values for $(M_{if,L2C} + E_{if,L2C} + \beta \cdot B_{P2-C2}^{R-S})$ and $(M_{if,L2P(Y)} + E_{if,L2P(Y)})$ for PRN 17 (Station UNB3, DOY 358 of 2007).

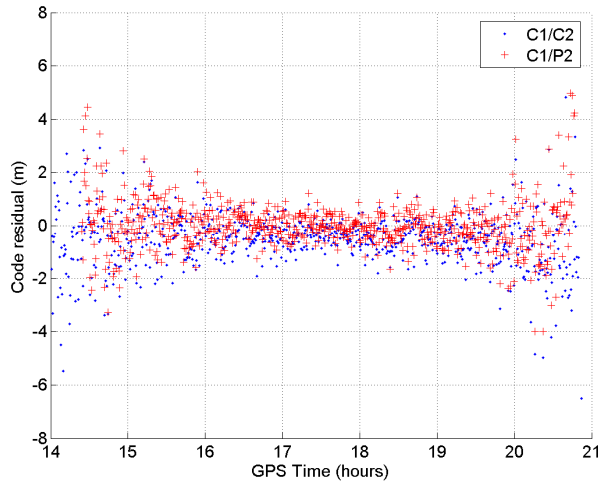


Figure 5.9. Code residuals for C2- and P2-based iono-free code observations.

Figure 5.10 shows the values computed for the bias combination $\beta \cdot B_{P2-C2}^{R-S}$, epoch by epoch (black) and the mean value (red line) computed for it (same data as Figure 5.9), which is around -41 cm for PRN 17.

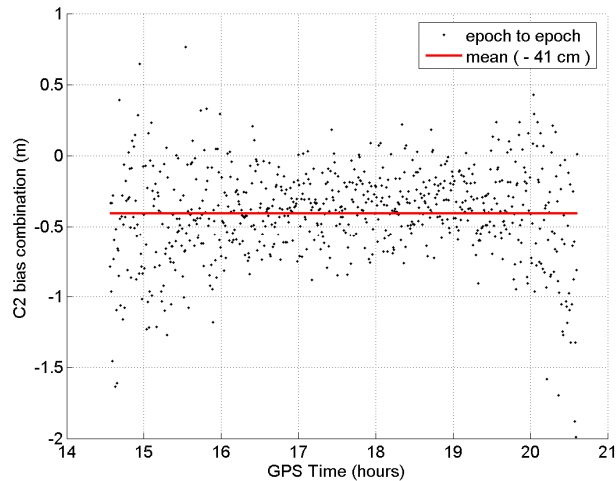


Figure 5.10. Receiver-satellite C2-P2 bias combination derivation.

After the receiver-satellite bias combination is accounted for, it is possible to compute the difference between the two code types in terms of un-modeled errors (which would be very similar to Figure 5.10, but shifted to have a zero-mean). Similarly, this comparison could also be made by means of the raw measurements. However, there is a major advantage in using GAPS M+N estimates rather than raw measurements. This is due to the fact that besides providing the magnitude of differences, the M+N estimates also allow us to determine which of the two code types is providing better results, since better measurements should provide smaller noise values. Other information, which can be derived only from these estimates, is the relative order of magnitude of the differences, with respect to the noise level itself, which tells us whether the differences are actually

negligible with respect to the noise or not. Figure 5.11 shows the two types (C2- and P2-based) of iono-free code M+N estimates for station UNB3, DOY 358 of 2007, with respect to elevation angle, for Block IIR-M satellites.

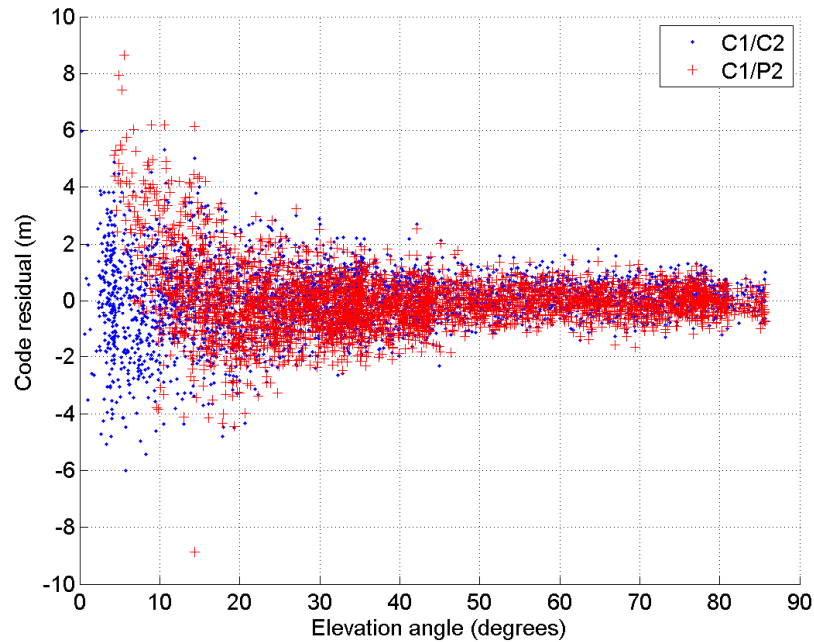


Figure 5.11. C2- and P2-based iono-free pseudorange residuals.

From the plot above, it is possible to see that, down to elevation angles of around 10 degrees, there is a very small difference between the spread of the residuals obtained using C2 or P2 codes. This means that, above 10 degrees, elevation angle both code types should provide results with a similar quality level. When we look at residuals at 10 degrees and below, it is clear that there are many more C2-based samples than P2-based samples. This is because L2C code typically can be tracked to lower elevation angles than L2P(Y) code. Besides that, the few samples of P2-based residuals below 10 degrees seem to have a somewhat worse quality than C2-based ones. This can be more clearly

seen in Figure 5.12, which shows the rms of the residuals of Figure 5.11 for each elevation angle bin (for every 10 degrees).

In Figure 5.12, it can be noticed that down to the 20-30 degrees bin there is virtually no difference between C1/P2 and C1/C2 residuals rms. There is a small difference for bin 10-20, of around 25 cm, and a big difference (about 1.5 m) in the rms for the 0-10 degrees bin.

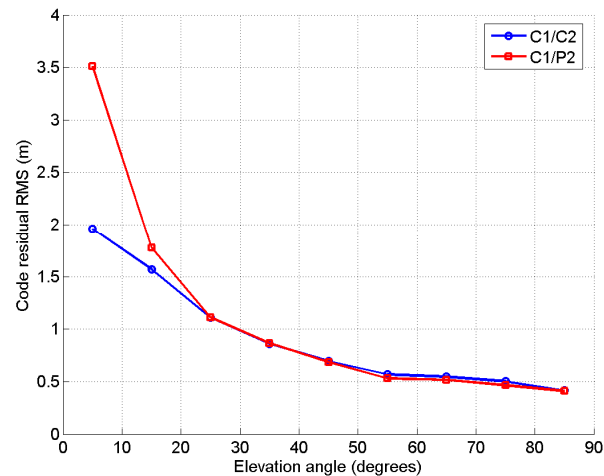


Figure 5.12. Rms of Figure 5.11 residuals for different elevation angle bins.

These plots lead us to the conclusion that for elevation angles above 10 degrees, the use of L2C does not bring any big advantage over the use of L2P(Y) code in terms of M+N level. It should be noted that this conclusion is valid only for situations when a reasonably clear sky is available. Surveys made in high multipath environments (such as under tree canopies or in urban areas) where there are potentially many losses of lock, might lead to different conclusions. Nevertheless, for lower elevation angles there is a

sensible difference in M+N level, as well as a larger number observations realized when L2C is used.

5.5. Chapter remarks

In this chapter I presented a technique to derive code multipath plus noise estimates using a PPP engine. These estimates can be derived from the iono-free code combination, as well as from observation on each individual frequency. The main difference between these two types of derivations (iono-free or frequency dependent) are that in case of single frequency (1) it is necessary to use a ionospheric model, such as the implemented in GAPS; and (2) differential code biases need to be accounted for.

In a comparison of GAPS' and TEQC's code M+N estimates for L1C and L2P(Y), an agreement of better than 5 cm was found, with estimates from GAPS being systematically slightly less than from TEQC. A potential reason for this is the fact that GAPS provides M+N estimates for the observations which were actually used in the PPP engine, and thus the data is already cleaned from high un-modeled effects (PPP-wise).

In an analysis of iono-free code M+N estimates using L2C and L2P(Y) measurements it was possible to arrive at the conclusion that even though L2C tracking is more robust than L2P(Y), the noise level of both signals tracked under the same conditions is about the same. Therefore we should expect that the major advantages of using L2C happen in

environments where satellite tracking is difficult, such as in urban areas and under canopies, which is a recommendation for future investigations.

6. Single-receiver satellite pseudo-clock estimation

In this chapter I will briefly discuss the possibility of estimating satellite pseudo-clock information from a single station and the usefulness of doing so. I will use the term “pseudo” for the PPP-derived satellite clocks because unlike satellite clocks estimated from networks, effects such as residual neutral atmosphere delay, multipath, residual orbit errors and others are strongly present in the data, since they cannot be mitigated or averaged out to a certain degree such as when station networks are used. The discussion will be carried out in terms of concepts, rather than results and validation procedures. The idea of estimating satellite-related information with a single reference station is not new, since it is the basis of relative GPS positioning techniques. The different aspect introduced here is to use a PPP engine to derive the satellite pseudo-clock, which can be used for positioning by another receiver. One advantage in estimating satellite clock information rather than directly using reference station data is clear: the same satellite clock values can be used for both carrier-phase and pseudorange measurements (in relative GPS, it would be necessary to have the two types of observations from the reference station to perform between-station differences for code and carrier). Therefore, using single-station derived pseudo-clocks might be advantageous in terms of communication and data-transfer bandwidth. Another interesting aspect is that the use of reference-station-derived pseudo-clocks for positioning is a procedure similar to relative GPS and therefore it might be an important key in allowing the integration of PPP and local-structure-based positioning techniques, as these different positioning technologies

develop and/or converge. The technique can be also used for continued clock generation in case of clock data outage, using one station. As mentioned earlier, one of the main effects present on these single station pseudo-clocks is the neutral atmosphere delay. This effect could be mitigated if a reliable source of a-priori delays could be used. This could be the case of using numerical weather models to feed the pseudo-clock generation. The pseudo-clock technique would then be reasonably more accurate, and could be used as part of more complex clock estimation processes.

6.1. Derivation of the satellite pseudo-clocks

The first aspect which should be mentioned here is that the main observation to be used in this estimation is the iono-free carrier-phase measurement, which can be represented in a simplified way as:

$$\Phi_{if} = R + c(dT - dt) + T + \lambda_{if} N'_{if} - c_{if} + m_{if} + e_{if} , \quad (6.1)$$

where all terms have already been described in Chapter 2. Since we are interested in the satellite clock, we might rearrange the equation as follows:

$$\Phi_{if} + c_{if} - R - T = c(dT - dt) + \lambda_{if} N'_{if} + m_{if} + e_{if} . \quad (6.2)$$

The equation above tells us that the carrier-phase observations are being corrected for effects such as body tide, satellite and receiver antenna phase center, phase wind-up, and

others (c_{if}) – all discussed in chapter 2. Also, the receiver and satellite positions are considered to be known (R) as well as the neutral atmosphere delay (T).

The neutral atmosphere delay is an object of concern, because it would be very difficult to compute a zenith delay parameter with a single receiver without having precise satellite clock information before hand (which, in this case, we do not have). In order to account for the neutral atmosphere delay, I will use the delays predicted using the UNB3m model (discussed in Chapter 7), which means we will have to consider that there is a residual neutral atmosphere delay effect on the estimated clocks. Satellite orbits are also not perfectly known and thus orbit residual errors will also be present in the estimated values. This is one of the drawbacks in estimating satellite clocks with a single receiver: the strong presence of residual effects that cannot be neglected, which is one of the reasons why I am calling these estimates “pseudo-clocks” rather than “clocks”.

Equation 6.3 shows the same terms as equation 6.2 joined by the explicit residual error terms for orbits (δR) and neutral atmosphere (δT), and with the subscript zero for orbits and neutral atmosphere delay to indicate they are approximate values:

$$\Phi_{if} + c_{if} - R_0 - T_0 = c(dT - dt) + \lambda_{if} N'_{if} + \delta R + \delta T + m_{if} + e_{if} . \quad (6.3)$$

There are still some terms which require some attention in equation 6.3. Carrier-phase multipath plus noise ($m_{if} + e_{if}$) is an effect which is not mitigated at all in the scope of this analysis, so they are fully present in the satellite pseudo-clock estimations. The receiver

clock term (ΔT), like the neutral atmosphere delay, cannot be accurately determined from the observations of a single station without the knowledge of precise satellite clocks. Therefore it is another term which will be present in the estimated satellite pseudo-clocks. In principle, this is not a problem because as long as this is an effect which equally affects all satellites, whenever this pseudo-clock solution is used for positioning this effect will be absorbed by the remote receiver clock parameter. Last, but not least, the ambiguity term (N'_{if}) is one more term which cannot really be determined during the pseudo-clock derivation process. This does not constitute a problem in using the pseudo-clocks for positioning with carrier-phase measurements since it would be absorbed by the carrier-phase ambiguity parameter. However, that would not work for pseudorange measurements, since they do not have ambiguity terms related to them. This means that in order to use the pseudo-clocks for pseudorange measurements, the ambiguities have to be somehow removed (not necessarily totally eliminated) from the estimates. If the ambiguities are not removed from the pseudo-clock estimates, there will be biases (different for each satellite) on the clocks of similar magnitude as values of the carrier-phase ambiguities themselves. These biases could be harmful for positioning since these quantities could reach values much higher than the uncertainty of the pseudorange measurements in the positioning filter.

One simple way to remove the carrier-phase ambiguities from the pseudo-clock estimates is using a combination of code and carrier to come up with an approximate value for the ambiguity, such as shown below:

$$\Phi_{if} - P_{if} = \lambda_{if} N'_{if} + m_{if} + e_{if} - M_{if} - E_{if} . \quad (6.4)$$

This equation can be used for estimating an approximate value for the ambiguity, though infected by carrier-phase, code multipath and other errors. Some of these errors might be mitigated by creating an estimate based on observations made over given periods of time up to a complete satellite pass. However using complete satellite passes would be feasible only for post-processing applications. It is important that this approximate ambiguity does not change over time; otherwise, it will not be absorbed by the ambiguity parameter at the remote positioning site. Assuming we have an ambiguity approximation (given by equation 6.4) to be used, we can re-write equation 6.3 as:

$$\Phi_{if} + c_{if} - R_0 - T_0 - \lambda_{if} N'_{if,0} = c(dT - dt) + \lambda_{if} \delta N'_{if} + \delta R + \delta T + m_{if} + e_{if} , \quad (6.5)$$

where we can see on the right-hand side all components of the estimated satellite pseudo-clock values. Note that like the geometric distance and neutral atmosphere, the approximate ambiguity term has the subscript zero, and the right hand side of the equation has the residual ambiguity term ($\delta N'_{if}$). In next section I show an example of the generation and use of pseudo-clocks.

6.2. An example of generation and use of satellite pseudo-clocks

In this section, I show a practical example of the procedure which was explained above.

In this example, I am using IGS stations UNBJ and SHE2, both of them located in eastern Canada, as shown in Figure 6.1. SHE2 is located in Shediac, New Brunswick.

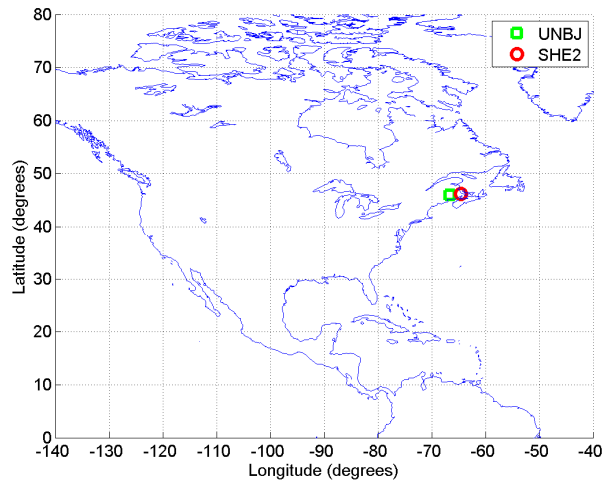


Figure 6.1. Stations UNBJ and SHE2.

The distance between these two stations is approximately 164 km. In this analysis, I used 24 hours of data observed on DOY 001 of 2008. The procedure consists of generating the satellite pseudo-clock values from SHE2 data, outputting them in RINEX clock file format [Ray, 2006], and then using this file for positioning using UNBJ data. In this particular case, the clock file header format is not strictly followed because some of the header records do not apply. Figure 6.2 shows a facsimile of the beginning of the file created from SHE2 data.

```

3.00          C          G          RINEX VERSION / TYPE
GAPS          Rodrigo Leandro 20080303 1200 UTC PGM / RUN BY / DATE
SHE2                                     ANALYSIS CLK REF
14                                                    LEAP SECONDS
1 AS                                                # / TYPES OF DATA
32                                                # OF SOLN SATS
G01 G02 G03 G04 G05 G06 G07 G08 G09 G10 G11 G12 G13 G14 G15 PRN LIST
G16 G17 G18 G19 G20 G21 G22 G23 G24 G25 G26 G27 G28 G29 G30 PRN LIST
G31 G32                                               PRN LIST
G                                                    SYS / PCVS APPLIED
          igs05_1455.atx                               END OF HEADER
AS G06 2008 01 01 00 00 30.000000 1 1.70151294825e-004
AS G24 2008 01 01 00 00 30.000000 1 5.86723915990e-005
AS G18 2008 01 01 00 00 30.000000 1 -2.15395453308e-004
AS G26 2008 01 01 00 00 30.000000 1 1.42478567684e-004
AS G21 2008 01 01 00 00 30.000000 1 7.44246769736e-005
AS G15 2008 01 01 00 00 30.000000 1 -7.06894766192e-005
AS G10 2008 01 01 00 00 30.000000 1 -1.91899498775e-004
AS G08 2008 01 01 00 00 30.000000 1 -1.3539539134e-004
AS G06 2008 01 01 00 00 60.000000 1 1.70152187638e-004
AS G24 2008 01 01 00 00 60.000000 1 5.86739283315e-005
AS G18 2008 01 01 00 00 60.000000 1 -2.15394012881e-004
AS G26 2008 01 01 00 00 60.000000 1 1.42480233898e-004
AS G21 2008 01 01 00 00 60.000000 1 7.44260169509e-005
AS G15 2008 01 01 00 00 60.000000 1 -7.06881474682e-005
AS G10 2008 01 01 00 00 60.000000 1 -1.91898881808e-004
AS G08 2008 01 01 00 00 60.000000 1 -1.35395025192e-004
AS G06 2008 01 01 00 01 30.000000 1 1.70152230390e-004
AS G24 2008 01 01 00 01 30.000000 1 5.86744371028e-005
AS G18 2008 01 01 00 01 30.000000 1 -2.15393402399e-004
AS G26 2008 01 01 00 01 30.000000 1 1.42481085596e-004
AS G21 2008 01 01 00 01 30.000000 1 7.44264091535e-005

```

Figure 6.2. Pseudo-clock file created from SHE2 data.

When looking at the file segment above, a very probable question which rises in our minds is how similar these numbers are to the IGS satellite clock solution. In fact, they are not supposed to be similar, given the already mentioned effects included in the pseudo-clocks. As an example, Figure 6.3 shows a comparison between GAPS pseudo-clock solution based on SHE2, and the IGS clock solution (for the same day, from file igs14602.clk_30s). The comparison shown here was done for PRN24 and PRN18, between 0 h and 2 h of DOY 001. It is quite obvious that the clock solutions are reasonably different between GAPS and IGS. However, one should notice that the behavior of the differences between the GAPS and IGS for each satellite is somehow similar. This is because a big chunk of the difference comes from the reference clock used: in the case of GAPS, SHE2's clock; and in case of IGS, the reference is a combination of NRC1, BRUS, ALGO, NISU, and USN3 clocks (all of them using hydrogen maser frequency standards when the data was observed for the generation of the IGS clock file) which is also aligned to GPS Time using the satellite broadcast

ephemeris (all this information can be found in the clock file itself and the station log files).

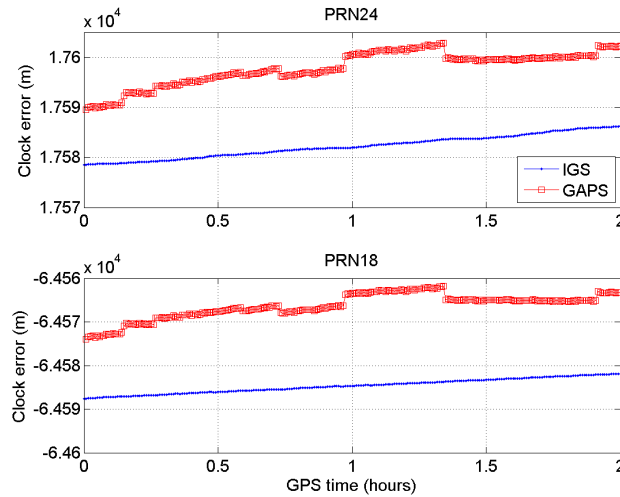


Figure 6.3. Comparison between GAPS satellite pseudo-clock solution and IGS clock solution.

In PPP, the meaningful information related to clocks is not the un-differenced clock value for each satellite, but the between-satellite differenced clocks. This is because the receiver clock error parameter will absorb any time offset which is common for all satellites. For carrier-phase measurements for which float ambiguities are being estimated, the relevant information is the double differenced clock, being the two differences between satellites, and between time (this means the relevant information for float ambiguities carrier-phase is the behavior of each clock over time). This is because the float ambiguity parameter will absorb any bias for each satellite. That said, a better way to compare the clocks shown in Figure 6.3 is by eliminating the influence of the reference clock on them, and this can be achieved by differencing the solution between two satellites. This way we can get the differential clock solution between PRN24 and

PRN18 (in the sense 24 - 18) for GAPS and IGS, as shown in Figure 6.4, where the two solutions were offset by the same amount (82163 m) to allow a better visualization of the vertical scale.

Analyzing shape of the two lines in Figure 6.4, it is possible to notice that the two solutions have a much more similar behavior now, although there is still a difference of about 2.5 m between them. The major source of this difference is probably the inability of coming up with correct values for the approximated carrier-phase ambiguities, as discussed earlier. Nevertheless, as long as an effect is constant over time, it will be absorbed by the carrier-phase ambiguity parameter in the PPP filter using the pseudo-clocks for positioning. That said, it is interesting to analyze whether the differences shown in Figure 6.4 are really constant over time. In order to visualize this, Figure 6.5 shows the same values as in Figure 6.4, but with constant offsets (the arithmetic mean of each time series) removed.

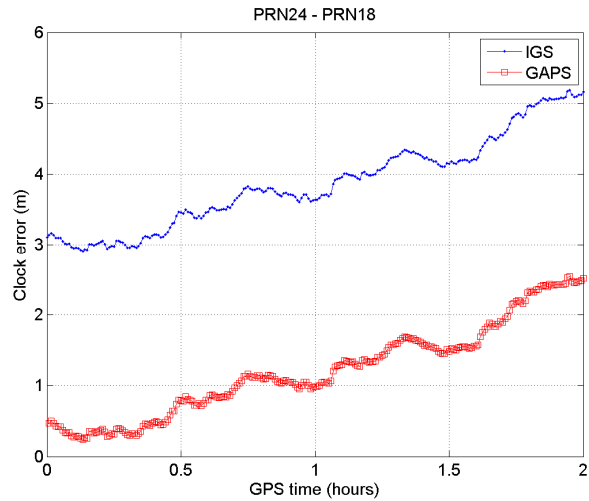


Figure 6.4. Comparison of between-satellite clock differences of GAPS satellite pseudo-clock solution and IGS clock solution.

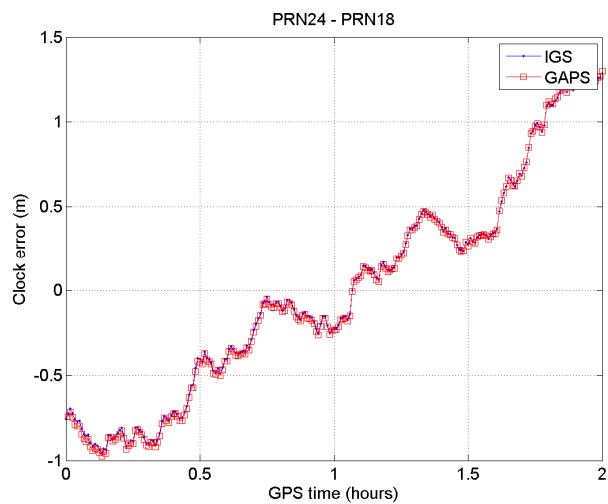


Figure 6.5. Comparison of between-satellite clock differences of GAPS satellite pseudo-clock solution for IGS clock solution (arithmetic mean of each time series removed).

In Figure 6.5, the similarity between the two clock solutions is quite noticeable. Because it is hard to take an estimate of the level of agreement from this plot, Figure 6.6. shows a plot of the difference between these two time series.

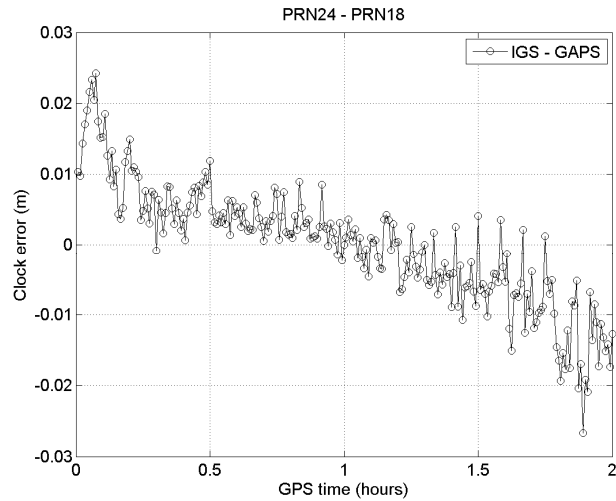


Figure 6.6. Comparison between GAPS satellite pseudo-clock solution and IGS clock solution.

Figure 6.6 is quite interesting because it shows two aspects of the pseudo-clocks estimation procedure. The first one is the fact that there is a reasonable agreement in terms of behavior between the two solutions (in fact, the rms of these differences is around 9 mm). We should use the term “relative behavior”, since we have removed offsets from the solutions and therefore we are no longer comparing the absolute values of the clocks, but simply how they behave over time. Anyway, as pointed out before the relative behavior over time is the most important aspect of a satellite clock when used for carrier-phase measurements in float-ambiguity-based PPP. However (and this is the second aspect), it is clear that there are systematic effects present in the pseudo-clock estimates, and these can include any one of the last four terms on the right-hand side of equation 6.5, the residual neutral atmosphere delay likely being the one with the most impact. Another aspect that could be pointed out is the fact that the pseudo-clocks as computed here are purely based on carrier-phase measurements, where the clocks were simply offset by an approximate constant derived from pseudoranges. Precise clocks such

as IGS ones are usually computed using carrier-phase and pseudorange measurements in parallel, under the assumption that the clock behavior is the same for both. This assumption has been contradicted in some publications such as in [Collins, 2008].

The next step after generating the pseudo-clock file is using it for positioning. In this analysis, I am using the pseudo-clock file generated from SHE2 data for processing UNBJ station data (in PPP positioning mode). I did the same analysis using the IGS clock file (igs14602.clk_30s) and used it as a benchmark. For analyses shown here, the reference coordinates are the ones which were obtained from a 24 hour static data processing using the IGS precise clock file. All the data processing options were identical between the two solutions. The only difference is the clock file which was used, which means that the pseudo-clocks are used just like they were precise satellite clocks. And this is the beauty of the whole idea, because we are feeding a PPP engine with locally based information rather than global-network-based information, without having to change anything in the data processing procedure. Figure 6.7 shows the horizontal error convergence obtained from a PPP run in static mode. In static mode, the receiver antenna is considered to be fixed and therefore a single set of coordinates is computed for the whole observation period. What the plot actually shows is how these coordinates converge to their final values over time.

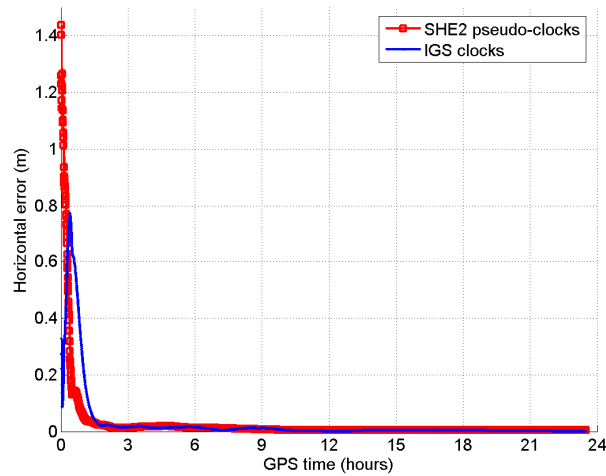


Figure 6.7. Horizontal error convergence from a PPP static run using IGS clocks, and SHE2 pseudo-clocks.

As can be seen, the final coordinates using the two different clock products converge to very similar final values, even only a few hours after the start of the observations. The (horizontal) difference between the two solutions at the end of the 24 h period is around 5 mm. It is also possible to notice that at the beginning of the time period, the convergence performance using the pseudo-clocks looks to be a bit better than using IGS clocks. This can be seen in Figure 6.8 where only the first two hours are shown.

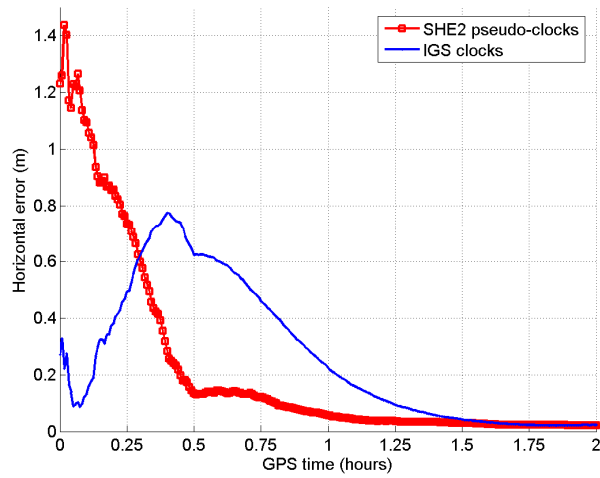


Figure 6.8. First two hours of horizontal error convergence from a PPP static run using IGS clocks and SHE2 pseudo-clocks.

Similar to Figures 6.7 and 6.8, Figures 6.9 and 6.10 show the convergence of the height component, for the same runs.

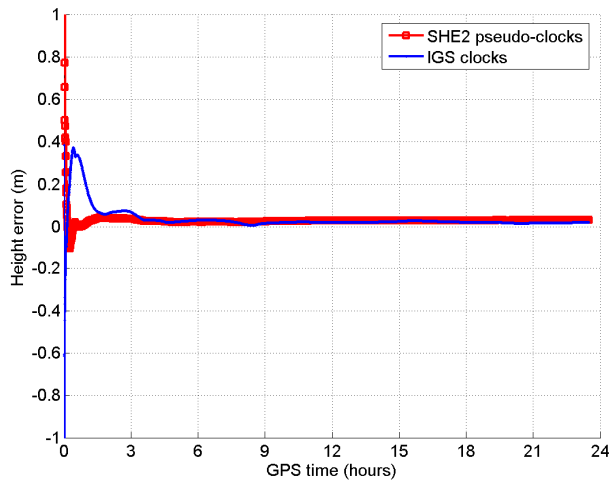


Figure 6.9. Height error convergence from a PPP static run using IGS clocks and SHE2 pseudo-clocks.

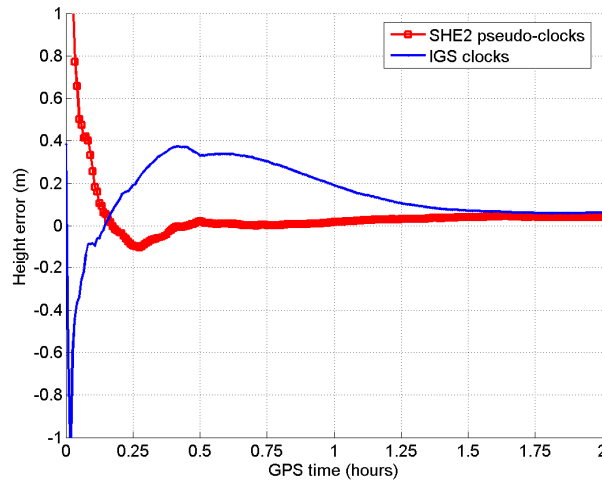


Figure 6.10. First two hours of height error convergence from a PPP static run using IGS clocks and SHE2 pseudo-clocks.

We can see that the height component results present similar characteristics as for the horizontal results, with very similar final values. The vertical difference between the two solutions was about 3 cm, and with the pseudo-clocks solution showing better convergence performance. The fact that the use of pseudo-clocks provided a better solution than the use of IGS clocks in certain aspects for this data processing, such as convergence time, should not come as a surprise. This is because even though the pseudo-clocks are infected by residual errors, some of these errors are highly correlated with errors obtained at the positioning station, and therefore get eliminated to a certain extent. This would be the case of the residual orbit errors, represented by the term δR in equation 6.5. The residual neutral atmosphere errors also get partially modeled as part of the positioning engine zenith neutral atmosphere delay parameter. Figure 6.11 shows the horizontal errors for a kinematic (epoch-by-epoch) run using the two clock types. In this case, the receiver antenna is not assumed to be fixed, and therefore one set of coordinates is computed for every observation epoch.

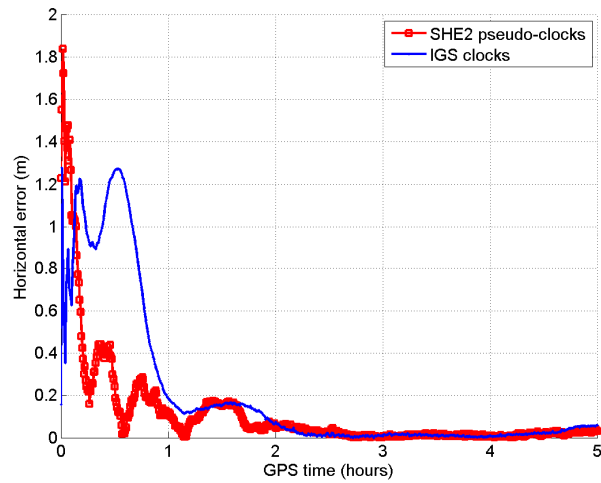


Figure 6.11. Horizontal error convergence from a PPP kinematic run using IGS clocks and SHE2 pseudo-clocks.

In the kinematic runs the use of pseudo-clock solution also provided a shorter convergence time and the final accuracies obtained after convergence are again comparable for the two clock solutions (statistics are shown in Table 6.1). This can be seen more clearly in Figure 6.12, which has a different scale for the vertical axis. Figure 6.13 shows the respective results for the height component.

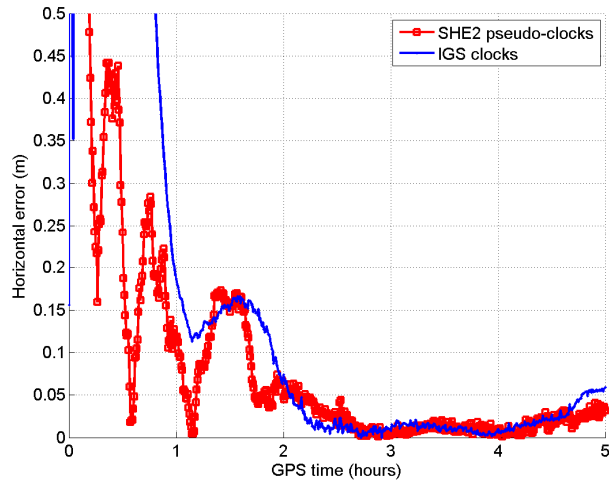


Figure 6.12. First two hours of horizontal error convergence from a PPP kinematic run using IGS clocks, and SHE2 pseudo-clocks.

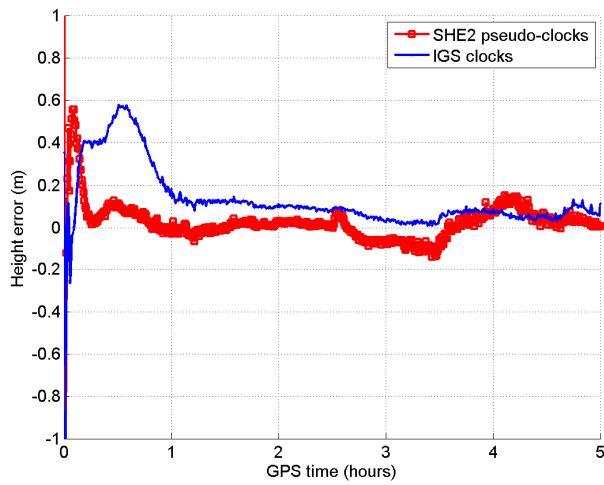


Figure 6.13. Height error convergence of a PPP kinematic run using IGS clocks, and SHE2 pseudo-clocks.

Table 6.1 shows the RMS values for the two clock solutions for the horizontal and vertical components. These values are in cm and were computed considering only the results obtained between 2 h and 5 h GPS Time.

Table 6.1. Kinematic PPP run RMS values (cm).

	SHE2 pseudo-clocks	IGS clocks
Horizontal	2.29	2.44
Vertical	6.43	7.07

It can be seen that the RMS values obtained from the two different clock solutions are comparable, with the ones provided from the pseudo-clocks being slightly better than the ones from IGS clocks.

6.3. Chapter remarks

In this chapter, I described a technique for estimating satellite clock information using data from a single receiver. This clock information is usually infected by residual (unmodeled) errors and, because of that, I have called it pseudo-clock information. The generation of pseudo-clocks is not too different from using a reference station in relative GPS positioning, but it has the advantage of allowing generating a relative positioning solution using a PPP engine, and using one single type of support data (pseudo-clock) which is useful for both carrier-phase and pseudorange measurements. This is a concept which might be quite useful in order to integrate global-network-based PPP with locally based relative GPS, since it was shown that it is possible to use either global network derived clocks (IGS clocks in this case) or local structure derived clocks (pseudo-clocks) with no changes in the positioning processor, with comparable accuracies.

In an application example, I have shown the use of pseudo-clocks estimated with data from station SHE2 for PPP with UNBJ data. In this analysis, the solution using the pseudo-clocks was shown to provide a shorter convergence time than when using IGS clocks, and both solutions provided comparable final accuracies.

7. Neutral Atmosphere prediction models for GNSS positioning

In this chapter I discuss developments related to neutral atmosphere delay prediction models. I will also introduce a new model, which was designed to provide better predictions for different regions inside a delimited wide area. The goal of this new development is to have a more reliable model for wide area augmentation system users, with some homogeneity in terms of performance over the area of interest. The approach to create the new wide area neutral atmosphere model for North America (UNBw.na) is comprehensively described and discussed. All result analyses took into consideration the most recent version of UNB models, until now, UNB3m [Leandro et al., 2006]. Results for meteorological parameters prediction showed that the new grid-based model could perform better than a latitude (only) based model (such as UNB3m). The general results do not show a spectacular improvement for the new model when looking at overall statistics, however it is consistently better than its predecessor, and the improvement for certain regions is more significant than others. Regions where the performance of the old model was not satisfactory had results significantly improved with the new model. A validation of UNBw.na predicted zenith delays was realized using radiosonde-derived delays as reference. This analysis showed that different regions of the continent manifested improvement for the estimations with the new model. Investigation of the performance of both models (UNBw.na and UNB3m) with radiosonde ray-traced delays at a few sample stations showed that UNBw.na generally has a better fit to the annual behavior of the zenith delays. It was also possible to notice that results from UNBw.na

are more consistent between stations at different locations than when using UNB3m. UNBw.na was shown to be consistently better than UNB3m in several aspects, and the adopted procedure for the grid calibration works in an adequate way, resulting in a reliable model.

7.1. Introduction

The neutral atmosphere delay (commonly referred to as tropospheric delay) is suffered by a GPS signal when it travels through the neutral atmosphere, on its way between satellite and receiver. Because of the nature of the neutral atmosphere, which is composed mainly of gases including water vapor, the signal gets refracted, which means its speed changes (the signal travels slower than the vacuum speed of light) as does its path (the signal doesn't travel in a straight line between satellite and receiver antennas). Due to these changes in speed and direction, it takes more time for the signal to reach the receiver's antenna than if it was traveling through a vacuum. This difference of time, which can also be represented in metric units, is the neutral atmosphere delay. The magnitude of this delay depends on several factors, and can be quantified based on the profiles of total atmospheric pressure, temperature, and the partial pressure of water vapor. The variation of these quantities at a particular location drives the variation of the delay from one day to another, over the different climate seasons. The most difficult quantity to predict is the amount of water in the atmosphere, due to its high variability, if compared to pressure or temperature. Another aspect which plays a fundamental role on how much delay the signal will experience is the amount of atmosphere it has to go through, which depends

basically on the elevation angle of the satellite with respect to the receiver. The closer the satellite is to the receiver's zenith, the less delay its signal will experience.

Zenith neutral atmosphere delays can be derived from prediction models such as UNB3m, which uses the Saastamoinen zenith delays, Niell mapping functions [Niell, 1996], and a look-up table with annual mean and amplitude for temperature, pressure, and water vapour pressure varying with respect to latitude and height. An extensive discussion of neutral atmosphere propagation delay modeling and testing can be found in Mendes [1999].

In the zenith direction, the neutral atmosphere delay at sea level is around 7.7 nanoseconds, or 2.3 meters, and it can get to more than 20 meters for elevation angles of around 5 degrees, and more than 10 meters at 10 degrees, as can be seen in Figure 7.1. Values in Figure 7.1 will be the approximate errors introduced into processed GPS observations in the case when neutral atmosphere delays are not accounted for. Given the level of these errors, it can be stated that neutral atmosphere delays have to be taken into account in GPS single receiver applications, no matter the level of accuracy which is being aimed at. This is, to a certain extent, also valid for differential positioning, mainly for long baselines.

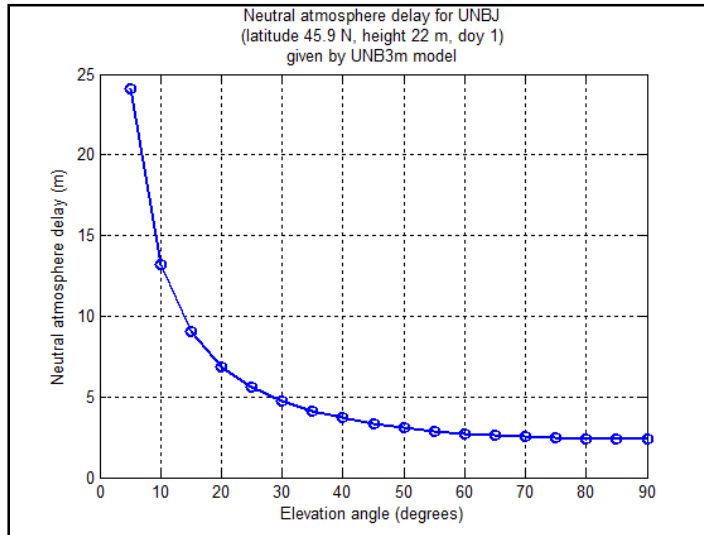


Figure 7.1. Neutral atmosphere delay as given by UNB3m prediction model and Niell mapping function.

The way neutral atmosphere delays can be handled may vary, depending on several aspects, such as type of observations being used, observation time and targeted accuracy. One way to account for these delays in GPS observations is by using prediction models, which don't require other sources of information and can provide the delays in real time, computed using an internal database. These prediction models usually have a 1-sigma uncertainty of 4-5 centimeters at zenith, which corresponds to 22-28 centimeters at 10 degrees elevation angle [Leandro et al. 2006]. This solution is good enough for most navigation applications nowadays, but future improved navigation techniques may require more accurate solutions. However, even today some positioning applications need higher accuracies than those provided by predictions, and for those applications there is an alternative, which is estimating the neutral atmosphere delay as a parameter in the data processing as done by GAPS. The drawback of this technique is that it might take time to achieve the convergence of this parameter depending on the quantity and distribution of the observed satellites, and dual-frequency code and carrier-phase observations must be

used, in order to get a reliable delay value. However, when these requirements are met, GPS-derived neutral atmosphere delays can be very reliable, and because of that GPS is being used as a sensor of the atmosphere for weather forecasting and climatology studies.

In order to analyze the impact of neutral atmosphere delays on GPS positioning, let's take a look at an experiment, where 12 hours of GPS data from IGS station UNBJ was processed in kinematic mode with GAPS and the results were compared with the known coordinates of the station. Three solutions were generated: (a) not accounting for the neutral atmosphere – no corrections were applied; (b) accounting for the neutral atmosphere using the UNB3m prediction model; and (c) accounting for the neutral atmosphere estimating the delay as a random walk parameter. The table below shows the bias (mean error) and rms values for each position component (north, east, and up) of the three cases, in meters (results are also shown in Figure 7.2):

Table 7.1. GAPS-PPP results from processing UNBJ data with variations on how the neutral atmosphere is handled.

	RMS (m)			Bias (m)		
	East	North	Up	East	North	Up
(a)	2.23	3.22	7.29	-0.41	1.32	4.39
(b)	0.06	0.08	0.17	-0.01	0.03	-0.15
(c)	0.05	0.06	0.12	-0.02	0.03	-0.01

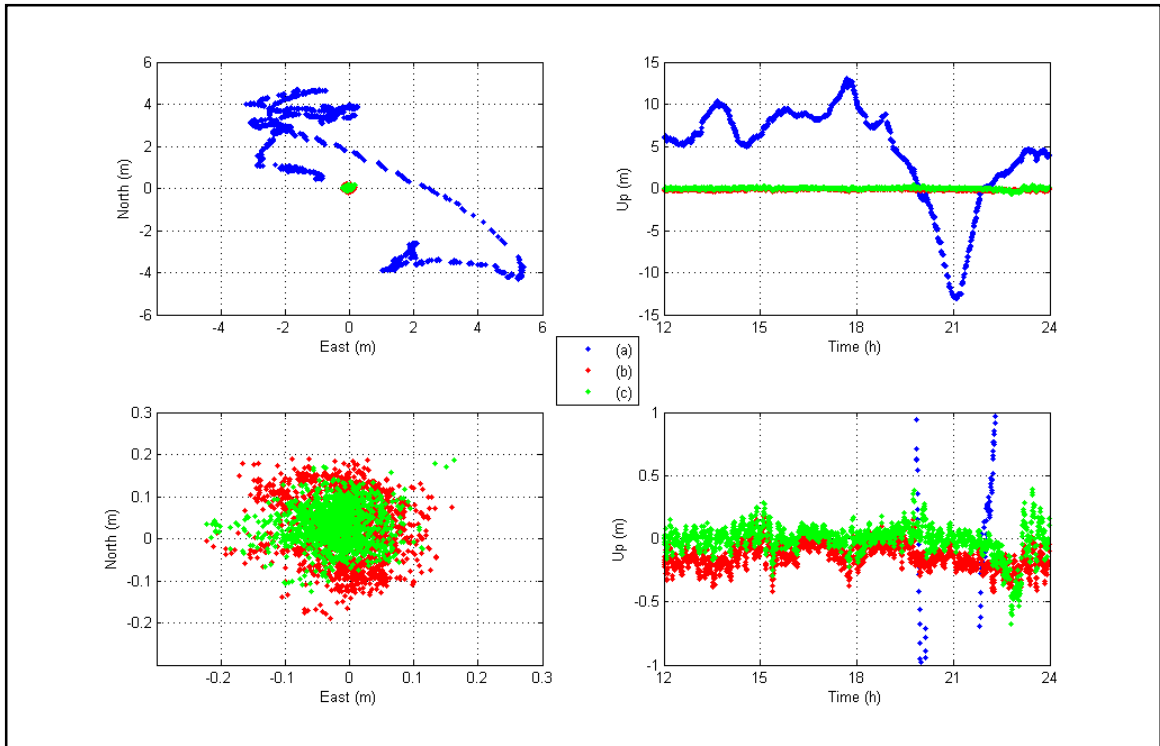


Figure 7.2. GAPS-PPP results from processing UNBJ data with variations on how the neutral atmosphere is handled.

We can see that solutions (b) and (c) are several orders of magnitude better than (a), in which delays were not corrected for. Note that even using 12 hours of data, mean horizontal position errors of several meters remain. Also, estimating neutral atmosphere delay as a parameter (c) provides better results than using a prediction model (b) for this dataset, with 1-5 centimeters improvement in the rms of each component, and with a significant improvement of 14 centimeters in height bias. On this particular day, UNB3m delay prediction was around 5 centimeters larger than the real delay value, as given by GAPS. From that we can see that the impact of neutral atmosphere delay mis-modeling on the height component is around three times larger than the error in the actual delay prediction. The large effect on height occurs because neutral atmosphere delays are highly correlated with the height component of the receiver position. Horizontal biases

for (b) and (c) are similar because of the variation of satellite geometry over time, which makes the average of the horizontal biases tend to zero (and this is only valid for relatively small residual neutral atmosphere delay errors – one can notice that the biases did not average out in (a)).

The improvement in the bias of the height component shows how important is having a reliable prediction model which can provide reasonable delay values. This importance is even higher if one considers that this is a significant milestone in order to allow PPP applications to provide results as reliable, as fast, and as accurate as solutions such as those provided by differential real-time kinematic applications.

In cases where the neutral atmosphere delay is being estimated as one of the parameters in GNSS positioning, this parameter is commonly a residual delay, to correct the initially predicted delay, which means that a prediction model is needed anyway. In most GNSS applications the prediction of the neutral atmosphere delay is required, even if only for an initial value for which a residual delay is computed. In this case having a very high level of accuracy for the prediction is usually not required.

As mentioned earlier, in this chapter I discuss developments related to neutral atmosphere delay prediction models at UNB. A number of UNB models have been developed over the past decade. Our latest global model version is called UNB3m, and a comprehensive description of it can be found in Leandro et al. [2006].

UNB neutral atmosphere models have their algorithm based on the prediction of surface meteorological parameter values, which are used to compute hydrostatic and non-hydrostatic zenith delays using the Saastamoinen models. The slant delays are determined applying the Niell mapping functions [Niell, 1996] to the zenith delays.

In order to account for the seasonal and regional variation of the neutral atmosphere behavior, meteorological parameters (barometric pressure, temperature, relative humidity, temperature lapse rate (β) and water vapour pressure height factor (λ)) are used as functions of time (day of year) and position in UNB models. Each meteorological parameter is modeled with two components: the average (mean) and amplitude of a cosine function with one year period. By definition, the origin of the yearly variation is day of year 28. This procedure is similar to the one used in the Niell mapping functions computation.

After average and amplitude of a given meteorological parameter are determined, the parameter value is estimated for the desired day of year according to:

$$X_{\text{doy}} = \text{Avg} - \text{Amp} \cdot \cos\left(\left(\text{doy} - 28\right) \frac{2\pi}{365.25}\right), \quad (7.1)$$

where X_{doy} represents the computed parameter value for day of year (doy), and Avg and Amp are the average and amplitude values respectively. This procedure is followed for each of the previously mentioned five parameters.

Once all parameters are determined for a given position and day of year, the zenith delays are computed according to:

$$d_h^z = \frac{10^{-6} k_1 R}{g_m} \cdot P_0 \cdot \left(1 - \frac{\beta H}{T_0}\right)^{\frac{g}{R\beta}}, \quad (7.2)$$

and

$$d_{nh}^z = \frac{10^{-6} (T_m k_2' + k_3) R}{g_m \lambda' - \beta R} \cdot \frac{e_0}{T_0} \cdot \left(1 - \frac{\beta H}{T_0}\right)^{\frac{\lambda' g}{R\beta} - 1}, \quad (7.3)$$

where

- d_h^z and d_{nh}^z are the hydrostatic and non-hydrostatic zenith delays, respectively;
- T_0 , P_0 , e_0 , β , and λ are the meteorological parameters computed according to (7.1);
- H is the orthometric height in meters;
- R is the gas constant for dry air ($287.054 \text{ J kg}^{-1} \text{ K}^{-1}$);
- g_m is the acceleration of gravity at the atmospheric column centroid in m s^{-2} and can be computed from

$$g_m = 9.784 \left(1 - 2.66 \times 10^{-3} \cos(2\phi) - 2.8 \times 10^{-7} H\right); \quad (7.4)$$

- ϕ is the latitude;
- g is the standard acceleration of gravity (9.80665 m s^{-2});
- T_m is the mean temperature of water vapour in K and can be computed from

$$T_m = (T_0 - \beta H) \left(1 - \frac{\beta R}{g_m \lambda'} \right); \quad (7.5)$$

- $\lambda' = \lambda + 1$ (unitless);
- k_1, k_2 and k_3 are refractivity constants with values $77.60 \text{ K mbar}^{-1}$, 16.6 K mbar^{-1} and $377600 \text{ K}^2 \text{ mbar}^{-1}$, respectively.

The total slant delay is computed according to

$$d_t = m_h d_h^z + m_{nh} d_{nh}^z, \quad (7.6)$$

where m_h and m_{nh} stand for hydrostatic and non-hydrostatic Niell [1996] mapping functions, respectively.

The procedure above has been used in all versions of UNB models, with the difference between them depending on the way the meteorological parameters (T_0 , P_0 , e_0 , β , and λ) are determined. Other models have also been based on the same principles, such as the Galileo System Test Bed models developed by European Space Agency [Krueger et al., 2004]. In the case of UNB3m, a look-up table with average and amplitude of the

meteorological parameters derived from the U.S. Standard Atmosphere Supplements, 1966 [COESA, 1966] is used. Table 7.2 shows the UNB3m look-up table.

Table 7.2. Look-up table of UNB3m model.

Average					
Latitude (degrees)	Pressure (mbar)	Temperature (K)	RH (%)	β ($K m^{-1}$)	λ (unitless)
15	1013.25	299.65	75.0	6.30e-3	2.77
30	1017.25	294.15	80.0	6.05e-3	3.15
45	1015.75	283.15	76.0	5.58e-3	2.57
60	1011.75	272.15	77.5	5.39e-3	1.81
75	1013.00	263.65	82.5	4.53e-3	1.55
Amplitude					
Latitude (degrees)	Pressure (mbar)	Temperature (K)	RH (%)	β ($K m^{-1}$)	λ (unitless)
15	0.00	0.00	0.0	0.00e-3	0.00
30	-3.75	7.00	0.0	0.25e-3	0.33
45	-2.25	11.00	-1.0	0.32e-3	0.46
60	-1.75	15.00	-2.5	0.81e-3	0.74
75	-0.50	14.50	2.5	0.62e-3	0.30

Using the table above, UNB3m is able to predict total zenith delays with an average rms of 4.9 cm [Leandro et al., 2006]. Previous analysis showed that this rms value likely could be improved if more realistic meteorological parameter values were used. Collins and Langley [1998] showed that if UNB models are used with surface-measured meteorological values, they can provide delays with an uncertainty of around 3.5 cm, which would be the performance of a UNB neutral atmosphere model if a perfect surface meteorology model could be implemented. Based on these numbers it is possible to state that a better model than the currently used UNB3m could provide zenith delays with uncertainties between 3.5 and 4.9 cm. One of the reasons why UNB3m is not capable of predicting delays with uncertainty close to 3.5 cm is the fact that the current look-up table is not able of accommodate the differences in the average surface meteorology of different regions. Part of this modeling inability is also due to day-to-day variation of

meteorological parameters, however this variation impacts any prediction model, since the modeled behavior is always a smooth curve in time (in our case a cosine curve over the year) while real values are points scattered about this line. Figure 7.3 shows the day-to-day variation of measured and UNB3m predicted meteorological parameters over several years for 50° N, 66° W. The blue crosses are the surface measurements of temperature, pressure and water vapour pressure, and the red dots are the predicted values using UNB3m.

The advantage of having a more realistic UNB model with the same functional model is improving the values of the yearly averages and amplitudes, as well as their geographical variation. This is the motivation for creating a new model, capable of describing the behavior of meteorological values more realistically.

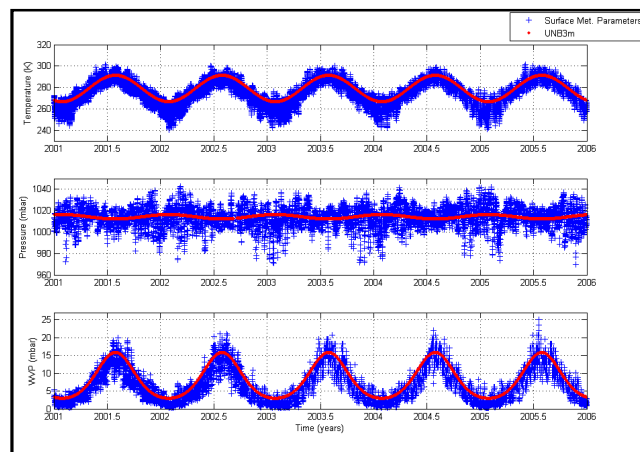


Figure 7.3. UNB3m surface meteorological parameter predictions compared to measured surface parameter values for 50° N, 66° W.

Although UNB3 is currently the most widely used version of UNB models, the most recent one is UNB3m, which offers a significant improvement in terms of non-hydrostatic zenith delay prediction compared to its predecessor.

In this chapter I am introducing a new model, which was designed to provide better predictions for different regions inside a delimited wide area. The goal is to have a more reliable model for wide area augmentation system users, with some homogeneity in terms of performance over the area of interest. These new models are called here wide area neutral atmosphere models, and are treated in more detail in the next section.

7.2. UNB wide area models

In this section I am introducing the concept of UNB wide area models. The first important characteristic of these models is that they keep the same physical assumptions as before (Equations 7.1 to 7.5). The key difference in the new approach is the way the surface meteorological values are evaluated, in this case, using a two-dimensional grid table instead of a latitude-band look-up table.

One of the first aspects to be taken into account when generating a new model is the data available for its calibration. In this work, I have used a data set with world wide hourly measurements of surface temperature, surface dew point temperature and mean sea level barometric pressure. The measurements were made between the years of 2001 and 2005 inclusive. This dataset was provided by NOAA, from its Integrated Surface Hourly (ISH)

Database. Figure 7.4 shows the global distribution of the ISH database, a total of 17,415 stations.

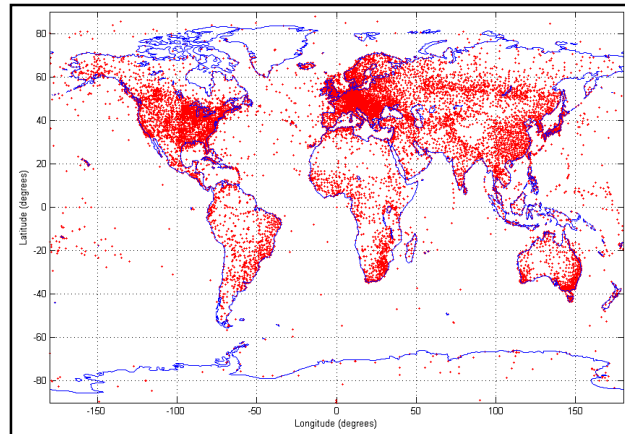


Figure 7.4. Distribution of ISH Database meteorological stations.

The observations of surface temperature, pressure and dew point temperature are used to calibrate a grid with average and amplitude values (to be used as in Equation 7.1) for each of the three parameters (In the case of dew point temperature, it is converted to relative humidity, as it will be shown later). Near surface temperature lapse rate and water vapor pressure height factor parameters can also be computed if desired. The functional model used for the grid interpolation is very simple, based on the four nearest grid nodes to the observation point (in case of grid calibration) or prediction point (in case of grid use). The value of interest can be computed according to the following formula:

$$X = (1 - p)(1 - q)x_1 + p(1 - q)x_2 + q(1 - p)x_3 + pqx_4, \quad (7.7)$$

where X is the computed value (it is either the average or amplitude of one of the modeled parameters), x_i is the parameter value at grid node i , and p and q are shown in Figure 7.5.

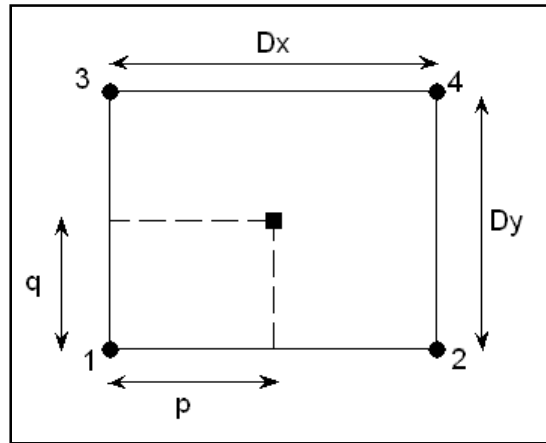


Figure 7.5. Grid interpolation procedure

In Figure 7.5 Dx and Dy represent the grid spacing in longitude and latitude, respectively. The black square in the middle of the grid represents the observation point, with coordinates ϕ_p and λ_p . The values for p and q can be computed as:

$$p = (\lambda_p - \lambda_1) / Dx, \quad (7.8)$$

and

$$q = (\phi_p - \phi_1) / Dy, \quad (7.9)$$

where λ_p and ϕ_p are the longitude and latitude of the point of interest, and λ_1 and ϕ_1 are the longitude and latitude of grid node 1 (as represented in Figure 7.5). Therefore p and q can assume values between 0 and 1.

Once all surface meteorological parameters for the point of interest are determined using the procedure above, the neutral atmosphere delays can be estimated using Equations 7.1 to 7.6. As can be seen, the use of the grid does not bring any significant complexity to the user, however the grid calibration is not a simple procedure.

The establishment of the values for each grid node is carried out in three steps. The first one is the calibration of the temperature (T) grid, followed by pressure (P) and relative humidity (RH) grids. The computation is performed on a station-by-station basis, where all data (all measurements over the observed years) is processed at each station step. For each station, the computation is performed on a year-by-year basis. This procedure is used to improve processing time, since the amount of data is too large to be processed in one single batch adjustment. The general least-squares adjustment model (used in all three grid calibrations) is:

$$\underline{x} = \underline{x}_0 + (\underline{A}'\underline{P}\underline{A} + \underline{N}_p)^{-1} \underline{A}'\underline{P}\underline{w}, \quad (7.10)$$

where \underline{x} is the vector of updated parameters, \underline{x}_0 is the vector of a-priori parameters (coming from previous updates), \underline{A} is the design matrix, \underline{P} is the weight matrix, \underline{N}_p is

the parameter normal matrix (coming from previous updates) and \underline{w} is the misclosure vector. The parameter normal matrix gets updated at each step, as follows:

$$\underline{N}_{pu} = (\underline{A}^t \underline{P} \underline{A} + \underline{N}_{p0}), \quad (7.11)$$

where \underline{N}_{pu} is the updated normal matrix and \underline{N}_{p0} is the a-priori normal matrix. The updated matrix is used as \underline{N}_p in equation 7.10 at the next parameter update, and then used as \underline{N}_{p0} in 7.11, and so on. The observations involved in each update step are the surface meteorological measurements for the current station and current year. The parameters are adjusted for the four nearest grid nodes, using the same functional model as in 7.7. Therefore the functional model in the adjustment of each grid type (T, P, RH) is built considering equation 7.7 plus the relevant formulas (relating interpolated grid values to measurements) for the given parameter type.

The first step, the temperature grid calibration, involves the adjustment of values for mean sea level temperature and optionally the temperature lapse rate. In case the lapse rates are not being adjusted, a-priori values from UNB3m are used as known values (as it will be seen later, this was the case of UNB3w.na model). The basic functional model for this step is given by:

$$T = T_0 - \beta H, \quad (7.12)$$

or, introducing the yearly variation:

$$T = \left(T_{\text{avg}} - T_{\text{amp}} \cos\left(\frac{\text{doy} - 28}{365.25}\right) \right) - H \left(\beta_{\text{avg}} - \beta_{\text{amp}} \cos\left(\frac{\text{doy} - 28}{365.25}\right) \right), \quad (7.13)$$

where T is the surface temperature measurement, T_{avg} and T_{amp} are the mean sea level temperature yearly average and amplitude respectively and β_{avg} and β_{amp} are the temperature lapse rate yearly average and amplitude respectively. Using this function yields the partial derivatives:

$$\frac{\partial T}{\partial T_{\text{avg},i}} = \frac{\partial T}{\partial T_{\text{avg},p}} \frac{\partial T_{\text{avg},p}}{\partial T_{\text{avg},i}} = \frac{\partial T_{\text{avg},p}}{\partial T_{\text{avg},i}}, \quad (7.14)$$

$$\frac{\partial T}{\partial T_{\text{amp},i}} = \frac{\partial T}{\partial T_{\text{amp},p}} \frac{\partial T_{\text{amp},p}}{\partial T_{\text{amp},i}} = -\cos\left(\frac{\text{doy} - 28}{365.25}\right) \frac{\partial T_{\text{amp},p}}{\partial T_{\text{amp},i}}, \quad (7.15)$$

$$\frac{\partial T}{\partial \beta_{\text{avg},i}} = \frac{\partial T}{\partial \beta_{\text{avg},p}} \frac{\partial \beta_{\text{avg},p}}{\partial \beta_{\text{avg},i}} = -H \frac{\partial \beta_{\text{avg},p}}{\partial \beta_{\text{avg},i}}, \quad (7.16)$$

$$\frac{\partial T}{\partial T_{\text{amp},i}} = \frac{\partial T}{\partial \beta_{\text{amp},p}} \frac{\partial \beta_{\text{amp},p}}{\partial \beta_{\text{amp},i}} = H \cos\left(\frac{\text{doy} - 28}{365.25}\right) \frac{\partial \beta_{\text{amp},p}}{\partial \beta_{\text{amp},i}}, \quad (7.17)$$

where T is the surface temperature, the subscript p stands for parameters at the point of interest (not to be confused with p representing longitude difference and P representing

pressure) and the subscript i stands for parameters at the grid node i. Partial derivatives of point values with respect to grid node values (e.g. $\frac{\partial T_{avg,p}}{\partial T_{avg,i}}$) are evaluated as follows:

$$\begin{aligned} \frac{\partial X_p}{\partial X_1} &= (1-p)(1-q), & \frac{\partial X_p}{\partial X_2} &= p(1-q) \\ \frac{\partial X_p}{\partial X_3} &= q(1-p) \quad \text{and} \quad \frac{\partial X_p}{\partial X_4} &= pq \end{aligned} \quad (7.18)$$

The derivatives in equation 7.18 are used in all steps (T, P, RH) of the adjustments of the grids.

The design matrix for the temperature grid calibration is built according to:

$$A = \begin{bmatrix} \frac{\partial T^1}{\partial T_{avg,i}} & \frac{\partial T^1}{\partial T_{amp,i}} & \frac{\partial T^1}{\partial \beta_{avg,i}} & \frac{\partial T^1}{\partial \beta_{amp,i}} \\ \vdots & \vdots & \vdots & \vdots \\ \frac{\partial T^n}{\partial T_{avg,i}} & \frac{\partial T^n}{\partial T_{amp,i}} & \frac{\partial T^n}{\partial \beta_{avg,i}} & \frac{\partial T^n}{\partial \beta_{amp,i}} \end{bmatrix}, \quad (7.19)$$

where the superscripts 1 and n stand for the observation index (therefore, A is a matrix with n rows, for n observations). In case the lapse rates are not being adjusted, the design matrix has only two columns (the first two of Equation 7.19). The misclosure vector is computed according to:

$$w = T - T', \quad (7.20)$$

where T is the measured surface temperature and T' is the evaluated surface temperature according to equation 7.13.

After the temperature grid is calibrated (meaning values of T_{avg} , T_{amp} , β_{avg} and β_{amp} have been established for all of the grid nodes) the relative humidity grid can be adjusted, or alternatively the pressure grid, which does not depend on temperature or relative humidity.

The ISH database provides hourly measurements of MSL barometric pressure, no matter the height of the meteorological station. The consequence is that the pressure measurements have no relation with any lapse rate type parameter. In case of surface pressure, the respective lapse rate would be β , assuming the height variation of pressure relates to the temperature variation of pressure according to:

$$P_s = P_0 \left(1 - \frac{\beta H}{T_0} \right)^{\frac{g}{R\beta}} = P_0 \left(\frac{T}{T_0} \right)^{\frac{g}{R\beta}}, \quad (7.21)$$

where P_s stands for surface pressure. However, because the pressure measurements are related to mean sea level, the function model of the pressure grid adjustment becomes:

$$P = P_{avg} - P_{amp} \cos\left(\frac{\text{doy} - 28}{365.25}\right), \quad (7.22)$$

where P is the MSL pressure measurement and the yearly variation parameters (P_{avg} and P_{amp}) are similar to the ones previously used for T and β (equation 7.13). Partial derivatives are also evaluated similarly to equations 7.14 and 7.15:

$$\frac{\partial P}{\partial P_{avg,i}} = \frac{\partial P}{\partial P_{avg,p}} \frac{\partial P_{avg,p}}{\partial P_{avg,i}} = \frac{\partial P_{avg,p}}{\partial P_{avg,i}}, \quad (7.23)$$

$$\frac{\partial P}{\partial P_{amp,i}} = \frac{\partial P}{\partial P_{amp,p}} \frac{\partial P_{amp,p}}{\partial P_{amp,i}} = -\cos\left(\frac{doy - 28}{365.25}\right) \frac{\partial P_{amp,p}}{\partial P_{amp,i}}. \quad (7.24)$$

The design matrix then yields:

$$A = \begin{bmatrix} \frac{\partial P^1}{\partial P_{avg,i}} & \frac{\partial P^1}{\partial P_{amp,i}} \\ \vdots & \vdots \\ \frac{\partial P^n}{\partial P_{avg,i}} & \frac{\partial P^n}{\partial P_{amp,i}} \end{bmatrix}, \quad (7.25)$$

and the misclosure vector is computed according to:

$$w = P - P', \quad (7.26)$$

where P is the measured MSL pressure and P' is the evaluated MSL pressure according to equation 7.22.

The calibration of the relative humidity grid involves a little more complexity than the previous ones because (1) it depends on temperature and pressure grids; and (2) the measurements are surface dew point temperature, but the height variation is modeled for water vapor pressure (according to equation 7.31) and the yearly variation is modeled for relative humidity. The transformation between these three types of parameters needs to be carried out and incorporated in the functional model for the grid adjustment. The first part of the functional model is the computation of the MSL relative humidity, done similarly to T and P:

$$RH_0 = RH_{\text{avg}} - RH_{\text{amp}} \cos\left(\frac{\text{doy} - 28}{365.25}\right), \quad (7.27)$$

where RH_0 stands for MSL relative humidity and the subscripts avg and amp stand for yearly average and amplitudes, respectively. The relative humidity has then to be transformed in water vapour pressure, which will be used for height variation modeling. The relation between the two (relative humidity and water vapour pressure) is given by the following equation (according to IERS conventions 2003):

$$e_0 = RH_0 \cdot e_{s_0} \cdot f_{w,0}, \quad (7.28)$$

where e_0 is the MSL water vapour pressure, $e_{s,0}$ is the saturation water vapour pressure and $f_{w,0}$ is the enhancement factor (both for MSL). Values for $e_{s,0}$ and $f_{w,0}$ can be computed according to:

$$\begin{aligned}
 e_{s,0} = & 0.01 \cdot \exp(1.2378847 \times 10^{-5} T_0^2 \dots \\
 & - 1.9121316 \times 10^{-2} T_0 + 33.93711047 \dots, \\
 & - 6.3431645 \times 10^3 T_0^{-1})
 \end{aligned} \tag{7.29}$$

and

$$\begin{aligned}
 f_{w,0} = & 1.00062 + 3.14 \times 10^{-6} P_0 \dots \\
 & + 5.6 \times 10^{-7} (T_0 - 273.15)^2
 \end{aligned} \tag{7.30}$$

The relation between MSL and surface water vapour pressure is expressed using the same physical assumption as in equation 7.3, as follows:

$$e = e_{0,s} \left(1 - \frac{\beta H}{T_0} \right)^{\frac{\lambda' g}{R \beta}}, \tag{7.31}$$

where $e_{0,s}$ stands for surface water vapour pressure. The last part of the functional model is the relation between e and dew point temperature, which can be derived from basic thermodynamic laws [IERS conventions, 2003], resulting in:

$$e = es(T_d) \cdot f_{w,s}, \quad (7.32)$$

where $es(T_d)$ is the saturation water vapour pressure for the dew point temperature T_d , and can be computed from equation 7.29 substituting T_d for T_0 , and $f_{w,s}$ can be computed from equation 7.30 substituting in values of pressure and surface temperature. After putting equations 7.28 to 7.32 together, the complete functional model “observation equation” for relative humidity calibration becomes:

$$es(T_d) = RH_0 \cdot es_0 \cdot \frac{f_{w,0}}{f_{w,s}} \cdot \left(1 - \frac{\beta H}{T_0}\right)^{\frac{g\lambda'}{R\beta}}, \quad (7.33)$$

Where, as before, subscripts s and 0 stand for surface and MSL values, respectively. In order to introduce average and amplitude for the modeled parameters in equation 7.34, RH_0 is replaced by the right hand side of 7.28 and λ' is replaced by:

$$\lambda' = \lambda'_{avg} - \lambda'_{amp} \cos\left(\frac{doy - 28}{365.25}\right). \quad (7.34)$$

The partial derivatives can then be evaluated as:

$$\frac{\partial es(T_d)}{\partial RH_{avg}} = \frac{\partial es(T_d)}{\partial RH_{avg,p}} \frac{\partial RH_{avg,p}}{\partial RH_{avg,i}} = es_0 \cdot \frac{f_{w,0}}{f_{w,s}} \cdot \left(1 - \frac{\beta H}{T_0}\right)^{\frac{g\lambda'}{R\beta}} \cdot \frac{\partial X_p}{\partial X_i}, \quad (7.35)$$

$$\frac{\partial e_s(T_d)}{\partial RH_{aamp}} = \frac{\partial e_s(T_d)}{\partial RH_{aamp,p}} \frac{\partial RH_{aamp,p}}{\partial RH_{aamp,i}} = -\cos\left(\frac{\text{doy} - 28}{365.25}\right) \cdot \frac{\partial e_s(T_d)}{\partial RH_{avg}}, \quad (7.36)$$

$$\frac{\partial e_s(T_d)}{\partial \lambda'_{avg}} = \frac{\partial e_s(T_d)}{\partial \lambda'_{avg,p}} \frac{\partial \lambda'_{avg,p}}{\partial \lambda'_{avg,i}} = RH_0 \cdot e_{s,0} \cdot \frac{f_{w,0}}{f_{w,s}} \cdot \left(1 - \frac{\beta H}{T_0}\right)^{\frac{g \lambda'}{R \beta}} \cdot \frac{g}{R \beta} \cdot \ln\left(1 - \frac{\beta H}{T_0}\right) \cdot \frac{\partial X_p}{\partial X_i}, \quad (7.37)$$

and

$$\frac{\partial e_s(T_d)}{\partial \lambda'_{aamp}} = \frac{\partial e_s(T_d)}{\partial \lambda'_{aamp,p}} \frac{\partial \lambda'_{aamp,p}}{\partial \lambda'_{aamp,i}} = -\cos\left(\frac{\text{doy} - 28}{365.25}\right) \cdot \frac{\partial e_s(T_d)}{\partial \lambda'_{avg}}, \quad (7.38)$$

and the design matrix becomes:

$$A = \begin{bmatrix} \frac{\partial e_s(T_d)^l}{\partial RH_{avg,i}} & \frac{\partial e_s(T_d)^l}{\partial RH_{amp,i}} & \frac{\partial e_s(T_d)^l}{\partial \lambda'_{avg,i}} & \frac{\partial e_s(T_d)^l}{\partial \lambda'_{amp,i}} \\ \vdots & \vdots & \vdots & \vdots \\ \frac{\partial e_s(T_d)^n}{\partial RH_{avg,i}} & \frac{\partial e_s(T_d)^n}{\partial RH_{amp,i}} & \frac{\partial e_s(T_d)^n}{\partial \lambda'_{avg,i}} & \frac{\partial e_s(T_d)^n}{\partial \lambda'_{amp,i}} \end{bmatrix}. \quad (7.40)$$

The misclosure vector is computed according to:

$$w = e_s(T_d) - e_s(T_d)', \quad (7.41)$$

where $e_s(T_d)$ is computed according to equation 7.29 using the measured dew point temperature and $e_s(T_d)'$ is evaluated using equation 7.33. In case the lapse rate parameter

(λ') is not being adjusted, the design matrix has only its two first columns (related to RH) and λ' values from UNB3m are used as known values (this was the case of UNBw.na).

7.3. UNB wide area model for North America – UNBw.na

In this section the creation of a model for North America using the previously described procedure is discussed. The model is called UNBw.na, where w stands for wide area and na stands for North America. The grid was defined between latitudes 0 and 90 degrees, and longitudes between -180 and -40 degrees, with spacing of 5 degrees in the two directions. Figure 7.6 shows the North American grid.

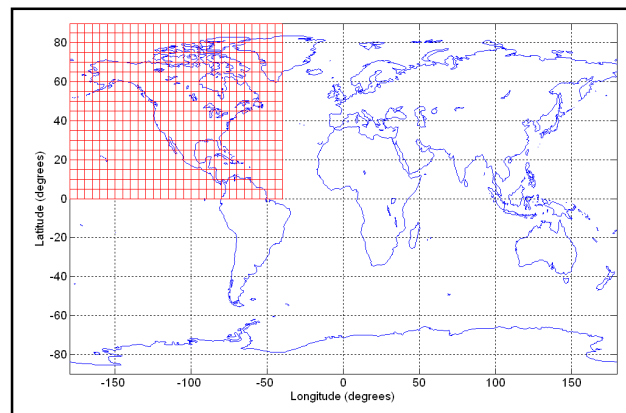


Figure 7.6. UNBw.na grid (red lines).

The grid is first initialized with UNB3m values, and then the grid node values are updated (adjusted) using the previously described approach. The initialization of the grid is fundamental for its adjustment because meteorological stations in the ISH database do not cover every cell of the grid. In this case, the grid node receives no update, and the consequence is a value equal to UNB3m's. The stations to be used in the calibration of

the grid were chosen simply taking all database stations within the grid (In this case a total of around 4000 stations). Figure 7.7 shows the distribution of meteorological stations over the grid.

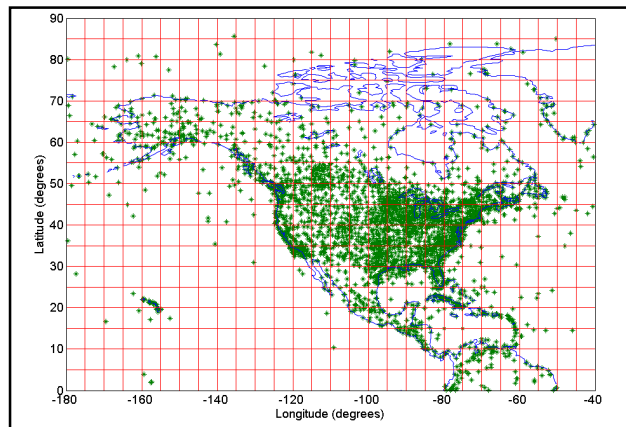


Figure 7.7. Distribution of meteorological stations over the UNBw.na grid

In order to assess the grid adjustment, 400 stations were randomly separated from the dataset to be used as control stations. These data were not used in the grid calibration, and after each adjustment step they were used to check results obtained for temperature, pressure and water vapour pressure. Figure 7.8 shows the distribution of the control stations (black dots) and calibration stations (green crosses).

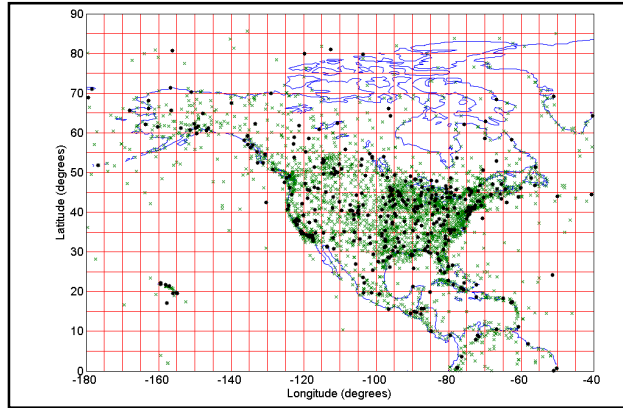


Figure 7.8. Distribution of the control stations (black dots) and the calibration stations (green crosses).

As shown in the previous section, the temperature lapse rate and water vapour pressure height factor could be calibrated or not. The two approaches were tested for this data set, and it turned out that the model provided slightly better results when lapse rates from UNB3m were used as known and were not recalibrated. One of the reasons which could have caused this is the fact that stations within a given grid cell have similar heights, which causes difficulties in the decorrelation between temperature or water vapour pressure and their lapse rate parameters. Figure 7.9 shows the height (represented by color) of the stations, where it is possible to notice that apart from a few cells, the height of stations inside cells is usually very similar.

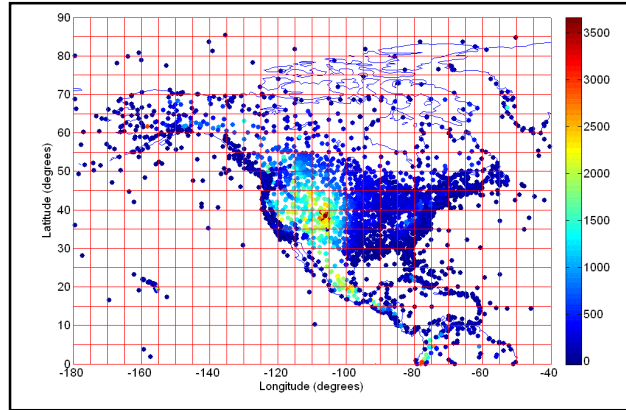


Figure 7.9. Height (in meters – represented by color) of the meteorological stations.

The results are presented only for the case when the lapse rates were not calibrated.

Figure 7.10 shows a representation of average MSL temperature given by UNB3m and UNBw.na for all grid nodes of the model. It is possible to notice that UNBw.ca shows lower temperatures for some northern regions. Also, for some regions, the temperature does not quite follow a variation dependent on latitude only. The two grids are practically the same for grid nodes outside the continent (over the oceans) because there is not enough data for grid calibration in these regions (see Figure 7.7), and UNB3m values from the initialization are almost unmodified by the calibration process.

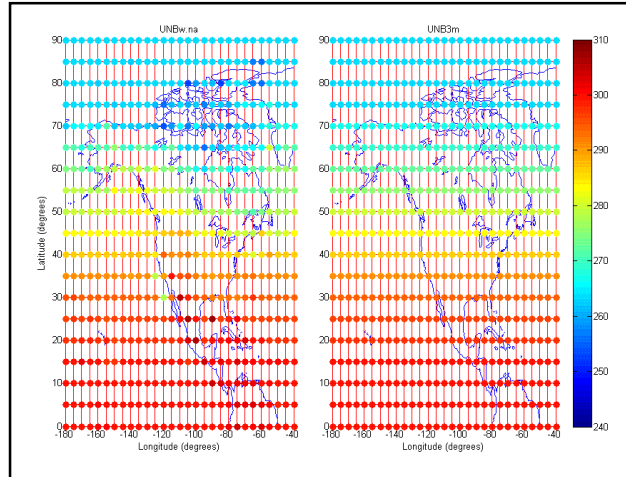


Figure 7.10. Average MSL temperature given by UNB3m and UNBw.na, in kelvins.

Figure 7.11 shows the difference between the two models, in the sense of UNBw.na-UNB3m. It can be seen that UNBw.na provides higher temperatures over the western part of North America, and lower temperatures for land mass with higher latitudes over the eastern part of the continent.

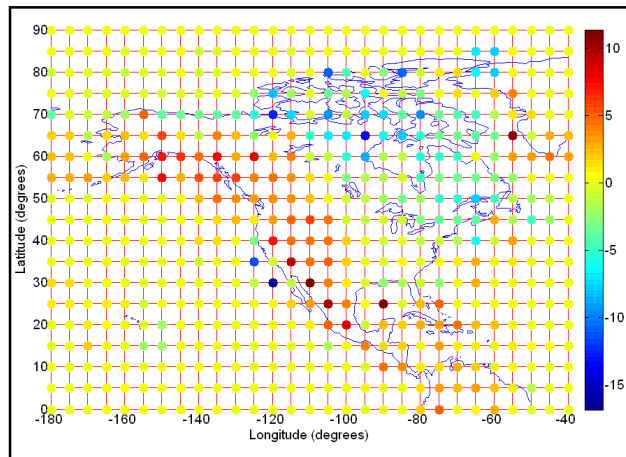


Figure 7.11. MSL temperature difference between UNBw.na and UNB3m, in kelvins.

With the estimation of temperature for control stations it is possible to check if these differences are bringing improvement to the model or not. Figure 7.12 shows the biases

encountered when estimating temperatures for control stations, using the two models, in the sense modeled value – observed value. It is possible to notice that there is a significant improvement in estimation for stations in the western part of North America, matching with differences of grid values (Figure 7.11) for the same region. It can also be noticed that UNB3m slightly overestimates the temperature for a localized region near the east coast. In terms of UNBw.na one can see that there is no trend related to longitude variation.

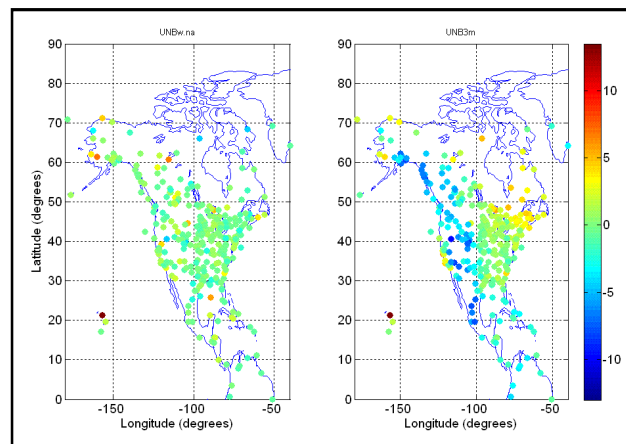


Figure 7.12. Biases encountered when estimating temperature for control stations, in kelvins.

General statistics for temperature estimation errors for the two models with respect to control station values can be seen in Table 7.3, where it is possible to notice the overall improvement brought by UNB3w.na in terms of temperature estimation. The values in Table 7.3 (and similar tables for pressure and water vapour) were computed using one set of values (bias, standard deviation and rms) per station, regardless of the number of measurements available for each station. There is a significant improvement in the bias of the model (91%), showing that UNB3m generally underestimates the mean temperature.

This systematic behavior is dominated by the temperature underestimation over the western part of the continent.

Table 7.3. General statistics for temperature estimation errors (all values in kelvins).

	Bias	Std. Dev.	RMS
UNBw.na	0.06	5.57	5.80
UNB3m	-0.68	6.04	6.80

The results of the following step in grid calibration (the pressure grid) is shown in Figure 7.13, where it can be noticed that UNBw.na also does not follow the latitude (only) dependence of UNB3m.

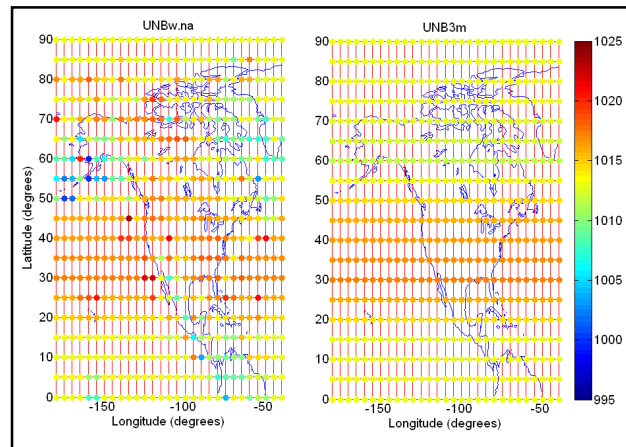


Figure 7.13. Average pressure at grid nodes, given by UNBw.ca and UNB3m, in mbar.

Figure 7.14 shows the difference between average MSL pressure of the two models, in the sense of UNBw.na-UNB3m. It can be noticed that the major differences are encountered in regions situated in the northwest, northeast and southern parts of the continent. Differences vary up to around 10 mbar, which means a difference of around 2

cm in hydrostatic delay estimation (according to Equation 7.2, if we consider a point at MSL, the delay rate with respect to pressure is around 0.0022 m/mbar).

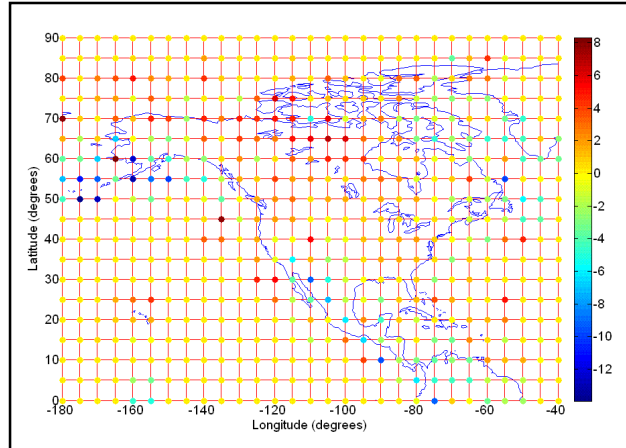


Figure 7.14. Average MSL pressure difference between UNBw.na and UNB3m, in mbar.

Figure 7.15 shows the biases of UNB3m and UNBw.na when estimating pressure for the control stations, where it can be seen that UNBw.na performs better than UNB3m for the regions where greater differences are found. Overall, the bias plot of UNBw.na is greener than UNB3m's, which means it is usually closer to zero (green is zero on the color scale).

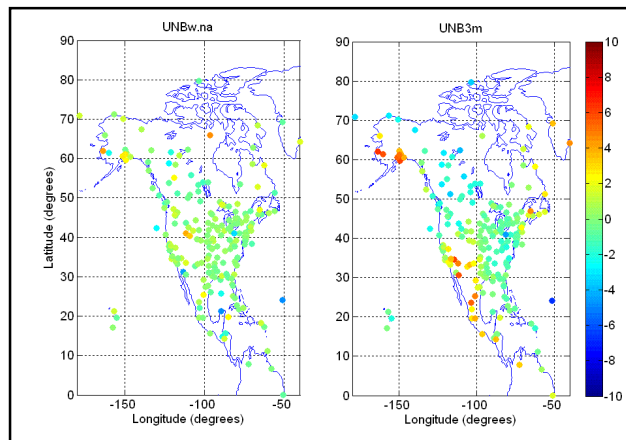


Figure 7.15. Mean biases encountered when estimating pressure for control stations, in mbar.

The general statistics for pressure estimation are shown in Table 7.4.

Table 7.4. General statistics for pressure estimation errors (all values in mbar).

	Bias	Std. Dev.	RMS
UNBw.na	0.05	3.89	3.95
UNB3m	0.02	3.95	4.12

From Table 7.4 it can be noticed that the differences for bias, standard deviation and rms between the two models are low (considering estimated delays, 1 mbar corresponds to around 2 mm in the zenith direction). Although the general bias of UNBw.na is slightly worse than UNB3m's, UNBw.na's better fitting for different regions is translated into an improvement in standard deviation and rms.

The last step of the model calibration is the relative humidity grid. Following the same procedure as for the other two steps in terms of reporting results, Figure 7.16 shows the average MSL values of RH (in %) for all grid nodes, given by UNBw.na and UNB3m, where it can be seen that UNBw.na shows a drier area in the southwest part of the continent. This difference can be better visualized in Figure 7.17, which shows the difference in the average MSL values between the two models for each grid node, in the sense of UNBw.na-UNB3m (in %).

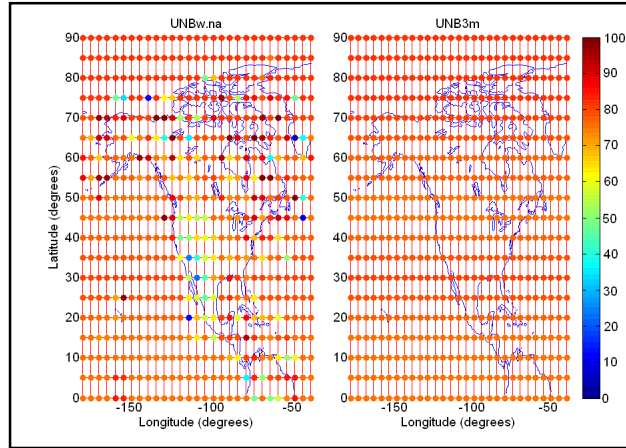


Figure 7.16. Average MSL relative humidity for grid nodes, given by UNBw.na and UNB3m, in %.

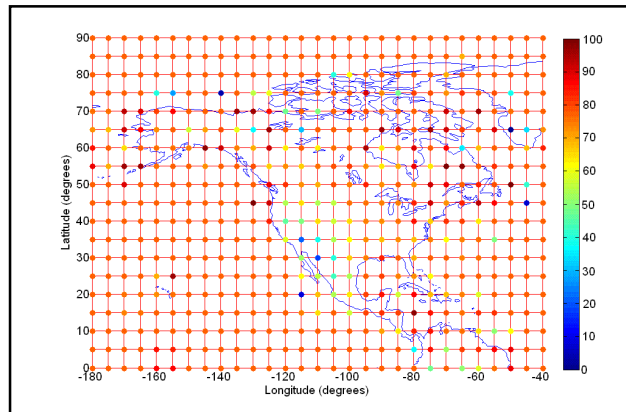


Figure 7.17. Difference between average MSL relative humidity provided by UNBw.na and UNB3m, in %.

The biases of the water vapour pressure (WVP) estimation for control stations are shown in Figure 7.18, where we can notice that UNB3m overestimates the WVP for the southwest part of the continent, while UNBw.na does not. There is also a region with a small improvement in the northwest part of the continent (is this last case, UNB3m underestimates the WVP).

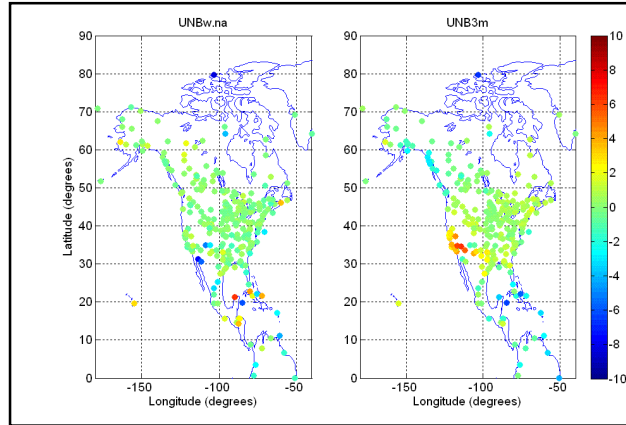


Figure 7.18. Mean biases encountered when estimating water vapour pressure for control stations, in mbar.

The general performance results can be seen in Table 7.5, where it can be noticed that there is an improvement (around 50%) in bias when estimating surface WVP with UNBw.na, compared to UNB3m. There is a small improvement in standard deviation, indicating a slightly better fitting to real conditions by UNBw.na.

Table 7.5. General statistics for WVP estimation errors (all values in mbar).

	Bias	Std. Dev.	RMS
UNBw.na	-0.10	2.30	2.47
UNB3m	0.20	2.43	2.65

7.4. UNBw.na validation with ray-traced delays

In order to verify if UNBw.na is more realistic than UNB3m in terms of delay estimation, a validation process was realized. In this approach radiosonde-derived delays were used as reference (“truth”). The radiosonde profiles of temperature, pressure, and dew point temperature were used to compute zenith delays by means of a ray-tracing technique. We used radiosonde soundings taken throughout North America and some neighboring

territories through the years from 1990 to 1996 inclusive. This dataset is compiled and made available by NOAA (National Oceanic and Atmospheric Administration). A total of 222 stations were used, distributed as shown in Figure 7.19.

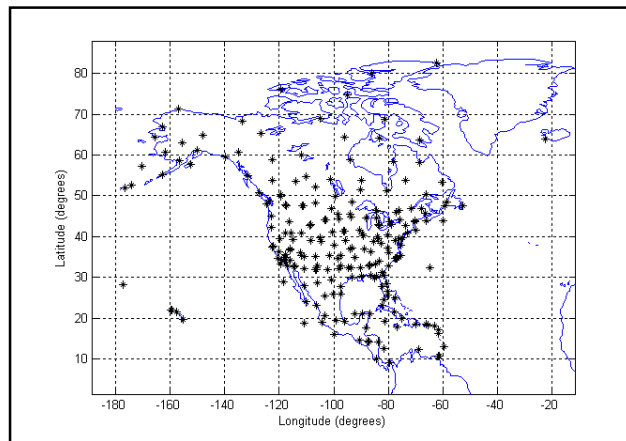


Figure 7.19. Distribution of radiosonde stations in North America and some nearby territories.

Each station usually has a balloon being launched twice a day, totaling 701,940 soundings for all stations, all years. For each one of the soundings, a total delay was predicted using UNBw.na and UNB3m, and then compared with the ray-traced total zenith delays. From this comparison, bias and rms values could be computed for each one of the stations shown in Figure 7.19. Figure 7.20 shows the mean biases found for all stations with the two models.

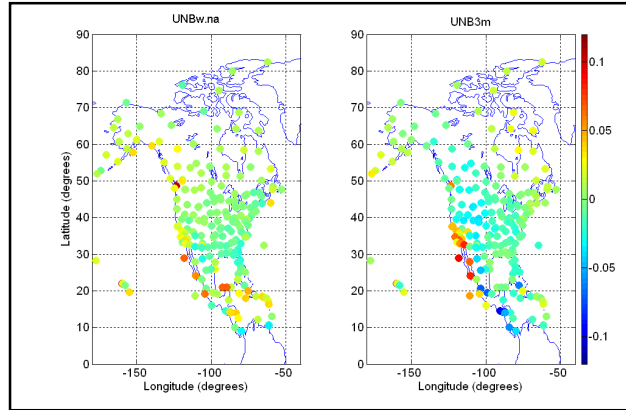


Figure 7.20. Total zenith delay estimation biases for each station, in meters.

In Figure 7.20, the zero value is green according to the color scale. It is possible to notice that the UNBw.na plot shows colors generally closer to green than UNB3m. It can also be noticed that in the western part of the continent, where UNB3m has its worse performance, there is a significant improvement with the new model. The rms values for the same stations can be seen in Figure 7.21, where it is possible to see that UNBw.na plot presents colors generally closer to blue (in this plot zero is represented by dark blue), also with a good improvement for the region with worst results provided by UNB3m.

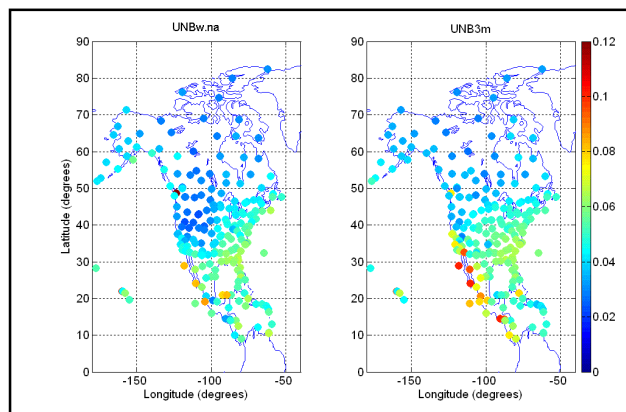


Figure 7.21. Total zenith delay estimation rms values for each station, in meters.

The general statistics of delay prediction performance of the two models are shown in Table 7.6, where we can see that there is a general improvement of absolute bias of around 30%, and small improvements in standard deviation (8%) and rms (9%).

Table 7.6. General statistics of total zenith delay prediction performance (all values in mm).

	Bias	Std. Dev.	RMS
UNBw.na	3.6	44.8	45.0
UNB3m	-5.2	48.9	49.2

Although the general rms doesn't show a significant improvement, the major concern with UNB3m is not its overall performance, but its performance in localized areas. In order to assess the performance of the models in different regions, the coverage area was divided into four analysis regions, trying to have approximately the same number of radiosonde stations in each one of them. Figure 7.22 shows the division of the four regions.

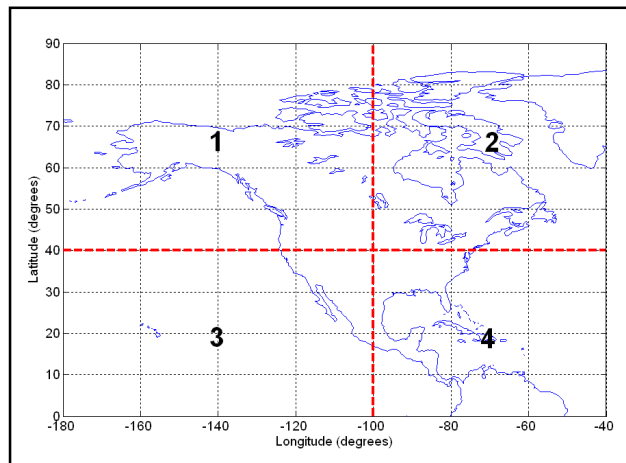


Figure 7.22. Division of the four analysis regions.

The statistics for each one of the analysis regions are shown in Table 7.7.

Table 7.7. Statistics (bias, standard deviation and rms) for analysis regions (all values in cm).

Region	UNBw.na			UNB3m		
	Bias	SD	RMS	Bias	SD	RMS
1	1.0	3.4	3.6	-0.9	3.5	3.7
2	0.4	4.1	4.1	0.5	4.3	4.3
3	0.6	4.4	4.4	0.2	5.7	5.7
4	-0.3	5.4	5.5	-1.3	5.6	5.8

In Table 7.7 it can be noticed that rms values for UNBw.na are better than UNB3m's for all regions, with a significant improvement for region 3 (around 23%). The bias of region 3 for UNBw.na is higher than for UNB3m, however it does not mean UNB3m is better, because although the mean bias is less, the variation of biases (above and below zero) is much higher than for UNBw.na (as can be noticed in Figure 7.20). This effect shows up in UNB3m's standard deviation and rms in region 3, which are significantly higher than UNBw.na's. Another way to show that is by computing the average absolute biases and their standard deviation, computed without considering bias sign. These values are shown in Table 7.8, where it can be noticed that, indeed, the average absolute bias and its standard deviation is significantly higher for UNB3m in region 3 (UNBw.na shows an improvement of around 25%).

Table 7.8. Average absolute biases (aab) and their standard deviations (aab-sd) - all values in cm.

Region	UNBw.na		UNB3m	
	aab	aab-sd	aab	aab-sd
1	2.8	2.2	2.8	2.3
2	3.2	2.6	3.4	2.7
3	3.4	2.9	4.5	3.6
4	4.5	3.2	4.7	3.4

One of the problems encountered in UNB neutral atmosphere modes is a systematic behavior with respect to station height [Leandro et al., 2006]. In order to verify if the new model has the same problem, Figure 7.23 shows a plot of station biases with respect to station heights. The error bars are (one sigma) standard deviations of the bias computation for each of the stations, and the red line is the fitted (using the points shown in the plots) linear trend of the models. The upper plot shows results of UNBw.na and the lower one shows UNB3m's results.

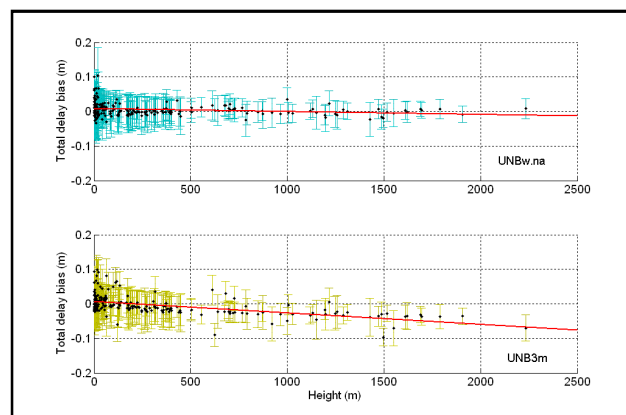


Figure 7.23. Station biases with respect to station heights.

It can be seen in Figure 7.23 that UNBw.na does not have a trend as significant as UNB3m, because while UNB3m biases tend to increase negatively as the height goes up, UNBw.na biases are kept with values around zero no matter the height of the station. This difference can also be clearly seen comparing the two trend lines (red lines) of the models.

In order to visualize the fit of the model estimations to the yearly variation of the zenith total delay, a few stations were selected for analysis. The station selection was based on availability of data for given stations over the period of time of the data set 1990-1996, having sample stations for different latitudes. The chosen stations are Belize, Pittsburgh, Salt Lake City, Bethel and Eureka. Figures 7.24 to 7.28 show the radiosonde ray-raced total zenith delays compared with UNB3m and UNBw.na predictions for each of the stations.

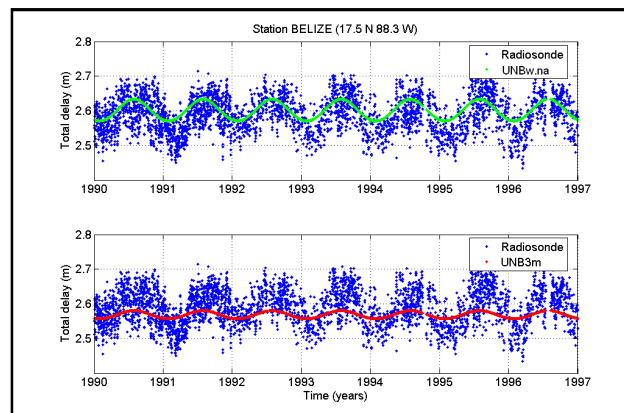


Figure 7.24. Total zenith delay estimation for station Belize.

The estimations provided by UNB3m for station Belize have a problem with the annual amplitude of the delays. This effect is caused by the fact that UNB3m assumes that meteorological parameters do not vary over the year for latitudes between 15°N and 15°S. The problem with amplitude underestimation affects even stations at higher latitudes, as in the case of station Pittsburgh. UNBw.na shows a good improvement in terms of estimated annual amplitude, as can be seen for these two stations.

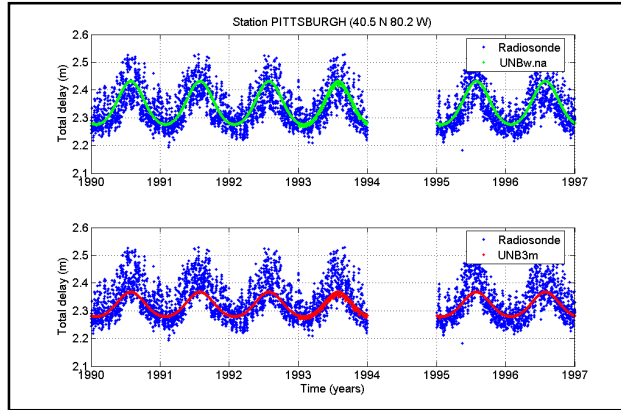


Figure 7.25. Total zenith delay estimation for station Pittsburgh.

Another problem suffered by UNB3m in the case of Pittsburgh is the underestimation of the delays, which also occurs for Salt Lake City. The average of the delays provided by UNBw.na seem to match much better with ray-traced delays than UNB3m's for these stations.

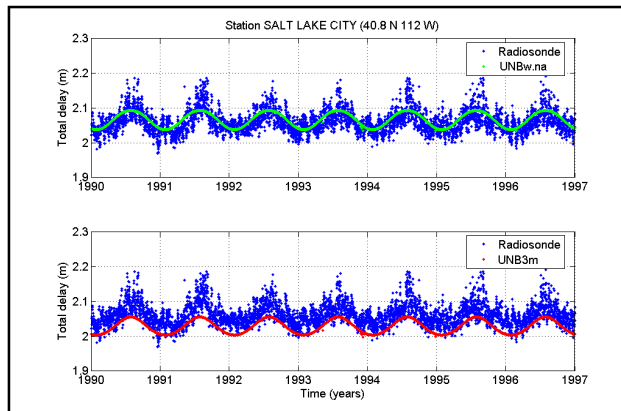


Figure 7.26. Total zenith delay estimation for station Salt Lake City.

In the case of station Bethel both models seem to work fine, with a good fit with radiosonde-derived delays. However for the northern station, Eureka (80°N), UNB3m predictions are generally overestimating the delays, while UNBw.na is closer to the average values of the ray-traced delays over the years.

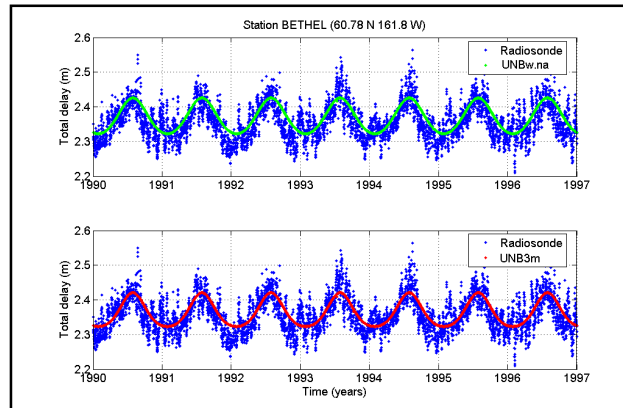


Figure 7.27. Total zenith delay estimation for station Bethel.

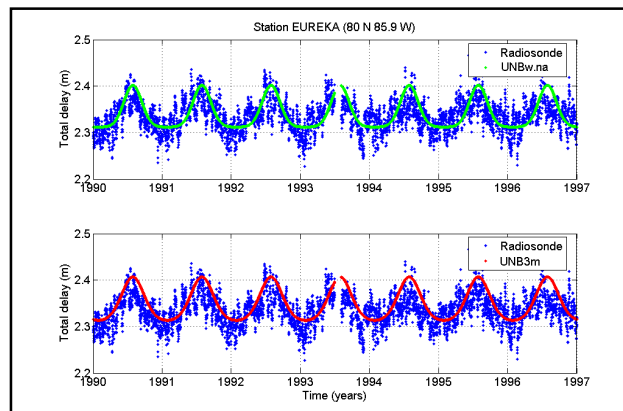


Figure 7.28. Total zenith delay estimation for station Eureka.

Table 7.9 shows the numerical results for each of the five stations. With the exception of station Bethel, UNBw.na shows better results for all stations, with improvement of up to 2.8 cm in bias and 1.6 cm in rms (both for station Salt Lake City). If the biases for all stations are considered, it is possible to notice that UNBw.na has more consistent (homogeneous) results for different locations.

Table 7.9. Numerical results for sample stations (represented by the first four characters of their names) – all values in cm.

	UNBw.na		UNB3m	
Station	Bias	RMS	bias	RMS
BELI	1.4	4.7	2.1	5.3
PITT	0.6	4.7	-1.8	5.3
SALT	0.5	2.6	-3.3	4.2
BETH	1.2	3.8	0.6	3.6
EURE	0.5	2.9	1.5	3.2

7.5. Chapter remarks

In this chapter an approach for creation of wide area neutral atmosphere models was comprehensively described and discussed. A dataset with hourly surface meteorological measurements was used to create a new model for North America, called here UNBw.na.

The calibration of surface temperature and water vapour pressure lapse rate parameters was performed, and after comparing results of a model calibration with fixed lapse rates it was concluded that better performance is achieved in the second case. One of the reasons behind this conclusion might be the fact that the used dataset (surface meteorological parameters) is not adequate to successfully decorrelate surface lapse rates from actual parameters, due to fact that stations nearby each other tend to have similar heights.

The meteorological values derived from the grids of the new model were compared with actual surface measurements, realized at stations which were not used in the calibration process. All analyses took into consideration the most recent version of UNB models, until now UNB3m.

Results for all three meteorological parameters showed that a two-dimensional grid-based model could perform better than a latitude (only) based model (such as UNB3m). The reason for that is the capability of accommodating longitude or regional climatic characteristics of the continent. In terms of temperature the general bias was practically eliminated, with a reduction of 91% (-0.68 to 0.06 K), while rms was improved by 15% (6.8 to 5.8 K). Pressure estimations were also improved in the new model, with a reduction of more than 50% in bias (0.05 to 0.02 mbar) and a slight improvement in rms (4.12 to 3.95 mbar). Water vapour pressure predictions had their general bias reduced 50% (0.2 to -0.1 mbar), also with slight improvement in rms (2.65 to 2.47 mbar). Although the general results do not show a spectacular improvement, the new model is consistently better than its predecessor, and, the improvement for certain regions is more significant than others. Regions where the performance of the old model was not satisfactory had results significantly improved with the new model.

A validation of UNBw.na predicted zenith delays was realized using radiosonde-derived delays as reference. Soundings carried out throughout North America and some neighboring territories through the years from 1990 to 1996 inclusive were used in this analysis, totaling 222 stations. General results from this analysis showed a general improvement of bias of around 30%, and small improvements in standard deviation (8%) and rms (9%).

Because the main goal with the new model is predicting zenith delays with a consistent uncertainty for different areas, the continent was divided into four analysis regions. This was done to detect localized improvements when using UNBw.na. This analysis showed that all regions manifested improvement for the estimations with the new model.

A problem with systematic behavior of biases (of zenith delay estimation) with height which has been previously detected in UNB neutral atmosphere models no longer exists in UNBw.na. Biases were shown to be consistently close to zero, no matter the height of the station.

Investigation of the performance of both models (UNBw.na and UNB3) with radiosonde ray-raced delays at a few sample stations showed that UNBw.na generally has a better fit to the yearly behavior of the zenith delays. It was also possible to notice that results from UNBw.na are more consistent between stations at different locations than when using UNB3m.

In terms of general conclusions, UNBw.na was shown to be consistently better than UNB3m in several aspects. The adopted procedure for the grid calibration worked in an adequate way, resulting in a reliable model.

Further research on this topic should involve investigation of lapse rate parameters, which were not calibrated in this work, perhaps using radiosonde data. The model for delay computation, which has not been modified so far, will also be reviewed.

Assimilation of different data, such as numerical weather models or contemporary standard atmospheres, still needs to be investigated. Future research can also include the calibration of wide area models for different regions of the globe, such as South America. GAPS currently does not use UNBw.na, therefore I also suggest for future activities the implementation and performance analysis of UNBw.na and/or other wide area models with GAPS or other PPP package.

8. Conclusions and recommendations

In this thesis I have shown that a precise point positioning (PPP) package can be used not only for positioning, but also as a tool for a series of data analysis. In order to demonstrate that, I have presented new analysis techniques which can be applied using data collected by a single receiver. These techniques deal with the estimation of ionospheric delays, satellite code biases, code multipath plus noise and satellite pseudo-clocks. The novelty of the research presented in here relates not only of getting information out of a precise point positioning package, but also feeding PPP with more reliable information. This is particularly true for the improved neutral atmosphere prediction model which was developed for North America.

The main tool used for this research is the precise point positioning package GAPS (GPS Analysis and Positioning Software). GAPS has been developed by myself since January 2006, and is an important practical contribution of this research. GAPS is freely available to be used by anyone via web interface, as part of the UNB/GGE Resources. An additional practical contribution of the research was the development and availability of the UNB3m neutral atmosphere model package.

This thesis' contributions are summarized as follows:

1. Single receiver ionospheric delay estimation

In chapter 3, I introduced a filter which can be used to estimate ionospheric delays using a single receiver. The procedure can be conveniently implemented into any PPP engine. One of the main advantages of having such a filter is that the PPP engine can be used as a stand-alone, static or kinematic, sensor of the ionosphere. On other hand, a model of the ionosphere at the single receiver site might provide a significant contribution towards the enhancement of the positioning solution, such as a future ambiguity-fix positioning procedure. The ionospheric delay observation model is based on geometry-free carrier-phase measurements, and considers the ionosphere as an earth-concentric spherical shell. The variation of the zenith ionospheric delay over the shell surface is modeled with a bilinear polynomial.

Results have shown that the model residuals are usually less than 2 TECU pick to pick during ionospheric calm periods, and can reach values as high as 10 TECU (as far as the realized tests go) during ionospheric storm picks. When comparing delay values independently obtained from two nearby stations, the results showed a very good agreement, of usually better than 0.3 TECU. When comparing the results with values provided by IGS, the time series behavior between the two estimates (IGS and GAPS) were found to be quite similar, with an overall agreement RMS seems to be around 4 TECU or so, where most of the mismatch looks to be coming from a bias effects. Since the other analyzes (residual analysis and independent nearby station results) showed to be quite consistent, it is probable that this mismatch might be caused by different assumptions used in the two estimates, such as the ionospheric shell height. The main recommendations therefore are that the full procedure used in GAPS is re-analyzed in

order to find which assumptions are being used differently from IGS maps, aiming at a greater similarity between the two procedures, which would be a desirable characteristic of the approach.

2. Satellite differential code bias estimation

A new technique to estimate satellite differential code biases based on PPP was presented. This technique is based on the fact that IGS clocks are based on L1P(Y) and L2P(Y) code measurements while the receiver tracks e.g. L1C/A and L2P(Y) codes. Using a straightforward reformulation of the code observation equations it is possible to obtain the satellite code biases (in this particular case, the so called P1-C1 biases) from a single receiver running a PPP engine. A comparison of estimated satellite P1-C1 biases with a monthly CODE solution showed an overall agreement of around 9 cm and 4 cm, for single station and a network of stations, respectively. Clock solutions based on other code types can be used with the same technique, probably yielding in different biases estimation. It is also true that a receiver tracking other types of codes, such as L2C, can also be used. That was done in order to estimate satellite P2-C2 differential code biases (for PRN12, 17 and 31 modernized satellites). Bias values of two satellites (PRN12 and PRN31) are quite similar, but different from PRN17 by around 12-15 cm. As more modernized satellites are launched, this scenario might change, which means that if new satellites have different values for their P2-C2 biases, the range of the differential biases will increase, forcing the values to be farther from zero, in case a zero-mean condition is used. For future research, I suggest work on different validation procedures, maybe with different sources and a wider dataset. Also, activities to keep tracking the bias value

behaviors as new modernized satellites are launched, as well as tracking the behavior of these values over time.

3. Code multipath estimation

A technique to derive code multipath plus noise estimates using a PPP engine was also presented. The iono-free code combination, as well as code measurements on each individual frequency can be used, each of those yielding in different types of multipath plus noise estimates. The main differences between these two types of derivations (iono-free or frequency dependent) are that in case of single frequency (1) it is necessary to use a ionospheric model, such as the implemented in GAPS; and (2) differential code biases need to be accounted for. In a comparison of GAPS' and TEQC's code M+N estimates for L1C and L2P(Y), an agreement of better than 5 cm was found, with estimates from GAPS being systematically slightly less than from TEQC. A potential reason for this is the fact that GAPS provides M+N estimates for the observations which were actually used in the PPP engine, and thus the data is already cleaned from high un-modeled effects (PPP-wise). One should also have in mind that GAPS and TEQC use different assumptions on the estimation, and that the noise part of model does not represent the exactly same effects for the two techniques. In an analysis of iono-free code M+N estimates using L2C and L2P(Y) measurements it was possible to arrive at the conclusion that the noise level of both signals tracked under the same conditions is about the same. Therefore we should expect that the major advantages of using L2C happen in environments where satellite tracking is difficult, such as in urban areas and under canopies.

4. Satellites pseudo-clock estimation

Another technique described in this thesis is used to estimate satellite clock information using data from a single receiver. This clock information is usually infected by residual (un-modeled) errors, and because of that it has been called “pseudo-clock”. The generation of pseudo-clocks is not too different from using a reference station in relative GPS positioning, but it has the advantage of allowing a similar mechanism as relative positioning, but using one single type of data (pseudo-clock) which is useful for both carrier-phase and pseudorange measurements. Also, this is a concept which might be quite useful in order to integrate global-network-based PPP with local-based relative GPS. In an application example, I have shown that a positioning solution using the pseudo-clocks showed to provide better convergence time than when using IGS clocks, and both solutions provided comparable final accuracies in static and kinematic mode, where the difference between final solutions in kinematic mode was of about 5 mm and 3 cm for horizontal and vertical, respectively, and RMS for both kinematic solutions was of around 2.5 for horizontal and 6.5 cm for vertical component. The main conclusion is that it is possible to switch the feeding data of a rover receiver running a PPP engine between global- and local-based derived satellite information, with no loss of precision. The positioning engine does not need to be tuned to each type of satellite data, as long as some conditions (which are explained in the paper) are met during the generation of the local-based pseudo-clocks. This concept represents a great advantage in terms of flexibility for GPS users would consider to use different type of structure to improve their solutions on the field.

5. Wide-area neutral atmosphere model

An approach for creation of wide area neutral atmosphere models was comprehensively described and discussed. A dataset with hourly surface meteorological measurements was used to create a new model for North America, called here UNBw.na. The meteorological values derived from the grids of the new model were compared with actual surface measurements, realized at stations which were not used in the calibration process. All analyses took into consideration the most recent version of UNB models, until now UNB3m. Results for all three meteorological parameters showed that a two-dimensional grid-based model could perform better than a latitude (only) based model (such as UNB3m). The reason for that is the capability of accommodating longitude or regional climatic characteristics of the continent. Regions where the performance of the old model was not satisfactory had results significantly improved with the new model. Investigation of the performance of both models (UNBw.na and UNB3) with radiosonde ray-traced delays at a few sample stations showed that UNBw.na generally has a better fit to the yearly behavior of the zenith delays. It was also possible to notice that results from UNBw.na are more consistent between stations at different locations than when using UNB3m. In terms of general conclusions, UNBw.na was shown to be consistently better than UNB3m in several aspects. The adopted procedure for the grid calibration worked in an adequate way, resulting in a reliable model. Further research on this topic should involve investigation of lapse rate parameters, which were not calibrated in this work. The model for delay computation, which has not been modified so far, will also be reviewed. Assimilation of different data, such as numerical weather models or contemporary standard atmospheres, still needs to be investigated.

9. Bibliography

- Banville, S., R. Santerre, M. Cocard, and R.B. Langley (2008). "Satellite and Receiver Phase Bias Calibration for Undifferenced Ambiguity Resolution". Proceedings of the Institute of Navigation National Technical Meeting, San Diego, California, January 28-30.
- Bisnath, S.B. and R.B. Langley (2001). "Precise Orbit Determination of Low Earth Orbiters with GPS Point Positioning". Proceedings of ION National Technical Meeting, January 22-24, Long Beach, 2001.
- CODE (2007). "CODE's Global Ionosphere Maps (GIM)". Center for Orbit Determination in Europe. Online at <<http://www.aiub.unibe.ch/ionosphere.html>>. Accessed on 1 May 2007.
- Collins, P. (2008). "Isolating and Estimating Undifferenced GPS Integer Ambiguities". Proceedings of the Institute of Navigation National Technical Meeting, San Diego, California, January 28-30.
- Davis, J.L., T.A. Herring, I.I. Shapiro, A.E.E. Rogers, and G. Elgered (1985). "Geodesy by Radio Interferometry: Effects of Atmospheric Modeling Errors on Estimates of Baseline Length". Radio Science, Vol. 20, No. 6, pp. 1593-1607.
- Gao, Y. and Chen, K. (2004). "Performance Analysis of Precise Point Positioning Using Real-Time Orbit and Clock Products". Journal of Global Positioning Systems, Vol. 3 No. 1-2, pp. 95-100, 2004.
- Gao Y., and X. Shen (2002). "A new method for carrier-phase-based precise point positioning". Journal of the Institute of Navigation, Vol. 49, No. 2, pp. 109-116.
- Garbor, M.J. and R.S. Nerem (2002). "Satellite-Satellite Single-Difference Phase Bias Calibration as Applied to Ambiguity Resolution". Journal of the Institute of Navigation, Vol. 49, No. 4, pp. 223-242.
- Ge, M., G. Gendt, M. Rothacher, C. Shi, and J. Liu, (2007). "Resolution of GPS carrier-phase ambiguities in Precise Point Positioning (PPP) with daily observations". Journal of Geodesy, available online at <http://www.springerlink.com/content/117870u48n1124nh/>.
- Goddard Geodetic VLBI GROUP, (2008). "Specifications of HARPOS format version of 2005.03.28". Document available at

- http://gemini.gsfc.nasa.gov/solve_root/help/harpos_format.txt . Accessed on March 5, 2008.
- Gurtner, W. and L. Estey (2006). “RINEX: The Receiver Independent Exchange Format Version 2.11”. Document available online at <ftp://igscb.jpl.nasa.gov/pub/data/format/rinex211.txt> , accessed on July 31, 2007.
- Gurtner, W. and L. Estey (2007). “RINEX The Receiver Independent Exchange Format Version 3.00”. Document available online at <ftp://igscb.jpl.nasa.gov/pub/data/format/rinex300.txt> , accessed on July 31, 2007.
- Heroux P. and J. Kouba (1995). “GPS Precise Point Positioning with a Difference”. Paper presented at Geomatics '95, Ottawa, Ontario, Canada, June 13-15, 1995.
- International GNSS Service (2007). “IGS Products”. <http://igscb.jpl.nasa.gov/components/prods.html> . Web site accessed on September 2007.
- King, B. (2007). Personal communication via e-mail, in December 2007.
- Klobuchar, J.A. (1996). “Ionospheric effects on GPS”. In Global Positioning System: Theory and applications, Vol. 1 (A96-20837 04-17), Washington, DC, American Institute of Aeronautics and Astronautics, Inc. (Progress in Astronautics and Aeronautics. Vol. 163), 1996, p. 485-515.
- Kolb, P.F., X. Chen, and U. Vollath (2005). “A New Method to Model the Ionosphere Across Local Area Networks”. Proceedings of the 18th International Technical Meeting of the Satellite Division of the Institute of Navigation, ION GNSS 2005, Long Beach, California, September 13 – 16 2005.
- Komjathy, A. (1997). Global Ionospheric Total Electron Content Mapping Using the Global Positioning System. Ph.D. dissertation, Department of Geodesy and Geomatics Engineering Technical Report No. 188, University of New Brunswick, Fredericton, New Brunswick, Canada, 248 pp.
- Komjathy, A. (2007). Personal communication via e-mail, in August 2007.
- Komjathy, A., L. Sparks, B.D. Wilson and A.J. Mannucci (2005). “Automated daily processing of more than 1000 ground-based GPS receivers for studying intense ionospheric storms”. Radio Science, Vol. 40, RS6006, DOI: 10.1029/2005RS003279, 2005.
- Kouba, J. (2003). “A Guide to Using International GPS Service (IGS) Products. Publication of the IGS Central Bureau”. February 2003. Online at <<http://igscb.jpl.nasa.gov/igscb/resource/pubs/GuidetoUsingIGSProducts.pdf>>.

- Kouba, J. and P. Héroux (2001). "Precise Point Positioning Using IGS Orbit and Clock Products." *GPS Solutions*, Vol. 5, No. 2 , pp. 12–28.
- Lahaye, F., (2006). Personal communication via e-mail, in August 2006.
- Langley, R.B. (2006). IGSMail-5406: "UNB1 Decommissioned; UNBJ Established." [On-line] Retrieved on September 10 2006 from IGSMail, igsb.jpl.nasa.gov, <http://igsb.jpl.nasa.gov/mail/igsmail/2006/msg00129.html>
- Laurichesse, D., F. Mercier, J-P. Berthias, and J. Bijac, (2008). "Real Time Zero-difference Ambiguities Blocking and Absolute RTK". Proceedings of the Institute of Navigation National Technical Meeting, San Diego, California, January 28-30.
- Leandro R.F. and M.C. Santos (2006). "Wide Area Based Precise Point Positioning." Proceedings of ION GNSS 2006, Fort Worth, Texas, 26-29 September 2006.
- Lockheed Martin (2007). "Lockheed Martin Completes Work on Modernized GPS Satellites". Press release, available online at <http://www.lockheedmartin.com/wms/findPage.do?dsp=fec&ci=18261&rsbci=0&fti=0&ti=0&sc=400>. Accessed on 1 May 2007.
- Maruyama T. (2006). "Extreme enhancement in total electron content after sunset on 8 November 2004 and its connection with storm enhanced density". *Geophysical Research Letters*, vol. 33, l20111, doi:10.1029/2006gl027367, 2006.
- McCarthy, D. D. and G. Petit. IERS Conventions (2003). IERS Technical Note 32, Verlag des Bundesamts für Kartographie und Geodäsie Frankfurt am Main, 127 pp., paperback, ISBN 3-89888-884-3. Also available at <http://www.iers.org/MainDisp.csl?pid=46-25776>. Accessed on 9 March 2008.
- Melbourne, W.G. (1985). "The case for ranging in GPS-based geodetic systems". Proceedings of the first International Symposium on Precise Positioning with the Global Positioning System. U.S. Department of Commerce. Rockville, Maryland, April 15-19. Vol. 1, pp. 373-386.
- Mendes, V.B. and R.B. Langley (1999). "Tropospheric Zenith Delay Prediction Accuracy for High-Precision GPS Positioning and Navigation." *Navigation: Journal of The Institute of Navigation*, Vol. 46, No. 1, pp. 25-34.
- Ocean tide loading provider, 2008. "A short introduction to ocean tide loading provider". Web page available at <http://www.oso.chalmers.se/~loading/loadingprimer.html> . Accessed on March 5 2008.

- Ray, J. (2006). "RINEX Extensions to Handle Clock Information". Document available at ftp://igsceb.jpl.nasa.gov/pub/data/format/rinex_clock.txt , Version 3.00, 14 November 2006. Accessed on March 4 2008.
- Rho, H., R.B. Langley and A. Komjathy (2004). "An Enhanced UNB Ionospheric Modeling Technique for SBAS: the Quadratic Approach". Proceedings of the 17th International Technical Meeting of the Satellite Division of the Institute of Navigation ION GNSS 2004, Long Beach, California, September 21 – 24 2004.
- Rothacher, M., and R. Schmid (2006). "ANTEX: The Antenna Exchange Format Version 1.3". Document available on-line at the International GNSS Service ftp server: <ftp://igsceb.jpl.nasa.gov/pub/station/general/antex13.txt>. Accessed on July 27, 2007.
- Schaer, S., W. Gurtner, and J. Feltens (1998). "IONEX: The IONosphere Map EXchange Format Version ". Document available on-line at the International GNSS Service ftp server: <ftp://igsceb.jpl.nasa.gov/igsceb/data/format/ionex1.pdf> . Accessed in September 2007.
- Space Environment Center (2007). "Indices, Events, and Region Data. Solar, Particle and Geomag. Indices beginning Jan. 1994". http://sec.noaa.gov/ftpmenu/indices/old_indices.html . Web site accessed on February 15 2007.
- Tétreault, P., J. Kouba, P. Héroux, and P. Legree (2005). "CSRS-PPP: An Internet Service for GPS User Access to the Canadian Spatial Reference Frame." *Geomatica*, Vol. 59, No. 1, pp. 17-28.
- U.S. Naval Observatory. "Current GPS constellation". <http://tycho.usno.navy.mil/gpscurre.html>. Web site accessed on July 15 2007.
- Wu, J. T., S. C. Wu, G. A. Hajj, w. I. Bertiger, and S. M. Lichten (1992). "Effects on antenna orientation on GPS carrier phase.". Proceedings of the AAS/AIAA Astrodynamics Conference, Durango, CO, 19-22 Aug. 1991. pp. 1647-1660. 1992.
- Wubben, G. (1985). "Software Developments for Geodetic Positioning with GPS using TI 4100 code and carrier measurements". Proceedings of the first International Symposium on Precise Positioning with the Global Positioning System. U.S. Department of Commerce. Rockville, Maryland, April 15-19. Vol. 1, pp. 403-412.
- Zumberge, J.F., Heflin, M.B., Jefferson, D.C., Watkins, M.M., and Webb, F.H. (1997). "Precise point positioning for the efficient and robust analysis of GPS data from large networks". *Journal of Geophysical Research*, Vol. 102, No. B3, pp. 5005–5018, 1997.

Appendix A: UNB3m_pack, a Neutral Atmosphere Delay Package for Radiometric Space Techniques

In this appendix I am presenting UNB3m_pack, a package with subroutines in FORTRAN and corresponding functions in MatLab which provide neutral atmosphere information estimated using the UNB3m model. The main goal of UNB3m is to provide reliable predicted neutral atmosphere delays for users of GNSS and other transatmospheric radiometric techniques. Slant neutral atmosphere delays are the main output of the package, however it can be used to estimate zenith delays, Niell mapping functions values, delay rates, mapping function rates, surface pressure, temperature and relative humidity and the mean temperature of water vapour in the atmospheric column. The subroutines work using day of year, latitude, height and elevation angle as input values. The files of the package have a commented section at the beginning, explaining how the subroutines work and what the input and output parameters are. The subroutines are self contained; i.e., they don't need any auxiliary files. The user has simply to add to his/her software one or more of the available files and call them in the appropriate way.

A.1. UNB3m_pack

Although slant neutral atmosphere delays are the main output of the UNB3m package, it can also be used to estimate zenith delays (hydrostatic, non-hydrostatic and total), Niell mapping function values (hydrostatic and non-hydrostatic), delay rates, mapping function rates, station barometric pressure, temperature, relative humidity, and mean temperature

of water vapour. These values are a function of day of year, latitude and height and (for some parameters) elevation angle, as shown in the previous section.

The package is made available as a zip-compressed file (UNB3m_pack.zip) which contains the following files:

UNB3m.f – FORTRAN code for delays subroutine;

UNB3mr.f – FORTRAN code for delay rates subroutine;

UNB3mm.f – FORTRAN code for meteorological values subroutine;

UNB3m.m – MatLab code for delays function;

UNB3mr.m – MatLab code for delay rates function;

UNB3mm.m – MatLab code for meteorological values function;

Readme.txt – description of package contents.

Leandroetal2006.pdf – Reference paper for UNB3m (PDF).

Each one of the source code files has a commented section at its beginning, explaining how the subroutine works and what the inputs and outputs (with format and units) are.

The subroutines are self contained; i.e., they don't need any auxiliary files. The user has simply to add to his/her software one or more of the available files listed above and call them in the appropriate way.

A.2. Using UNB3m subroutines

This section explains how to use the UNB3m subroutines, both the FORTRAN and MatLab versions (in this case, functions). There is one subsection for each type of subroutine: delays, delay rates, and meteorological values, respectively. All input and output variables are of type DOUBLE. The subroutines were implemented in FORTRAN 77 and MatLab 7.2, however because they are based on basic mathematical operations, only minor changes (if any) would be necessary to run them using other versions of either FORTRAN or MatLab.

A.2.1. UNB3m – Delays subroutine

This is the primary subroutine of the package. It uses the UNB3m model to calculate the slant neutral atmospheric delay for a given latitude, height, day of year (DOY), and elevation angle.

How this subroutine works

- 1) A look-up table is used to calculate mean sea level (MSL) values for pressure, temperature, relative humidity, temperature lapse rate, and water vapour pressure (WVP) height factor (for given latitude and DOY).
- 2) MSL water vapour pressure is computed according to IERS Conventions 2003 (IERS, 2004).
- 3) Pressure, temperature, and WVP values are computed for the station height.

- 4) Zenith hydrostatic and non-hydrostatic delays are computed using modified Saastamoinen formulas.
- 5) Computation of hydrostatic and non-hydrostatic Niell mapping function values.
- 6) Total slant delay is determined using equations (4) and (5).

Input and output parameters of the subroutine

The parameters are listed in Table A.1.

Table A.1. UNB3m input and output.

INPUT		
Variable	Description	Units
LATRAD	Station geodetic latitude	radians
HEIGHTM	Station orthometric height	metres
DAYOYEAR	Day of year	days
ELEVRAD	Elevation angle	radians
OUTPUT		
Variable	Description	Units
RTROP	Total slant delay	metres
HZD	Hydrostatic zenith delay	metres
HMF	Hydrostatic Niell mapping function	unitless
WZD	Non-hydrostatic zenith delay	metres
WMF	Non-hydrostatic Niell mapping function	unitless

Syntax in FORTRAN (UNB3m.f file)

```
Call UNB3m(LATRAD, HEIGHTM, DAYOYEAR,
ELEVRAD, HZD, HMF, WZD, WMF, RTROP)
```

Syntax in MatLab (UNB3m.m file)

[RTROP HZD HMF WZD WMF] =

UNB3m(LATRAD, HEIGHTM, DAYOYEAR, ELEVRAD)

A.2.2. UNB3mr – Delay rates subroutine

This subroutine uses UNB3m to calculate the slant neutral atmospheric delay rate for given latitude, height, day of year, and elevation angle.

How this subroutine works

Steps 1 to 4 are the same as for the UNB3m subroutine.

- 5) Computation of hydrostatic and non-hydrostatic Niell mapping function rates.
- 6) Total slant delay rate is determined using equations (4), (5) and (9).

Input and output parameters of the subroutine

The parameters are listed in Table A.2.

Table A.2. UNB3mr input and output.

INPUT		
Variable	Description	Units
LATRAD	Station geodetic latitude	radians
HEIGHTM	Station orthometric height	metres
DAYOYEAR	Day of year	days
ELEVRAD	Elevation angle	radians
OUTPUT		
Variable	Description	Units
HZD	Hydrostatic zenith delay	metres
DHMFDEL	Hydrostatic Niell mapping function rate	radians ⁻¹

WZD	Non-hydrostatic zenith delay	metres
DWMFDEL	Non-hydrostatic Niell mapping function rate	radians ⁻¹
DRATE	Total slant delay rate	metres radians ⁻¹

Syntax in FORTRAN (UNB3mr.f file)

```
Call UNB3mr (LATRAD, HEIGHTM, DAYOYEAR,
ELEVRAD, HZD, DHMFDEL, WZD, DWMFDEL, DRATE)
```

Syntax in MatLab (UNB3mr.m file)

```
[DRATE HZD DHMFDEL WZD DWMFDEL]=
UNB3mr (LATRAD, HEIGHTM, DAYOYEAR, ELEVRAD)
```

A.2.2. UNB3mm – Meteorological values subroutine

This subroutine uses UNB3m to calculate the estimated surface temperature, surface pressure, surface water vapour pressure, and mean temperature of water vapour for given latitude, height, and DOY.

The goal of this subroutine is to allow the user to access meteorological values computed from the UNB3m look-up table to be used with delay computation algorithms different from Saastamoinen, which is used in the UNB3m delay and delay rates subroutines. A value for the mean temperature of water vapour is provided, which is useful for deriving water vapour quantities from zenith delays determined with GNSS, for example.

How this subroutine works

Steps 1 to 3 are the same as for the UNB3m subroutine.

- 4) Mean temperature of water vapour is computed.

Input and output parameters of the subroutine

The parameters are listed in Table A.3.

Table A.3. UNB3mm input and output.

INPUT		
Variable	Description	Units
LATRAD	Station geodetic latitude	radians
HEIGHTM	Station orthometric height	metres
DAYOYEAR	Day of year	days
OUTPUT		
Variable	Description	Units
T	Surface temperature	kelvins
P	Surface pressure	millibars
E	Surface water vapour pressure	millibars
TM	Mean temperature of water vapour	kelvins

Syntax in FORTRAN (UNB3mm.f file)

```
Call UNB3mm(LATRAD, HEIGHTM, DAYOYEAR, T, P, E, TM)
```

Syntax in MatLab (UNB3mm.m file)

```
[T P E TM] = UNB3mr(LATRAD, HEIGHTM, DAYOYEAR)
```

A.3. UNB3m_pack retrieval

UNB3m_pack can be downloaded from the website of the Department of Geodesy and Geomatics Engineering of the University of New Brunswick:

<http://gge.unb.ca/Resources/unb3m/unb3m.html>

In order to decompress the file the user can use one of the many compression/decompression applications available on the Internet, such as Filzip (<http://www.filzip.com/>) or Winzip (<http://www.winzip.com/>) for Windows OS with comparable applications for Macintosh, UNIX, and Linux OS. The uncompressed text files have DOS end-of-line delimiters.

Vita

Name: Rodrigo Figueiredo Leandro

Date of Birth: May, 21st of 1978

Place of Birth: Rio de Janeiro, Brazil

Academic Formation:

1996-2000 - Graduated in Civil Engineering by the University of São Paulo (USP), Brazil.

2001-2003 – Master of Science degree obtained from the University of São Paulo (USP), Brazil. Title of dissertation: The influence of the ionosphere in GPS point positioning (in portuguese).

2004-2009 – Ph.D. Candidate at the Department of Geodesy and Geomatics Engineering of the University of New Brunswick, Fredericton, Canada.

Academic/professional Activities:

2002 – Visiting Lecturer at the University of Vale do Rio dos Sinos (UNISINOS) to lecture the 20h graduate course “Total Stations and GPS” (in portuguese).

2002 – Visiting Lecturer at the University of Vale do Rio dos Sinos (UNISINOS) to lecture the 20h graduate course “GPS for GIS” (in portuguese).

2002 – Visiting Lecturer at the University of Vale do Rio dos Sinos (UNISINOS) to lecture the 20h graduate course “Geodesy, Errors Theory and Observation Adjustments: Basic Concepts and Practical Applications to attend the Law 10.267/2001” (in portuguese).

2003 – Graduate Teaching Assistant at the University of São Paulo, in the course “Surveying” (year long course, in portuguese).

2004 – Graduate Teaching Assistant at the University of New Brunswick, in the course “Advanced Adjustments” (winter term).

2004 – Graduate Teaching Assistant at the University of New Brunswick, in the course “Precision Survey” (fall term).

2005 – Graduate Teaching Assistant at the University of New Brunswick, in the course “Advanced Adjustments” (winter term).

2005 – Graduate Teaching Assistant at the University of New Brunswick, in the course “Precision Survey” (fall term).

2006 – Graduate Teaching Assistant at the University of New Brunswick, in the course “Advanced Adjustments” (winter term).

2006 – Graduate Teaching Assistant at the University of New Brunswick, in the course “Survey Camp III” (summer term).

2006-March/2007 – Equipment Technologist at the Department of Geodesy and Geomatics Engineering of the University of New Brunswick.

April/2007 to date – GNSS Research and Development Engineer - Trimble Geomatics and Engineering Group, Trimble Terrasat GmbH, Hoehenkirchen, Germany.

January/2008 to date – Columnist of InfoGNSS Geomática magazine, published by MundoGeo, Brazil.

Publications – Papers:

Veronez, M.R.; Leandro, R.F.; Erba, D.A.; Segantine, P.C.L. and Thum, A.B. “Automated adjustment of a mathematical model for geoidal heights determination over the University of Vale do Rio dos Sinos Campus” (in portuguese). XX Congresso Brasileiro de Cartografia, Porto Alegre - Brazil, 2001.

Leandro, R. F. and Segantine, P.C.L. (2002). “A analysis of the influence of the choice of ionospheric models in determining horizontal coordinates with GPS” (in portuguese). Congresso Brasileiro de Cadastro Técnico Multifinalitário UFSC, Florianópolis – Brazil, October, 2002.

Maia, T.C.B.; Silva, C.A.U.; Romero, R.A.F.; Leandro, R.F.; Segantine, P.C.L.. (2002). “Prediction of GPS carrier-phase measurements using a FIR MLP temporal connexionist model”. XVI Brazilian Symposium on Neural Networks, Porto de Galinhas – Brazil, 2002.

Leandro, R.F., (2004). “A New Technique to TEC Regional Modeling using a Neural Network”. proceedings of ION GNSS 2004, Long Beach, California, September, 2004.

Leandro, R.F. and Santos, M.C., (2004). "Comparison between autoregressive model and neural network for forecasting space environment parameters". *Bollettino di Geodesia e Scienze Affini*, Anno LXII, N.3, June-August-September, 2004.

Leandro, R.F., Santos, M.C. and Cove, K., (2005). "An Empirical Approach for the Estimation of GPS Covariance Matrix of Observations". *Proceedings of ION Annual Meeting 2005*, Cambridge, Massachusetts, June, 2005.

Leandro R.F., Santos, M.C. and Langley R.B., (2006). "UNB Neutral Atmosphere Models: Development and Performance". *Proceedings of ION NTM 2006*, Monterey, California, January, 2006.

Leandro R.F. and Santos, M.C. (2006). "Wide Area Based Precise Point Positioning". *Proceedings of ION GNSS 2006*, Fort Worth, Texas, September, 2006.

Leandro R.F., Santos, M.C. and Langley R.B., (2006). "Wide Area Neutral Atmosphere Models for GNSS Applications". *Proceedings of ION GNSS 2006*, Fort Worth, Texas, September, 2006.

Leandro R.F. and Santos M.C.. "A Neural Network Approach for Regional Vertical Total Electron Content". *Studia Geophysica et Geodaetica*, Vol. 51, 279-292.

Leandro R.F. and Santos M.C. (2007). "Stochastic Models for GPS Positioning: An Empirical Approach". *GPS World*, vol. 18, n. 2, pp. 48-56 – February, 2007.

Leandro R.F. Langley R.B. and Santos M.C. (2007). "Modernized GPS signal P2-C2 Bias Estimation Using Precise Point Positioning". *Proceedings of ION 63rd AM 2007*, Cambridge, Massachusetts, April, 2007.

Leandro, R.F., M.C. Santos, and R.B. Langley (2007). "GAPS: The GPS Analysis and Positioning Software - A Brief Overview." *Proceedings of ION GNSS 2007, the 20th International Technical Meeting of the Satellite Division of The Institute of Navigation*, Fort Worth, Texas, 25-28 September, pp. 1807-1811.

Leandro, R.F., M.C. Santos, and R.B. Langley (2007). "PPP-based Ionospheric Activity Monitoring." *Proceedings of ION GNSS 2007, the 20th International Technical Meeting of the Satellite Division of The Institute of Navigation*, Fort Worth, Texas, 25-28 September, pp. 2849-2853.

Leandro, R.F., R. B. Langley, and M. C. Santos (2007). "Estimation of P2-C2 Biases by Means of Precise Point Positioning." *Proceedings of the ION 63rd Annual Meeting*, Cambridge, Massachusetts, 23-25 April, pp. 225-231.

Leandro, R.F., R.B. Langley and M.C. Santos (2007). "UNB3m_pack: A neutral atmosphere delay package for GNSS." *GPS Solutions*, Vol. 12, No. 1, pp. 65-70.

Súkeová, L., M.C. Santos, R.B. Langley, and R.F. Leandro (2007). A Preliminary Report on L2C Data Collection and Analysis using a Trimble R7 GPS Receiver. Published online at <http://gauss.gge.unb.ca/papers.pdf/R7-Report.Jan07.pdf>. January, 2007.

Súkeová, L., M.C. SANTOS, R.B. Langley, R.F. Leandro, O. Nnani, F.G. Nievinski (2007) "GPS L2C Signal Quality Analysis." Proceedings of the ION 63rd Annual Meeting, Cambridge, Massachusetts, April 23-25, pp. 232-241.

Leandro, R.F. and Santos, M.C., (2008). "An empirical stochastic model for GPS". Proceedings of the Joint Assembly of IAG, IAPSO and IABO, Vol. 130, pp.179-185. Cairns, Australia, August, 2005.

Leandro, R.F., Silva, C.A.U. and Santos, M.C., (2008). "Feeding neural network models with GPS Observations: a challenging task". Proceedings of the Joint Assembly of IAG, IAPSO and IABO, Vol. 130, pp. 186-193. Cairns, Australia, August, 2005.

Landau, H., X. Chen, S. Klose, R.F. Leandro, and U. Vollath (2008). "Trimble's RTK And DGPS Solutions In Comparison With Precise Point Positioning" Observing our Changing Earth, Proceedings of the 2007 IAG General Assembly, Perugia, Italy, 2 – 13 July, 2007, International Association of Geodesy Symposia Vol. 133 (M. Sideris, Ed.), pp. 709-718, Springer.

Leandro, R.F., T. Thirumurthi, L. Súkeová, R.B. Langley, and M.C. Santos (2008). "Analysis of GPS L2C Signal Quality and its Impact on PPP Performance." National Technical Meeting of The Institute of Navigation, San Diego, California, January 28-30, pp. 1020-.

Leandro, R.F., R.B. Langley, and M.C. Santos (2008). "A North America Wide Area Neutral Atmosphere Model for GNSS Applications." Accepted for publication on Navigation: Journal of The Institute of Navigation.

Leandro, R.F., R.B. Langley, M.C. Santos, L. Sukeova, T. Thirumurthi (2008). "The GPS L2C Signal – A Preliminary Analysis of Data Quality". GPS World, vol. 19, n. 10, pp. 42-47 – October, 2008.

Oliveira, L.C., M.C. SANTOS, F.G. Nievinski, R.F. Leandro, S.M.A. Costa, M.F. Santos, J. Magna Jr., M. Galo, P.O. Camargo, J.G. Monico, C.U. Silva, T.B. Maia (2008) "Searching for the optimal relationships between SIRGAS2000, South American Datum of 1969 and Córrego Alegre in Brazil." Observing our Changing Earth, Proceedings of the 2007 IAG General Assembly, Perugia, Italy, 2 – 13 July, 2007, International Association of Geodesy Symposia Vol. 133 (M. Sideris, Ed.), pp. 71-79, Springer.

Santos, Marcelo C., R.B. Langley, R.F. Leandro, S. Pagiatakis, S. Bisnath, R. Santerre, M. Cocard, A. El-Rabbany, R. Landry, H. Dragert, P. Héroux, and P. Collins (2008). "Next-generation algorithms for navigation, geodesy and earth sciences under modernized Global Navigation Satellite Systems (GNSS)." Observing our Changing

Earth, Proceedings of the 2007 IAG General Assembly, Perugia, Italy, 2 – 13 July, 2007, International Association of Geodesy Symposia Vol. 133 (M. Sideris, Ed.), pp. 871-824, Springer.

Publications – Chapters in book:

Leandro, R.F. (2003). “Planialtimetric Surveys”. In “Surveying for Architecture, Engineering and Geology students” (in portuguese). First Edition, UNISINOS press, São Leopoldo – Brazil, 2003.

Leandro, R.F. (2003). “Errors Theory for Surveying”. In “Surveying for Architecture, Engineering and Geology students” (in portuguese). First Edition, UNISINOS press, São Leopoldo – Brazil, 2003.

Awards:

2004 – Best Student Paper Award by the Geodesy Section of the Canadian Geophysics Union. Paper presented at the Joint Assembly of CGU, AGU, SEG and EEGS, Montreal, May, 2004. Title: “Regional Computation of TEC using a Neural Network Model”.

2004 – Best Student Paper Award, by the Institute of Navigation. Paper presented at the ION GNSS 2004, Long Beach, California, September, 2004. Title: “A New Technique to TEC Regional Modeling using a Neural Network”

2006 – Best Paper Presentation Award by the Institute of Navigation. Paper presented at the ION GNSS 2006, Fort Worth, Texas, September, 2006. Title: “Wide Area Neutral Atmosphere Models for GNSS Applications”.